POLITECNICO DI MILANO

Scuola di Ingegneria dell'Informazione

Corso di Laurea Magistrale in Ingegneria Fisica

DEVELOPMENT OF A BROADBAND ELECTRONIC BIDIMENSIONAL SPECTROSCOPY SYSTEM IN THE NEAR INFRARED

Relatore:
Chiar.mo Prof. Giulio Nicola CERULLO

Correlatore:
Dott. Margherita MAIURI

Candidato:

Alice CANTALUPPI

Matr. 765192
Cod. persona 10291344

Anno Accademico 2012/2013

Contents

List of Figures

List of Tables

Abstract

Time-resolved spectroscopy is a powerful technique that allows to explore the dynamics of a system by measuring its optical polarization response. In this thesis work I present my contribution for the realization of an innovative and promising set-up for a specific nonlinear technique: the bidimensional electronic spectroscopy (2DES). By this new technique it is possible to fully characterize the third order nonlinear polarization $P^{(3)}$ and to reveal the coupling between electronic transitions, to monitor the energy flow in complex system or to study the inhomogeneous broadening in congested samples.

2DES represents the most complete nonlinear spectroscopy tool to study a system, but it requires a complex set-up and a careful data-analysis. In order to perform this experiment, three incoming pulsed beams are required.

In our laboratories we use the so called pump-probe configuration of 2DES where the first two interaction pulses, called *pump* pulses, have the same propagation $\vec{k}$-vector and the *probe* pulse comes from another direction. The emitted signal is called photon echo and is detected along the probe direction.

The most challenging part of the experiment is to control the two pump pulses that must be phase-locked. In our laboratories it has been proposed a new technique based on birefringent glass wedges, witch could simplify the experimental set-up and fit to ultrashort broadband pulses. My activity was involved in the opto-mechanical realization of this device followed by its optical characterization.

Moreover I performed some preliminary measurements to test the set-up on carbon nanotubes (CNTs). The results obtained are very promising and can be used to address the problem of the inhomogeneous broadening in the nanotubes.

Sommario

La spettroscopia ottica risolta nel tempo è un potente strumento che permette di esplorare le dinamiche di un sistema attraverso la risposta della polarizzazione ottica. Ad oggi sono molte le tecniche di spettroscopia nonlineare basate sull'interazione di impulsi con la materia, ed in questo elaborato presenterò la realizzazione del set-up di spettroscopia elettronica bidimensionale (2DES). L'informazione aggiunta da questa tecnica nuova e promettente riguarda proprio la misura completa del termine non lineare del terzo ordine della polarizzazione: $P^{(3)}$.

Molti sono i vantaggi della 2DES; in particolare, dalle informazioni ricavate, è possibile tracciare eventuali accoppiamenti tra transizioni elettroniche, registrare le dinamiche di flussi di energia in sistemi complessi e misurare l'allargamento di riga inomogeneo in sistemi congestionati. Ad oggi la spettroscopia bidimensionale è lo strumento più completo per lo studio di sistemi, ma proprio per questo motivo essa richiede un set-up particolarmente complesso, e i dati ottenuti devono essere analizzati con cura.

Per generare la polarizzazione del terzo ordine nella spettroscopia 2D c'è bisogno di tre impulsi. Il setup di 2DES realizzato nei nostri laboratori è in geometria pump-probe, ovvero prevede due impulsi con stesso vettore d'onda $\vec{k}$ chiamati impulsi di pompa (*pump* pulses) e un impulso di lettura (*probe* pulse). Il segnale emesso dal campione dopo l'interazione con i tre impulsi incidenti prende il nome di *photon echo* ed è emesso esattamente nella stessa direzione del *probe*.

La principale difficoltà del setup di 2DES risiede nel controllo dei due impulsi di pompa che devono essere agganciati in fase (*phase-locked*). Per risolvere tale difficoltà è stato pensato, nei nostri laboratori, un compatto sistema di cunei (*wedges*) birifrangenti che permette la generazione dei due impulsi di pompa con le caratteristiche desiderate. Durante la mia tesi ho partecipato alla realizzazione dei componenti opto-meccanici e alla caratterizzazione di questo setup.

Infine ho svolto alcune misure preliminari su un campione di nanotubi di carbonio dimostrando la potenzialità della spettroscopia bidimensionale nello studio dei sistemi inomogenei.

Introduction

Scientific research springs from the need of knowledge about what surrounds ourselves. Trying to understand how matter behaves and evolves in time is a hot topic in this field. Physics, chemistry and biology allow us to obtain wide descriptions of matter. Concerning physics thanks to interaction between matter and electromagnetic radiation it is possible to study the composition and the dynamics of almost any sample. The knowledge of all these aspects allows us to be able to understand many phenomena that occur in nature.

As already said, in physics the interaction between light and matter plays a fundamental role in the analysis of a sample. Therefore the optical properties of the matter can be investigated and from them it is possible to retrieve information about the object of study. In particular it is possible to study the physics of a sample thanks to optical spectroscopy. Optical spectroscopy is a technique that involves the electromagnetic radiation and its interaction with matter. Once the electric polarization is generated, it is possible to register it and to retrieve fundamental properties of the sample.

Therefore polarization has a fundamental role in the study of the matter. If many interactions occur, it is possible to talk of high orders of polarization or *nonlinear* polarization. These terms are even more useful in the analysis of the matter. The first term that is directly connected to the physics behavior and composition of a sample is the *third order* polarization $P^{(3)}$ and it is also the first nonlinear term that is reachable for every material. *Nonlinear optical spectroscopy* is therefore a very useful technique since it allows to measure this term of electric polarization.

The importance of this measurements is getting even higher when it is possible to speak of *ultrafast nonlinear optical spectroscopy*. The *ultrafast* feature is obtained thanks to ultrafast pulses that are used as electromagnetic radiation. Thanks to the short duration of these pulses what it is possible to obtain is the characterization of the very first moments of the evolution of the matter when it is excited by radiation.

In this thesis work will be first illustrated the formalism required for an

overview on the nonlinear spectroscopy and afterward will be presented some different techniques that nowadays are used to record the physics evolution of a sample. Then a quite new technique of ultrafast nonlinear spectroscopy, i.e. *two-dimensional spectroscopy* will be treated. It is an innovative method that allows to obtain almost every information from the sample in one single measurement.

In the first chapter it is introduced the formalism of the density matrix operator, a statistic function able to describe the state of matter. The formalism adopted is thus quite rigorous but is necessary for a complete treatise of the perturbative theory. When light interacts with matter the state of the sample is perturbed and starts to oscillate. Thus a polarization inside the material is generated. This oscillations are described by the density matrix operator and hence by studying its the temporal evolution several information about the sample can be retrieved.

In the second chapter some technique of spectroscopy are presented. The simpler that is described is the linear spectroscopy, i.e. a measurement of the absorption spectrum. When several interaction between light and matter take place, higher order of polarization are thus generated inside the material. The density matrix operator allows to know also those terms and thus, techniques that allow to measure it are necessary. Nonlinear spectroscopy helps to do that. Many ultrafast nonlinear spectroscopy techniques are here presented starting from the simpler (the pump probe spectroscopy) and concluding with a new one that is able to extract almost all the information that it is possible to obtain. This nonlinear technique is the bidimensional spectroscopy (2D-S).

In the third chapter is described how this nonlinear technique is realized in our laboratories. 2D spectroscopy involves three pulses, two to pump and one to probe. The most challenging part of the experiment is the control of the delay between the two pump pulses and thus many possible devices that control it are described. An innovative and very interesting way to produce two phase-locked finely controlled replica based on birefringent media is than presented. This device, developed at Politecnico di Milano, is here described and tested. Then the project for all the opto-mechanical mounts and its realization is displayed.

In the fourth chapter is described the experimental setup used for the experiment. The light source used is a very compact Ti:sapphire laser form *Coherent* with pulses of 100 fs at 800 nm with 1 kHz of repetition rate. This light is used to realize an optical parametric amplifier able to generate e near infrared pulsed radiation. These pulses are those used in the bidimensional spectroscopy experiment and thus are here characterized. In the last paragraph is then described the setup used in the laboratory for the 2DES.

In the last fifth chapter, to summarize what it has been said, some very

first measurements are displayed. 2DES is performed on a single walled carbon nanotubes (SWNTs) sample that is briefly described. Its temporal evolution is then recorded at different delays between the two pump pulses and the probe pulse. From data it is possible to observe a certain ultrafast dynamics typical of the sample. To conclude some tips in order to improve the quality of the experiment are given so that less noisy maps with higher resolution can be recorded.

Chapter 1

Quantum theory of the Density Matrix Operator

In this chapter is introduced the formalism that allows a mathematical comprehension of the generation of the third order polarization. First will be discussed the basics concepts of the density operator that describes the system's state, and then will be derivated its time evolution. When matter interacts with electromagnetic pulses, the density operator evolution describes the system's state in time. From this it is possible to retrieve the evolution of the nonlinear polarization. It will be possible to understand why ultrafast nonlinear spectroscopy is fundamental for the study of the evolution and composition of the system in analysis.

1.1 Density Matrix Operator

In a quantum mechanical approach to the interaction between matter and radiation it is possible to divide systems between *pure states* and *mixed states*. A *pure state* is a state of the system (e.g. a molecule) that can be described by a single wavefunction or by combination of wavefunctions. In the most common cases, instead, the state of the system is more complicated and it can not be described by coherent combination of wavefunction. It is not a superposition of single states, it is something more difficult to understand but that can be described by the *density matrix operator*. *Density matrix operator* is a statistical operator that must be involved when a *statistical ensemble* is considered [6] [7].

Thanks to the new formalism that will be presented, it will be possible to calculate the expectation value of any operator $\hat{A}$. Expectation value is defined

as

$$\langle \hat{A} \rangle = \langle \psi | \, \hat{A} \, | \psi \rangle \tag{1.1}$$

that expressed with the basis set $\{|n\rangle\}$ become

$$\begin{aligned} \langle \hat{A} \rangle &= \sum c_n c_m^* \langle n | \, \hat{A} \, | m \rangle \\ &= \sum \rho_{nm} \hat{A}_{nm} \\ &= Tr \left[\rho \hat{A} \right] \end{aligned} \tag{1.2}$$

with $\hat{A}_{nm}$ matrix elements of $\hat{A}$ and $\rho_{nm} = c_n c_m^*$ density matrix elements. This will be clear in next sections.

1.1.1 Density matrix of a pure state

A *pure state* of a system can be represented by a single wavefunction $|\psi\rangle$ and the density matrix operator is defined as:

$$\rho = |\psi\rangle \langle \psi| \, . \tag{1.3}$$

If $\{|n\rangle\}$ is an arbitrary basis set it is possible to write

$$|\psi\rangle = \sum_n c_n \, |n\rangle \tag{1.4}$$

where c_n are the quantum probability amplitudes that satisfy the relation:

$$\langle \psi | \psi \rangle = \sum_n c_n c_n^* = \sum_n |c_n|^2 = 1 \tag{1.5}$$

Thus the density matrix operator can be written as

$$\rho = \sum_{n,m} c_n c_m^* \, |n\rangle \langle m| \, . \tag{1.6}$$

and the density matrix elements ρ_{nm} are

$$\rho_{nm} = \langle n | \, \rho \, | m \rangle = c_n c_m^* . \tag{1.7}$$

It is possible to make a distinction between matrix elements on the diagonal and terms off the diagonal. The firsts are called *population terms* and describe the dynamics of the population of excited or ground states when they interact with electromagnetic radiation, the others are *coherence terms* and give information about the coherent superposition of two different states. These two classes of terms are sufficient for the analysis of the system and, from their time

evolution, it is possible to know the internal evolution of the system.

In this representation it is possible to introduce the time dependence and find the so called *Liouville-von Neumann equation* that describes the evolution of the system in time,

$$\frac{d}{dt}\rho(t) = \frac{d}{dt}\left(|\psi(t)\rangle\langle\psi(t)|\right) = \left(\frac{d}{dt}|\psi(t)\rangle\right)\cdot\langle\psi(t)| + |\psi(t)\rangle\cdot\left(\frac{d}{dt}\langle\psi(t)|\right). \quad (1.8)$$

The terms in the round braces are directly connected to the time dependent Schrödinger equation (TDSEQ). In fact:

$$\frac{d}{dt}|\psi(t)\rangle = -\frac{i}{\hbar}\hat{H}|\psi(t)\rangle \quad (1.9)$$

and its complex conjugate

$$\frac{d}{dt}\langle\psi(t)| = +\frac{i}{\hbar}\langle\psi(t)|\hat{H} \quad (1.10)$$

that substituted in Eq. 1.8 give

$$\begin{aligned}\frac{d}{dt}\rho(t) &= -\frac{i}{\hbar}\hat{H}|\psi(t)\rangle\langle\psi(t)| + \frac{i}{\hbar}|\psi(t)\rangle\langle\psi(t)|\hat{H} \\ &= -\frac{i}{\hbar}\hat{H}\rho(t) + \frac{i}{\hbar}\rho(t)\hat{H} \\ &= -\frac{i}{\hbar}\left[\hat{H},\rho(t)\right].\end{aligned} \quad (1.11)$$

Liouville-von Neumann equation describes the evolution of the density matrix operator and involves the interaction of the Hamiltonian $\hat{H}$ both from the left and from the right with $\rho(t)$

The expectation value of the operator $\hat{A}(t)$ in a *pure state* can be expressed by Eq. 1.2 as

$$\langle\hat{A}(t)\rangle = Tr\left[\rho(t)\hat{A}\right] \quad (1.12)$$

with $\hat{A}_{nm}(t)$ matrix elements of $\hat{A}(t)$. The density matrix operator in a *pure state*, indeed, allows to calculate the expectation value of any operator $\hat{A}(t)$. Concerning the evolution of the wavefunction in *pure states*, it is described by the Schrödinger equation, see Eq. 1.9, therefore it doesn't involves the density matrix operator.

1.1.2 Density matrix of a mixed state

In most of the cases it is not possible to speak of *pure state* because the system cannot be described only by a single wavefunction. Moreover it is important to underline that in *pure states*, Schrödinger and Liouville-von Neumann equa-

tions are identical and therefore the density matrix operator does not add any additional physical meaning to the analysis of the system.

Things get more interesting when a statistical approach is taken and *ensemble* of molecules are considered. The system cannot be described by a superposition of *pure states*, it is instead a undetermined state in between of all the possible states. This systems, called *mixed states*, cannot be described by a single wavefunction or by a coherent superposition of wavefunctions, and the only way to trace it is thanks to the density matrix operator.

Let p_s be the classical probability that the *ensemble* is in a certain state $|\psi_s(t)\rangle$ described by

$$|\psi_s(t)\rangle = \sum_{j=1}^{n} c_j(t) \, |\psi_j\rangle \tag{1.13}$$

the density matrix operator is defined as

$$\rho(t) = \sum_s p_s \, |\psi_s(t)\rangle \, \langle\psi_s(t)| \tag{1.14}$$

with $p_s \geq 0$ and $\sum_s |p_s|^2 = 1$. Note that $\rho(t)$ is not a coherent superposition of state, i.e. it is not equivalent to any wavefunctions. It is possible to underline how the *pure states* are a particular case of the *mixed states* in which $p_k \neq 0$ and $p_s = 0$ for every $s \neq k$.

Let's try to calculate the expectation value for an operator $\hat{A}(t)$ and the evolution of the system of *mixed states*. As in the previous section the expectation value will depend on the density matrix operator (see Eq. 1.2):

$$\langle \hat{A}(t) \rangle = \sum_s p_s \, \langle\psi_s(t)| \, \hat{A} \, |\psi_s(t)\rangle = Tr \left[\rho(t) \hat{A} \right]. \tag{1.15}$$

The temporal evolution of the system is more difficult to evaluate with respect to the previous case, but since the transformation from a *pure state* to *mixed state* is linear, in a first approximation equation 1.11 is still valid. To be more precise some additional terms must be considered for a complete treatment.

For a statistical average it is possible to write the basis representation of the density matrix operator

$$\rho_{nm}(t) = \sum_s p_s c_n^{s*} c_m^s \tag{1.16}$$

and the density matrix elements evolution is

$$\begin{aligned} \dot{\rho}_{nm}(t) &= \sum_s \frac{dp_s}{dt} c_n^{s*}(t) c_m^s(t) + \sum_s p_s \left(\frac{dc_n^{s*}}{dt} c_m^s(t) + c_n^{s*}(t) \frac{dc_m^s}{dt} \right) \\ &= \sum_s \frac{dp_s}{dt} c_n^{s*}(t) c_m^s(t) - \frac{i}{\hbar} \left[\hat{H}, \rho(t) \right]_{nm} \end{aligned} \tag{1.17}$$

Properties	Pure state	Mixed state
Hermitian	$\rho^*_{nm}(t) = \rho_{nm}(t)$	$\rho^*_{nm}(t) = \rho_{nm}(t)$
Diagonal elements	$\rho_{nn}(t) \geq 0$	$\rho_{nn}(t) \geq 0$
Normalization	$Tr\left[\rho(t)\right] = 1$	$Tr\left[\rho(t)\right] = 1$
Trace of ρ^2	$Tr\left[\rho^2(t)\right] = 1$	$Tr\left[\rho^2(t)\right] \leq 1$

Table 1.1: Density matrix operator properties

The second term is related to the *Liouville-von Neumann* equation for a *pure state* while the first leads to dephasing and populations relaxation.

To conclude this section a summary of all the properties of the density matrix operator is shown in Table 1.1.

1.2 Time dependent perturbation theory

Taking in mind the evolution of a *mixed state* described Eq. 1.17, it is possible to calculate the linear response of a time dependent perturbation. Let's consider an Hamiltonian in the form

$$\hat{H}(t) = \hat{H}_0 + \hat{W}(t) \tag{1.18}$$

where $\hat{H}_0$ is the Hamiltonian of the unperturbed system and $\hat{W}(t)$ is the perturbative field generated by the pulses from the laser. $\hat{W}(t)$ will be weaker than the internal electric field generated by the molecules, so that $\hat{W}(t) \ll \hat{H}_0$. This means that pulses do not alter the eigenstates of the system, but will act only on the coefficients c_n. Therefore a perturbative treatment can be used.

Eigenstates of the Hamiltonian can be obtained from

$$\hat{H}_0 \left|n\right\rangle = E_n \left|n\right\rangle \tag{1.19}$$

From the *Liouville-von Neumann* equation for *mixed states* 1.17, considering the dephasing term for the *coherenses*, i.e. ρ_{nm} with $n \neq m$, it is possible to write

$$\dot{\rho}_{nm}(t) = -\frac{i}{\hbar}\left[\hat{H}_0, \rho(t)\right]_{nm} - \frac{i}{\hbar}\left[\hat{W}(t), \rho(t)\right]_{nm} - \frac{\rho_{nm}(t)}{T_2} \tag{1.20}$$

The first term can be easily calculated by expanding the density matrix on the

eigenfunction of the unperturbed Hamiltonian:

$$\begin{aligned}\left[\hat{H}_0, \rho(t)\right]_{nm} &= \langle n| \hat{H}_0 \rho(t) |m\rangle - \langle n| \rho(t) \hat{H}_0 |m\rangle \\ &= E_n \langle n| \rho(t) |m\rangle - E_m \langle n| \rho(t) |m\rangle \\ &= (E_n - E_m)\, \rho_{nm}(t)\end{aligned} \tag{1.21}$$

And then Eq. 1.20 becomes

$$\dot{\rho}_{nm}(t) = -\left(i\omega_{nm} + \frac{1}{T_2}\right) \rho_{nm}(t) - \frac{i}{\hbar}\left[\hat{W}(t), \rho\right]_{nm} \tag{1.22}$$

where $\omega_{nm} = \frac{E_n - E_m}{\hbar}$. Making the hypothesis that the system is at equilibrium before interaction with light, it is possible to suppose zeroth-order terms off diagonals of the density matrix equal to zero, i.e. $\rho^{(0)}_{nm} = 0$ for $n \neq m$. The first-order dynamics hence can be written

$$\dot{\rho}^{(1)}_{nm}(\tau) = -\left(i\omega_{nm} + \frac{1}{T_2}\right) \rho^{(1)}_{nm}(\tau) - \frac{i}{\hbar}\left[\hat{W}(t), \rho^{(0)}\right]_{nm} \tag{1.23}$$

with τ absolute time. The solution of this equation, expressed in relative time delay, is

$$\rho^{(1)}_{nm}(t) = \frac{i}{\hbar} \int_0^\infty \left[\hat{W}(t - t_1), \rho^{(0)}\right]_{nm} e^{-\left(i\omega_{nm} + \frac{1}{T_2}\right) t_1} dt_1. \tag{1.24}$$

In order to expand the commutator, let's consider the perturbation term

$$\hat{W}(t) = \hat{\mu}(t) E^{'}(t) cos(\omega t) = \frac{\hat{\mu}(t)}{2} E^{'}\left(e^{i\omega t} - e^{-i\omega t}\right) = \frac{\hat{\mu}(t)}{2}\left(E(t) - E^*(t)\right) \tag{1.25}$$

that will give

$$\begin{aligned}\left[\hat{W}(t), \rho^{(0)}\right]_{nm} &= \left(\hat{W}(t)\rho^{(0)} - \rho^{(0)}\hat{W}(t)\right)_{nm} \\ &= \left(\hat{\mu}\rho^{(0)} - \rho^{(0)}\hat{\mu}\right)_{nm} \left(E(t) - E^*(t)\right) \\ &= -\left(\rho^{(0)}_{mm} - \rho^{(0)}_{nn}\right) \hat{\mu}_{nm} \left(E(t) - E^*(t)\right)\end{aligned} \tag{1.26}$$

since $\rho^{(0)}_{nm} = 0$ for $n \neq m$. If the incoming radiation is resonant with the system, i.e. $\omega = \omega_{nm}$, first-order density matrix will be in the form

$$\begin{aligned}\rho^{(1)}_{nm}(t) = \frac{i}{\hbar}\left(\rho^{(0)}_{mm} - \rho^{(0)}_{nn}\right) \hat{\mu}_{nm} \cdot \\ \left\{e^{-i\omega t} \int_0^\infty E^{'}(t - t_1) e^{-t_1/T_2} e^{2i\omega t_1} dt_1 + e^{i\omega t} \int_0^\infty E^{'}(t - t_1) e^{-t_1/T_2} dt_1\right\}.\end{aligned} \tag{1.27}$$

Thanks to rotating wave approximation is it possible to neglect the first integral that will oscillate too fast, and consider only the second term in the between of the braces. This will simplify the analytic formalism and will allow a easier analysis. Eq. 1.27 shows how first order density matrix operator off diagonal elements are non zero and if the same calculation is performed for the opposite corner term, what would be obtained is

$$\rho_{mn}^{(1)} = \rho_{nm}^{*(1)} \tag{1.28}$$

thus, off diagonal terms of the density matrix operator are complex conjugates.

In order to go beyond the first order of the density matrix operator elements in perturbative expansion it is possible to follow the same procedure, but an easier formalism can be introduce to make this operation easier. Thanks to this new formalism that will be introduced in the next paragraph will be possible to evaluate high-order terms of the density matrix operator $\rho^{(n)}$. These will lead to high order polarization terms. Thus let's introduce the *interaction picture* formalism.

1.2.1 Interaction picture

The importance of *interaction picture* is due to the fact that it allows to describe dynamics caused by the laser pulses and those that are internal to the molecules of the *ensemble*. Taking in mind the perturbative Hamiltonian in Eq. 1.18, it is possible to divide the evolution of $|\psi(t)\rangle$ governed by $\hat{H}_0$ from the one dictated by $\hat{W}(t)$. Thus once defined the *time evolution operator* $\hat{U}_0(t, t_0)$ respect to the unperturbed Hamiltonian $\hat{H}_0$ as

$$\hat{U}(t, t_0) = e^{-\frac{i}{\hbar}\hat{H}_0(t-t_0} \tag{1.29}$$

the wavefunction in the *interaction picture* $|\psi_I(t)\rangle$ must satisfy

$$|\psi(t)\rangle = \hat{U}_0(t, t_0)\,|\psi_I(t)\rangle\,. \tag{1.30}$$

The system is hence described by the time evolution operator that is responsible of all that concern the unperturbed Hamiltonian, while $|\psi_I(t)\rangle$ describes the evolution of the wavefunction due to the difference between the total Hamiltonian and the unperturbed one, i.e. the weak perturbation $\hat{W}(t)$. If there is no perturbation, i.e $\hat{H}(t) = \hat{H}_0$, the interaction wavefunction is the unperturbed one and will be constant in time

$$|\psi_I(t)\rangle = |\psi(t_0)\rangle\,. \tag{1.31}$$

By introducing Eq. 1.30 into the Schrödinger Eq. 1.9:

$$\begin{aligned}
-\frac{i}{\hbar}\hat{H}\left|\psi(t)\right\rangle &= \frac{d}{dt}\left|\psi(t)\right\rangle \\
-\frac{i}{\hbar}\hat{H}\cdot\hat{U}_0(t,t_0)\left|\psi_I(t)\right\rangle &= \frac{d}{dt}\cdot\hat{U}_0(t,t_0)\left|\psi_I(t)\right\rangle \\
&= \left(\frac{d}{dt}\hat{U}_0(t,t_0)\right)\cdot\left|\psi_I(t)\right\rangle + \hat{U}_0(t,t_0)\cdot\left(\frac{d}{dt}\left|\psi_I(t)\right\rangle\right) \\
&= -\frac{i}{\hbar}\hat{H}_0\cdot\hat{U}_0(t,t_0)\left|\psi_I(t)\right\rangle + \hat{U}_0(t,t_0)\cdot\left(\frac{d}{dt}\left|\psi_I(t)\right\rangle\right)
\end{aligned} \tag{1.32}$$

From the definition of the perturbative Hamiltonian 1.18, previous equation become

$$-\frac{i}{\hbar}\hat{W}(t)\hat{U}_0(t,t_0)\left|\psi_I(t)\right\rangle = \hat{U}_0(t,t_0)\left(\frac{d}{dt}\left|\psi_I(t)\right\rangle\right). \tag{1.33}$$

Multiplying Eq. 1.33 from the left by a factor $\hat{U}_0^\dagger(t,t_0)$, taking in mind that the time evolution operator is *unitary* (i.e. $\hat{U}^\dagger\hat{U}=1$) and defining the weak interaction Hamiltonian $\hat{H}_I(t)$ as

$$\begin{aligned}
\hat{H}_I(t) &= \hat{U}_0^\dagger(t,t_0)\hat{W}(t)\hat{U}_0(t,t_0) \\
&= e^{\frac{i}{\hbar}\hat{H}_0(t-t_0)}\hat{W}(t)e^{-\frac{i}{\hbar}\hat{H}_0(t-t_0)}
\end{aligned} \tag{1.34}$$

the Schrödinger equation become

$$-\frac{i}{\hbar}\hat{H}_I(t)\left|\psi_I(t)\right\rangle = \frac{d}{dt}\left|\psi_I(t)\right\rangle. \tag{1.35}$$

The *interaction picture* is a compact way to treat the evolution of a system and is a combination of Schrödinger picture and Heisenberg picture. Infact the weak evolution due to the perturbation term of the Hamiltonian is deal with the evolution of the wavefunction, i.e. Schrödinger picture, whereas the overall evolution is left to the operator as the Heisenberg picture requests.

1.2.2 Perturbative expansion of the wavefunction

Eq. 1.35 is the Schrödinger equation for the interaction wavefunction, hence it can be integrated and gives

$$\left|\psi_I(t)\right\rangle = \left|\psi_I(t_0)\right\rangle - \frac{i}{\hbar}\int_{t_0}^{t} d\tau\hat{H}_I(\tau)\left|\psi_I(\tau)\right\rangle \tag{1.36}$$

that can be iteratively solved as

$$|\psi_I(t)\rangle = |\psi_I(t_0)\rangle - \frac{i}{\hbar}\int_{t_0}^{t} d\tau \hat{H}_I(\tau)\,|\psi_I(t_0)\rangle + \left(-\frac{i}{\hbar}\right)^2 \int_{t_0}^{t} d\tau_2 \int_{t_0}^{\tau_2} d\tau_1 \hat{H}_I(\tau_2)\hat{H}_I(\tau_1)\,|\psi_I(\tau_1)\rangle\,. \tag{1.37}$$

Cycling this procedure it is possible to obtain the following equation

$$|\psi_I(t)\rangle = |\psi_I(t_0)\rangle + \sum_{n=1}^{\infty}\left(-\frac{i}{\hbar}\right)^n \int_{t_0}^{t} d\tau_n \int_{t_0}^{\tau_n} d\tau_{n-1} \ldots \int_{t_0}^{\tau_2} d\tau_1 \hat{H}_I(\tau_n)\hat{H}_I(\tau_{n-1})\ldots\hat{H}_I(\tau_1)\,|\psi_I(t_0)\rangle \tag{1.38}$$

that is the power expansion in terms of the small interaction term $\hat{H}_I(t)$.

Trying to go back to the Schrödinger picture it is possible to multiply Eq. 1.38 by the time evolution operator since $|\psi(t)\rangle = \hat{U}_0(t,t_0)\,|\psi_I(t)\rangle$. Defining $|\psi_I(t_0)\rangle = |\psi(t_0)\rangle$, previous equation become

$$|\psi(t)\rangle = |\psi^{(0)}(t)\rangle + \sum_{n=1}^{\infty}\left(-\frac{i}{\hbar}\right)^n \int_{t_0}^{t} d\tau_n \int_{t_0}^{\tau_n} d\tau_{n-1} \ldots \int_{t_0}^{\tau_2} d\tau_1 \hat{U}_0(t,t_0)\hat{H}_I(\tau_n)\hat{H}_I(\tau_{n-1})\ldots\hat{H}_I(\tau_1)\,|\psi(t_0)\rangle \tag{1.39}$$

with $|\psi^{(0)}(t)\rangle = \hat{U}_0(t,t_0)\,|\psi(t_0)\rangle$ zeroth-order wavefunction that describes the evolution of the *ensemble* due to the molecular Hamiltonian $\hat{H}_0$ only. Thus first term of Eq. 1.39 gives the temporal evolution of the system as it was unperturbed. The second term contains all the information about the weak perturbative Hamiltonian and it has a intuitive physical meaning: from t_0 the system evolves freely thanks to the molecular Hamiltonian $\hat{H}_0$ until τ_1, time at which light pulses overcome. From that moment the *ensemble* interacts with the weak perturbation $\hat{H}_I(\tau_1)$ and then propagates. When another weak perturbation overcome $\hat{H}_I(\tau_2)$, the system interacts with it and then it propagates and so on. In order to have a figurative representation of the expansion of the wavefunction, Feynman *single sided diagrams* can be helpful. In Fig. 1.1 the solid arrow is the time axis and the dotted arrows correspond to the interaction at different time τ_1, τ_2 and so on.

1.2.3 Perturbative expansion of the density matrix

It is possible to do the same expansion did for the wavefuntion but on the density matrix operator. In the *interaction picture* it has been shown in Eq. 1.35 that the evolution of the wavefunction is analogous to the Schrödinger equation. The same is true for what concern the density matrix operator in

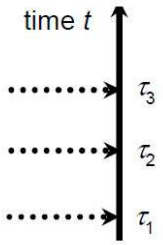

Figure 1.1: Single sided Feynman diagram. [1]

the *interaction picture* what therefore will be described by the *Liouville-von Neumann* equation.

The density matrix operator of a *pure state* in the new formalism is defined as

$$\rho_I(t) = |\psi_I(t)\rangle \langle\psi_I(t)| \tag{1.40}$$

since

$$\begin{aligned} \rho(t) &= |\psi(t)\rangle \langle\psi(t)| \\ &= \hat{U}_0(t,t_0) |\psi_I(t)\rangle \langle\psi_I(t)| \hat{U}_0^\dagger(t,t_0) \\ &= \hat{U}_0(t,t_0)\rho_I(t)\hat{U}_0^\dagger(t,t_0) \end{aligned} \tag{1.41}$$

From the linearity of this derivation, the definition can be expanded to a statistical *ensemble*, i.e. a *mixed state*.

The evolution of the density matrix operator is governed by an equation that is formally equivalent to the *Liouville-von Neumann* equation that in the interaction picture become

$$\frac{d}{dt}\rho_I(t) = -\frac{i}{\hbar}\left[\hat{H}_I(t), \rho_I(t)\right]. \tag{1.42}$$

From the perturbative expansion analogous to the one for the wavefunction, it is possible to expand the density matrix operator in 1.42 obtaining

$$\begin{aligned} \rho_I(t) = \rho_I(t_0) + \sum_{n=1}^{\infty} \left(-\frac{i}{\hbar}\right)^n \int_{t_0}^{t} d\tau_n \int_{t_0}^{\tau_n} d\tau_{n-1} \dots \int_{t_0}^{\tau_2} d\tau_1 \\ \left[\hat{H}_I(\tau_n), \left[\hat{H}_I(\tau_{n-1}), \left[\dots \left[\hat{H}_I(\tau_1), \rho_I(t_0)\right] \dots\right]\right]\right]. \end{aligned} \tag{1.43}$$

By multiplying from the left by the time evolution operator $\hat{U}(t,t_0)$ and by its hermitian conjugate from the right, it's possible to go back in the Schrödinger

domain

$$\rho(t) = \rho^{(0)}(t) + \sum_{n=1}^{\infty} \left(-\frac{i}{\hbar}\right)^n \int_{t_0}^{t} d\tau_n \int_{t_0}^{\tau_n} d\tau_{n-1} \dots \int_{t_0}^{\tau_2} d\tau_1 \\ \hat{U}(t,t_0) \cdot \Big[\hat{H}_I(\tau_n), \Big[\hat{H}_I(\tau_{n-1}), \Big[\dots \Big[\hat{H}_I(\tau_1), \rho(t_0)\Big] \dots\Big]\Big]\Big] \cdot \hat{U}^\dagger(t,t_0). \tag{1.44}$$

that can be rewritten as

$$\rho(t) = \rho^{(0)}(t) + \sum_{n=1}^{\infty} \rho^{(n)}(t) \tag{1.45}$$

simply by defining

$$\rho^{(n)}(t) = \left(-\frac{i}{\hbar}\right)^n \int_{t_0}^{t} d\tau_n \int_{t_0}^{\tau_n} d\tau_{n-1} \dots \int_{t_0}^{\tau_2} d\tau_1 \\ \hat{U}(t,t_0) \cdot \Big[\hat{H}_I(\tau_n), \Big[\hat{H}_I(\tau_{n-1}), \Big[\dots \Big[\hat{H}_I(\tau_1), \rho(t_0)\Big] \dots\Big]\Big]\Big] \cdot \hat{U}^\dagger(t,t_0). \tag{1.46}$$

This last term $\rho^{(n)}(t)$ is the nth-order density matrices ordered by the weak perturbation $\hat{H}_I(t)$ whereas $\rho^{(0)}$ is the zeroth order density matrix operator that evolves unperturbed.

Let's define an equilibrium system defined by a density matrix operator $\rho(t_0)$, it is reasonable to send t_0 to $-\infty$ just thinking that it won't evolve in time under a Hamiltonian H_0. Defining the pertubative Hamiltonian as in Eq. 1.25 that can be written in a simpler way as

$$\hat{W}(t) = \hat{\mu} \cdot E(t) \tag{1.47}$$

Eq. 1.45 become

$$\rho(t) = \rho^0(-\infty) + \sum_{n=1}^{\infty} \rho^{(n)}(t) \tag{1.48}$$

with the nth-order density matrices

$$\rho^{(n)}(t) = \left(-\frac{i}{\hbar}\right)^n \int_{t_0}^{t} d\tau_n \int_{t_0}^{\tau_n} d\tau_{n-1} \dots \int_{t_0}^{\tau_2} d\tau_1 E(\tau_n)E(\tau_{n-1}) \dots E(\tau_1) \\ \hat{U}(t,t_0) \cdot [\hat{\mu}_I(\tau_n), [\hat{\mu}_I(\tau_{n-1}), [\dots [\hat{\mu}_I(\tau_1), \rho(-\infty)] \dots]]] \cdot \hat{U}^\dagger(t,t_0). \tag{1.49}$$

with $\hat{\mu}_I(t) = \hat{U}^\dagger(t,t_0)\hat{\mu}\hat{U}(t,t_0)$ is the dipole operator in the interaction picture. Note that in this formalism the operator is time dependent since the system is evolving under the overall Hamiltonian $\hat{H}_0$, whereas in the Schrödinger picture it is not.

1.3 Nonlinear polarization

Linear polarization is defined as

$$\vec{P} = \epsilon_0 \chi^{(1)} \cdot \vec{E} \tag{1.50}$$

where ϵ_0 is the dielectric constant in vacuum, $\chi^{(1)}$ is the linear electric susceptibility and $\vec{E}$ is the electric field. It is possible to talk about linear polarization when the generating incoming field is weak and, let's say, it interacts only one time with the material. Linear electric polarization will earn the same oscillatory term of the incident radiation and then will evolve in time.

Working with ultrafast optical pulses means to deal with very high peak energies and it is possible to think that the radiation interact several time with the matter. This will lead to some nonlinear effect that are expressed by the *non linear* polarization. Eq. 1.50 must be modified and becomes

$$\vec{P} = \epsilon_0 \left(\chi^{(1)} \cdot \vec{E} + \chi^{(2)} \cdot \vec{E} \cdot \vec{E} + \chi^{(3)} \cdot \vec{E} \cdot \vec{E} \cdot \vec{E} + \dots \right) \tag{1.51}$$

with non linear susceptibilities $\chi^{(n)}$ tensors. In media with inversion symmetry the first nonlinear term of polarization available is the third one, in all the other it is possible to have also the second order polarization term.

Considering an *ensemble* the macroscopic polarization is defined as

$$P = N \langle \hat{\mu} \rangle \tag{1.52}$$

with N number of electric dipoles and $\hat{\mu}$ dipole momentum. Thanks to density matrix operator the expectation value of an operator can be expressed as the trace of the operator multiplied by the density matrix operator, that means

$$P = Tr \left[\hat{\mu} \rho(t) \right] \tag{1.53}$$

that can be generalized to high power of the electric field and give

$$P^{(n)} = Tr \left[\hat{\mu} \rho^{(n)}(t) \right] \tag{1.54}$$

In order to understand on which elements of density matrix operator the polarization depend, let's consider for example to a two level system. In this case N=1 and

$$\hat{\mu} = \begin{pmatrix} 0 & \hat{\mu}_{12} \\ \hat{\mu}_{21} & 0 \end{pmatrix}. \tag{1.55}$$

First order polarization is

$$\begin{aligned} P &= Tr\left[\begin{pmatrix} 0 & \hat{\mu}_{12} \\ \hat{\mu}_{21} & 0 \end{pmatrix}\begin{pmatrix} \rho_{11} & \rho_{12} \\ \rho_{21} & \rho_{22} \end{pmatrix}\right] \\ &= Tr\left[\begin{pmatrix} \hat{\mu}_{12}\rho_{21} & \hat{\mu}_{12}\rho_{22} \\ \hat{\mu}_{21}\rho_{11} & \hat{\mu}_{21}\rho_{12} \end{pmatrix}\right] \\ &= \hat{\mu}_{12}\rho_{21} + \hat{\mu}_{21}\rho_{12}. \end{aligned} \tag{1.56}$$

Eq. 1.56 shows how polarization depend from off-diagonal terms of the density matrix operator. This means that these terms are responsible of the interaction between matter and radiation.

Inserting Eq. 1.49 into Eq. 1.54 it is possible to explicit the nth-order polarization as

$$\begin{aligned} P^{(n)} =& Tr\Bigg[\hat{\mu}\left(-\frac{i}{\hbar}\right)^n \int_{t_0}^{t} d\tau_n \int_{t_0}^{\tau_n} d\tau_{n-1} \dots \int_{t_0}^{\tau_2} d\tau_1 E(\tau_n)E(\tau_{n-1})\dots E(\tau_1)\cdot \\ & \hat{U}(t,t_0)\cdot[\hat{\mu}_I(\tau_n),[\hat{\mu}_I(\tau_{n-1}),[\dots[\hat{\mu}_I(\tau_1),\rho(-\infty)]\dots]]]\cdot\hat{U}^\dagger(t,t_0)\Bigg] \end{aligned} \tag{1.57}$$

Thanks to the invariance to cyclic permutation of the trace operator, it is possible to write Eq. 1.57 as

$$\begin{aligned} P^{(n)} &= Tr\Bigg[\left(-\frac{i}{\hbar}\right)^n \int_{t_0}^{t} d\tau_n \int_{t_0}^{\tau_n} d\tau_{n-1} \dots \int_{t_0}^{\tau_2} d\tau_1 E(\tau_n)E(\tau_{n-1})\dots E(\tau_1)\cdot \\ &\quad \hat{U}^\dagger(t,t_0)\hat{\mu}\hat{U}(t,t_0)\cdot[\hat{\mu}_I(\tau_n),[\hat{\mu}_I(\tau_{n-1}),[\dots[\hat{\mu}_I(\tau_1),\rho(-\infty)]\dots]]]\Bigg] \\ &= Tr\Bigg[\left(-\frac{i}{\hbar}\right)^n \int_{t_0}^{t} d\tau_n \int_{t_0}^{\tau_n} d\tau_{n-1} \dots \int_{t_0}^{\tau_2} d\tau_1 E(\tau_n)E(\tau_{n-1})\dots E(\tau_1)\cdot \\ &\quad \hat{\mu}_I(t)\cdot[\hat{\mu}_I(\tau_n),[\hat{\mu}_I(\tau_{n-1}),[\dots[\hat{\mu}_I(\tau_1),\rho(-\infty)]\dots]]]\Bigg] \end{aligned} \tag{1.58}$$

where in the last step the definition of dipole operator in the interaction picture has been used $\hat{\mu}_I(t) = \hat{U}_0^\dagger(t,t_0)\hat{\mu}\hat{U}_0(t,t_0)$. A different set of temporal variable is used instead of the absolute time τ_n, thus the time interval t_n is preferred whit

t_n defined as

$$\begin{aligned}
\tau_0 &= 0 \\
t_1 &= \tau_2 - \tau_1 \\
t_2 &= \tau_3 - \tau_2 \\
&\cdots \\
t_n &= t - \tau_n
\end{aligned} \tag{1.59}$$

thus Eq. 1.58 become

$$\begin{aligned}
P^{(n)}(t) =& Tr\Bigg[\left(-\frac{i}{\hbar}\right)^n \int_0^\infty dt_n \int_0^\infty dt_{n-1} \dots \int_0^\infty dt_1 \cdot \\
& E(t-t_n)E(t-t_n-t_{n-1}) \dots E(t-t_n-tn-1-\dots-t_1) \cdot \\
& \hat{\mu}_I(t_n+t_{n-1}+\dots+t_1) \cdot [\hat{\mu}_I(t_{n-1}-\dots-t_1), \dots [\hat{\mu}_I(0), \rho(-\infty)] \dots]\Bigg].
\end{aligned} \tag{1.60}$$

Last equation shows how the nth-order polarization term can be written as a convolution of n electric fields:

$$\begin{aligned}
P^{(n)}(t) = & \int_0^\infty dt_n \int_0^\infty dt_{n-1} \dots \int_0^\infty dt_1 \cdot \\
& E(t-t_n)E(t-t_n-t_{n-1}) \dots E(t-t_n-tn-1-\dots-t_1) \cdot \\
& S^{(n)}(t_n, t_{n-1}, \dots, t_1)
\end{aligned} \tag{1.61}$$

with $S^{(n)}(t_n, t_{n-1}, \dots, t_1)$ nth-nonlinear response function

$$\begin{aligned}
S^{(n)}(t_n, t_{n-1}, \dots, t_1) = & \left(-\frac{i}{\hbar}\right)^n \cdot \\
& Tr\Bigg[\hat{\mu}_I(t_n+t_{n-1}+\dots+t_1) \cdot [\hat{\mu}_I(t_{n-1}-\dots-t_1), \dots [\hat{\mu}_I(0), \rho(-\infty)] \dots]\Bigg].
\end{aligned} \tag{1.62}$$

From Eq. 1.62 it is possible to notice that the interactions at time $t_1, t_1 + t_2, \dots, t_1 + \dots + t_{n-1}$ are responsible of the non equilibrium density matrix operator $\rho^{(n)}$ whose off-diagonal elements emit light at $t_n + t_{n-1} + \dots + t_1$.

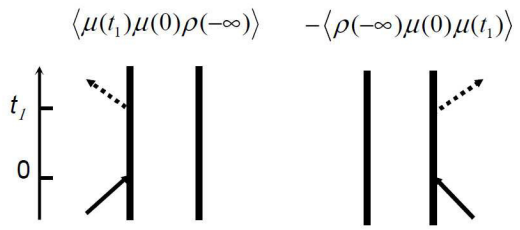

Figure 1.2: Double sided Feynman diagrams for linear response of a two level system [1].

1.3.1 Double sided Feynman Diagrams

Liouville Pathways

Let's try to go more in the detail for what concern the nonlinear response function of a system $S^{(n)}(t_1,\ldots,t_n)$. Due to simplicity let's consider a two level system that interacts with the electromagnetic field. When the commutator is expanded there will be 2^n terms acting either on the right or on the left of the density matrix operator. For example the linear response function is

$$\begin{aligned} S^{(1)}(t_1) &= -\frac{i}{\hbar}Tr\Big[\mu_I(t_1)\cdot[\hat{\mu}_I(0),\rho(-\infty)]\Big] \\ &= -\frac{i}{\hbar}Tr\Big[\hat{\mu}_I(t_1)\mu_I(0)\rho(-\infty)-\mu_I\rho(-\infty)\mu_I(0)\Big] \\ &= -\frac{i}{\hbar}\left(Tr\Big[\mu_I(t_1)\mu_I(0)\rho(-\infty)\Big]-Tr\Big[\mu_I\rho(-\infty)\mu_I(0)\Big]\right). \end{aligned} \tag{1.63}$$

It is possible to represent this function with Feynman diagrams in which there are two vertical lines, the one on the right correspond to the *ket* of the density matrix operator, while the one on the right correspond to the *bra*. The interaction are represented by sided arrow at different temporal time. In Fig 1.2 are shown the two terms of the linear response function. The one on the right is the complex conjugate of the one on the left, thus often it is unexpressed. Due to simplicity, it is possible to consider only diagrams with the last interaction with the *ket*. Solid sided arrow represent interactions with the density matrix operator that generate the non-equilibrium state, while dashed arrow is associated to the last interaction that is responsible of the emitted light by the off-diagonal terms, in accordance with Eq. 1.62.

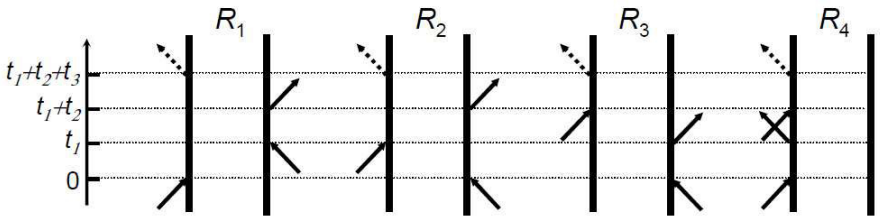

Figure 1.3: Double sided Feynman diagrams for third order response function of a two level system [1].

The *3rd*-order nonlinear response function instead is

$$\begin{aligned}
S^{(3)}(t_3,t_2,t_1) \propto Tr\Big[\mu_I(t_3+t_2+t_1)\cdot[\hat{\mu}_I(t_2+t_1),[\hat{\mu}_I(t_1),[\hat{\mu}_I(0),\rho(-\infty)]]]\Big] \\
= Tr\Big[\hat{\mu}_I(t_3+t_2+t_1)\hat{\mu}_I(t_2+t_1)\hat{\mu}_I(t_1)\hat{\mu}_I(0)\rho(-\infty)\Big] \\
- Tr\Big[\hat{\mu}_I(t_3+t_2+t_1)\hat{\mu}_I(t_2+t_1)\hat{\mu}_I(t_1)\rho(-\infty)\hat{\mu}_I(0)\Big] \\
- Tr\Big[\hat{\mu}_I(t_3+t_2+t_1)\hat{\mu}_I(t_2+t_1)\hat{\mu}_I(0)\rho(-\infty)\hat{\mu}_I(t_1)\Big] \\
+ Tr\Big[\hat{\mu}_I(t_3+t_2+t_1)\hat{\mu}_I(t_2+t_1)\rho(-\infty)\hat{\mu}_I(0)\hat{\mu}_I(t_1)\Big] \\
- Tr\Big[\hat{\mu}_I(t_3+t_2+t_1)\hat{\mu}_I(t_1)\hat{\mu}_I(0)\rho(-\infty)\hat{\mu}_I(t_2+t_1)\Big] \\
+ Tr\Big[\hat{\mu}_I(t_3+t_2+t_1)\hat{\mu}_I(t_1)\rho(-\infty)\hat{\mu}_I(0)\hat{\mu}_I(t_2+t_1)\Big] \\
+ Tr\Big[\hat{\mu}_I(t_3+t_2+t_1)\hat{\mu}_I(0)\rho(-\infty)\hat{\mu}_I(t_1)\hat{\mu}_I(t_2+t_1)\Big] \\
- Tr\Big[\hat{\mu}_I(t_3+t_2+t_1)\rho(-\infty)\hat{\mu}_I(0)\hat{\mu}_I(t_1)\hat{\mu}_I(t_2+t_1)\Big]
\end{aligned} \tag{1.64}$$

that can be written as

$$S^{(3)}(t_3,t_2,t_1) \propto R_4 - R_1^* - R_2^* + R_3 - R_3^* + R_2 + R_1 - R_4^* \tag{1.65}$$

where the complex conjugates are shown. It is possible to visualize these interactions thanks to *Feynman diagrams* in Figure 1.3

where only 2^{n-1} terms are represented. Calculation of the nth-order polarization become even more complicated when the light field is explicitly expressed. In order to avoid all these algebra some approximations can be done in order to simplify the analysis.

Considering Eq. 1.61 for high-order nonlinear polarization, it can be simpli-

fied concerning the expression of the electric fields. Indeed semi-impulsive limit allows to consider fields as three non overlapping, well temporal ordered pulses. Thus $\hat{\mu}_I(0)$ is generated by $E_1(t)$ field, $\hat{\mu}_I(t_1)$ by $E_2(t)$ and so on. Moreover since the electric field is pulsed all of these terms can be treated as *delta*-functions $\delta(t)$ since the dynamics of the system are slower than the temporal duration of the pulses. Electric field is written as

$$\begin{aligned} E_1(t) &= E_1\delta(t)e^{\pm\omega t\mp kr} \\ E_2(t) &= E_2\delta(t-\tau)e^{\pm\omega t\mp kr} \\ E_3(t) &= E_1\delta(t-\tau-T)e^{\pm\omega t\mp kr} \end{aligned} \tag{1.66}$$

thus 3^{rd} order nonlinear polarization from Eq. 1.61 simplifies as:

$$P^{(3)} = S^{(3)}(t,\tau,T) \tag{1.67}$$

that means that 3^{rd} order nonlinear polarization in time ordering semi-impulsive limit is exactly the physics of the system. From this equation it emerges the importance of this nonlinear term of polarization. In this limit the number of terms in the response function is reduced and that could be helpful for a complete analysis of the problem. If other approximation are taken into account, for example the rotating wave approximation and phase matching condition, the number Feynman diagrams that survive is reduce to a number of two. This is a much easier condition respect the starting point of the problem.

Chapter 2

Nonlinear Spectroscopy

In this chapter there will be illustrated some techniques of spectroscopy. First it will be introduced an example of linear spectroscopy and then some nonlinear ultrafast methods of detection of the 3^{rd} order polarization. For each technique it will be presented the information it is possible to retrieve.

2.1 Linear Spectroscopy

Let's start with a linear technique of spectroscopy, i.e. the measurement of the linear absorption spectrum of a sample. In linear measurements there is only one interaction between light and the sample. This yields to only the first-order polarization, known as *linear polarization*. In order to understand how this term is generated it is possible to look at Feynman diagram in Fig. 2.1 and for an analytical analysis it is possible to explicit Eq. 1.61 for the simpler case of n=1.

The linear response function is proportional to

$$S^{(1)} \propto Tr\left[\hat{\mu}_I(t_1)\mu_I(0)\rho(-\infty) - \mu_I(t_1)\rho(-\infty)\mu_I(0)\right] \tag{2.1}$$

that means that anything happens before the time zero. At t=0 the interaction with a light pulse yields to coherences, i.e. to off diagonal density matrix

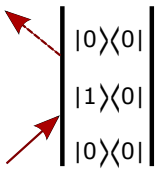

Figure 2.1: Double sided Feynman diagram for linear spectroscopy.

elements ρ_{10} and ρ_{01}. These terms are proportional to the transition dipole momentum

$$\rho_{01}(0) \propto \hat{\mu}_{10} \tag{2.2}$$

Let's think to a two level system which evolution is dictated by the *Liouville-von Neumann* equation 1.20 and in a first instance let's assume the stationary case just setting $\hat{W}(t) = 0$. The total Hamiltonian is equal to the unperturbed one

$$\hat{H}(t) = \hat{H}_0 = \begin{pmatrix} \epsilon_1 & 0 \\ 0 & \epsilon_2 \end{pmatrix} \tag{2.3}$$

hence the time evolution of the density matrix operator is

$$\begin{aligned} \frac{d}{dt}\begin{pmatrix} \rho_{11} & \rho_{12} \\ \rho_{21} & \rho_{22} \end{pmatrix} &= -\frac{i}{\hbar}\left[\begin{pmatrix} \epsilon_1 & 0 \\ 0 & \epsilon_2 \end{pmatrix}\begin{pmatrix} \rho_{11} & \rho_{12} \\ \rho_{21} & \rho_{22} \end{pmatrix} - \begin{pmatrix} \rho_{11} & \rho_{12} \\ \rho_{21} & \rho_{22} \end{pmatrix}\begin{pmatrix} \epsilon_1 & 0 \\ 0 & \epsilon_2 \end{pmatrix}\right] \\ &= -\frac{i}{\hbar}\begin{pmatrix} 0 & (\epsilon_1 - \epsilon_2)\rho_{12} \\ (\epsilon_2 - \epsilon_1)\rho_{21} & 0 \end{pmatrix}. \end{aligned} \tag{2.4}$$

Populations terms are constant while the *coherences* oscillate in time as

$$\begin{aligned} \dot{\rho}_{12}(t) &= -\frac{i}{\hbar}(\epsilon_1 - \epsilon_2)\rho_{12} \quad \Rightarrow \quad \rho_{12} = e^{-i\frac{(\epsilon_1-\epsilon_2)}{\hbar}t}\rho_{12}(0) \\ \dot{\rho}_{21}(t) &= -\frac{i}{\hbar}(\epsilon_2 - \epsilon_1)\rho_{21} \quad \Rightarrow \quad \rho_{21} = e^{+i\frac{(\epsilon_1-\epsilon_2)}{\hbar}t}\rho_{21}(0) \end{aligned} \tag{2.5}$$

This is valid for *pure states*, but when *mixed states* are considered, in order to make complete analysis, dephasing must be introduced. The simplest way to introduce it is just to write Eq. 2.5 as

$$\begin{aligned} \dot{\rho}_{12}(t) &= -\frac{i}{\hbar}(\epsilon_1 - \epsilon_2)\rho_{12} - \Gamma\rho_{12} \quad \Rightarrow \quad \rho_{12} = e^{-i\frac{(\epsilon_1-\epsilon_2)}{\hbar}t}e^{-\Gamma t}\rho_{12}(0) \\ \dot{\rho}_{21}(t) &= -\frac{i}{\hbar}(\epsilon_2 - \epsilon_1)\rho_{21} - \Gamma\rho_{21} \quad \Rightarrow \quad \rho_{21} = e^{+i\frac{(\epsilon_1-\epsilon_2)}{\hbar}t}e^{-\Gamma t}\rho_{21}(0) \end{aligned} \tag{2.6}$$

where Γ takes into account the dephasing of the system and is proportional to $\frac{1}{T_2}$, where T_2 is the *dephasing time*.

Let's now consider the perturbation term in the dipole approximation, i.e. $\hat{W}(t) = -\hat{\mu}E(t)$, the total Hamiltonian is

$$\hat{H}(t) = \begin{pmatrix} \epsilon_1 & 0 \\ 0 & \epsilon_2 \end{pmatrix} + \begin{pmatrix} 0 & -\hat{\mu}_{12} \\ -\hat{\mu}_{21} & 0 \end{pmatrix} E(t) = \begin{pmatrix} \epsilon_1 & -\hat{\mu}_{12}E(t) \\ -\hat{\mu}_{21}E(t) & \epsilon_2 \end{pmatrix} \tag{2.7}$$

from which, with some algebra, it is possible to retrieve that the evolution of the density matrix operator evolution is somehow proportional to the electric

dipole momentum, indeed it is possible to write

$$\rho_{12}(t) \propto e^{-i\frac{(\epsilon_1-\epsilon_2)}{\hbar}t}e^{-\Gamma t}\rho_{12}(0). \tag{2.8}$$

where the $\rho_{12}(0)$ contains the dependance from the dipole momentum: $\rho_{12}(0) \propto \hat{\mu}_{12}$. Analogous equation is valid for $\rho_{21}(t)$.

Going back to the linear response function, at t=0 coherenses are excited with a certain probability proportional to the dipole momentum which evolution in time is described by Eq. 2.8. At $t = t_1$ the off diagonal density matrix elements emit light with a probability that is again proportional to the electric dipole momentum. Thus the linear response is

$$S^{(1)}(t_1) \propto \hat{\mu}^2 e^{-i\frac{(\epsilon_2-\epsilon_1)}{\hbar}t_1}e^{-\Gamma t_1}. \tag{2.9}$$

First order polarization is then described by Eq. 1.61 and hence, by setting $n = 1$ is

$$P^{(1)}(t) = \int_0^\infty dt_1 E(t-t_1)S^{(1)}(t_1). \tag{2.10}$$

Considering a pulsed electric field written as

$$E(t) = E_0\delta(t)(e^{-i\omega t} + e^{i\omega t}) \tag{2.11}$$

with the resonant case

$$\omega = \frac{(\epsilon_2 - \epsilon_1)}{\hbar} \tag{2.12}$$

is is possible to develop Eq. 2.10 as follow

$$\begin{aligned} P^{(1)}(t) &\propto \int_0^\infty dt_1 E_0\delta(t-t_1)(e^{-i\omega(t-t_1)} + e^{i\omega(t-t_1)})\hat{\mu}^2 e^{-i\omega t_1}e^{-\Gamma t_1} \\ &\propto E_0\hat{\mu}^2 e^{-i\omega t}\int_0^\infty dt_1\delta(t-t_1)e^{-\Gamma t_1} + E_0\hat{\mu}^2 e^{i\omega t}\int_0^\infty dt_1\delta(t-t_1)e^{-i2\omega t_1}e^{-\Gamma t_1}. \end{aligned} \tag{2.13}$$

Second term in this last equation oscillates faster than the first, this means that thanks to the rotating wave approximation it can be neglected. The *linear polarization* thus become

$$P^{(1)}(t) = -\frac{i}{\hbar}E_0\hat{\mu}^2 e^{-i\omega t}e^{-\Gamma t}. \tag{2.14}$$

This term emits an electric field with a phase locked at 90° with it,

$$E^{(1)}(t) \propto -iP^{(1)}(t) \tag{2.15}$$

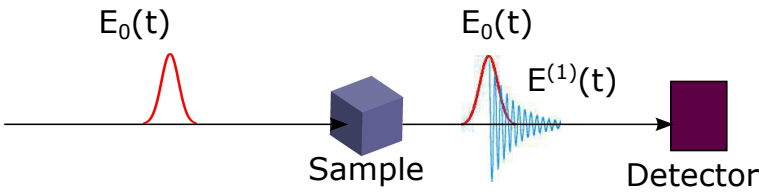

Figure 2.2: Setup for linear spectroscopy

and this pulsed propagating field decays in time. This temporal behavior is called *free induction decay*.

In order to record *first order* polarization and thus the $E^{(1)}(t)$, different approaches can be used. A simple method is shown in Fig. 2.2 where a spectrometer and photodetector are involved. This kind of detector allow a measurement of the intensity, i.e. the temporal average of the signal, since the temporal response of the photodetector is very slow respect to the duration of the pulses. Due to a phase matching conditions the emitted field is collinear with the generating incoming one, hence on the photodetector it will be measured the intensity of the overlap between the two pulses resolved in the frequency domain. The measured field thus is

$$|E_0(\omega) + E^{(1)}(\omega)|^2 = |E_0(\omega)|^2 + |E^{(1)}(t)|^2 + 2Re\left\{E_0(\omega)E^{(1)}(\omega)\right\} \tag{2.16}$$

Due to the fact the generated field is weaker than the incident one, i.e. $|E^{(1)}(\omega)| \ll |E_0(\omega)|$, second term on the right can be neglected. The measurement is a kind of *self-heterodyne* detection due to the collinear geometry between the incoming beam and the generated one. Hence the E_0 is treated as the local oscillator for this system. Looking at the absorption spectrum, that is to $A = 1 - T$ where T is the transmitted light, it is normalized and results

$$\begin{aligned} A(\omega) \propto 1 - \frac{I}{I_0} &= 1 - \frac{|E_0(\omega) + E^{(1)}(\omega)|^2}{|E_0(\omega)|^2} \\ &= -\frac{2Re\left\{E_0(\omega)E^{(1)}(\omega)\right\}}{|E_0(\omega|^2} \propto -2Re\left\{E^{(1)}(\omega)\right\} \end{aligned} \tag{2.17}$$

where in the last step it has been considered $E_0(\omega) = const = E_0$, i.e. an ultrashort broadband pulse assumed to be a delta function $\delta(t)$. Due to the relation between $E^{(1)}$ and $P^{(1)}$ the absorption spectrum is

$$\begin{aligned} A(\omega) &\propto 2Im\left\{P^{(1)}\right\} \propto 2Re\left\{\int_0^\infty e^{-i(\omega-\omega_0)t}e^{-\Gamma t}\right\} \\ &= 2Re\left\{\frac{1}{i(\omega-\omega_0)-\Gamma}\right\} = \frac{2\Gamma}{(\omega-\omega_0)^2+\Gamma^2}. \end{aligned} \tag{2.18}$$

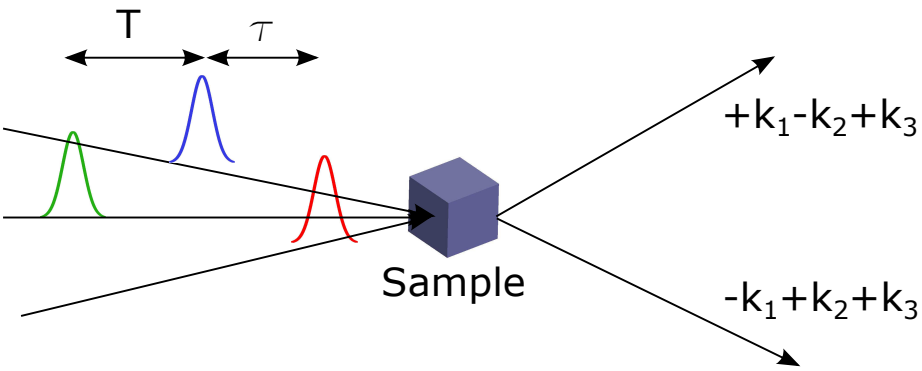

Figure 2.3: Three pulses Photon Echo spectroscopy scheme.

As expected the absorption spectrum is a Lorentzian function with the broadening that depends from the dephasing rate of the transition.

After this simple example of linear spectroscopy, let's try to enlarge the discussion and to go to *third order* polarization measurement techniques.

2.2 Three Pulses Photon Echo Spectroscopy

Going into nonlinear spectroscopy, three interaction between electric field and matter must be taken into account. The first creates the first order coherences, the second one projects them in population states, while the third creates the third order coherences responsible of the nonlinear polarization. This multiple interactions can generate different phenomena that can be explained very easily for example considering a three level system.

The most general technique that allows to have access to the *third order* polarization is the so called *photon echo* spectroscopy. This method involves three pulses delayed by fixed delays τ and T as the basic scheme is represented in Fig. 2.3. Since the three pulses are propagating in different directions, *third order* polarization emits a field in the phase-matched directions k_S given by the following equations

$$\begin{aligned} k_S &= k_3 + k_2 - k_1 \\ k_S &= k_3 + k_1 - k_2. \end{aligned} \tag{2.19}$$

This directions are those that survive from the geometry involved. This means that terms of Eq. 1.64 that survive are those represented in the *double sided Feynman diagram* in Fig. 2.4. The generated third order fields are thus background free and can be measured with a photodetector that integrates the signal in time. Along these two direction signal is not the same: one direction

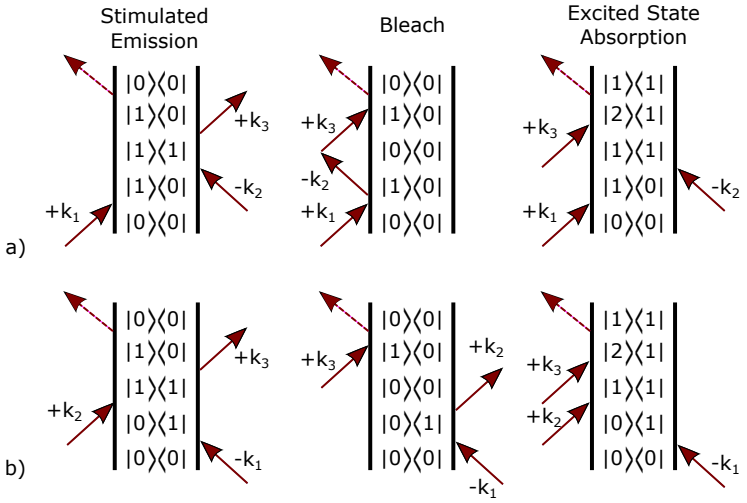

Figure 2.4: Double sided Feynman diagram for photon echo spectroscopy. a) *Non rephasing* response function terms. b) *rephasing* diagrams.

is the so called *rephasing* one, the other is *non rephasing* [8]. These two kind of signals rise every time the third order polarization is generated, but often they are overlapped. Photon echo allows to distinguish them.

The *non rephasing* signal is a signal that is generated by the third order polarization and it is the *free induction decay* field, thus is a quite long pulse. Indeed it's duration depend from the time that polarization take to disappear, i.e from the homogeneity of the material. This signal in generated immediately by the polarization, that means in the instant in which the third pulse interacts with matter.

Instead, the *rephasing* signal in photon echo experiments is a short pulse that is emitted by the material after exactly a delay τ from the third pulse. This emission is due to the recombination of all the electric dipole in the material that after a certain time are again in phase one with each other. This rephasing is somehow due to the second and third pulses of the photon echo experiment. This pulse reverse the temporal axis, i.e. reverse the temporal evolution of all the electric dipole in the material that recombine for a short time and emit the *rephasing* field. It can be figured as the fist pulse is a $\pi/2$-pulse, that means a pulse able to generate a coherence. It stimulates the sample and the dephasing of all the electric dipoles. The second and the third pulse together act as a π-pulse that is able to inverse the population of the system and generate a sort of time inversion that is responsible of the *echo*.

The temporal scheme both for *rephasing* and *non-rephasing* signal is represented in Fig. 2.5 from which it is possible to understand the difference from

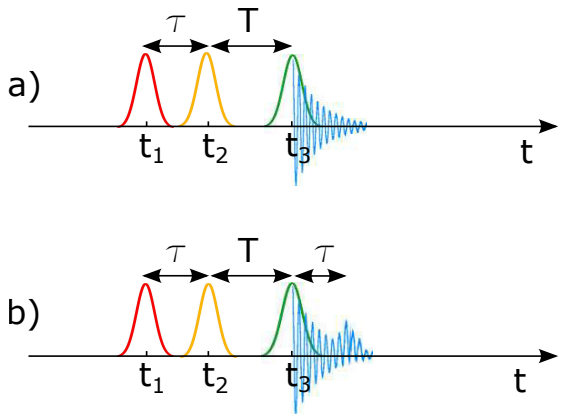

Figure 2.5: Temporal scheme of three pulses photon echo spectroscopy. a) *non rephasing* field. The *free induction decay* field is generated at the arrival of the third pulse. b) *rephasing* temporal scheme. After the third pulse an echo appears at delay τ.

the two.

In photon echo experiments the *rephasing* signal is revealed thanks to a photodetector that integrates in time the incoming signal. If the diffracted pulse is detected for different values of T between the second and the third pulse, the recorder signal decays with a time constant proportional to the decaying time of the population state (the *longitudinal* decay time). If different measurement are taken for different values of τ between the first and the second pulse, the signal decays with a time constant proportional to the *dephasing time* (or *transverse* decay time), i.e. the time needed by the system to lose coherence with the perturbation.

Hence photon echo experiment allows to retrieve all the temporal constant of the system. It is interesting to note that whit this experiments, many are the degree of freedom that take place: $\vec{k}_1$, $\vec{k}_2$ and $\vec{k}_3$, concerning the spatial components and t_1, t_2 and t_3 for the temporal delays. Going to the relative delays this means that with three pulse photon-echo it is possible to control τ_1, T and τ_3 where in $\tau_1 = \tau_3 = \tau$. It will be shown how not always these degree of freedom will be accessible, and on the other hand, how these can be increased, allowing to distinguish between the τ_1 and τ_3.

Three pulse photon echo allows to distinguish between system with a *homogenous* line broadening from one with an *inhomogeneous* broadening. This is an important feature that makes photon echo a very interesting technique. Let's take a look at the diffracted direction of the *rephasing* and *non rephasing* in Eq. 2.19. The only difference between the two is connected to the sign of the first two interaction pulses. This means that by using negative delay between the first and the second pulse, i.e. reversing their temporal order, *non rephasing*

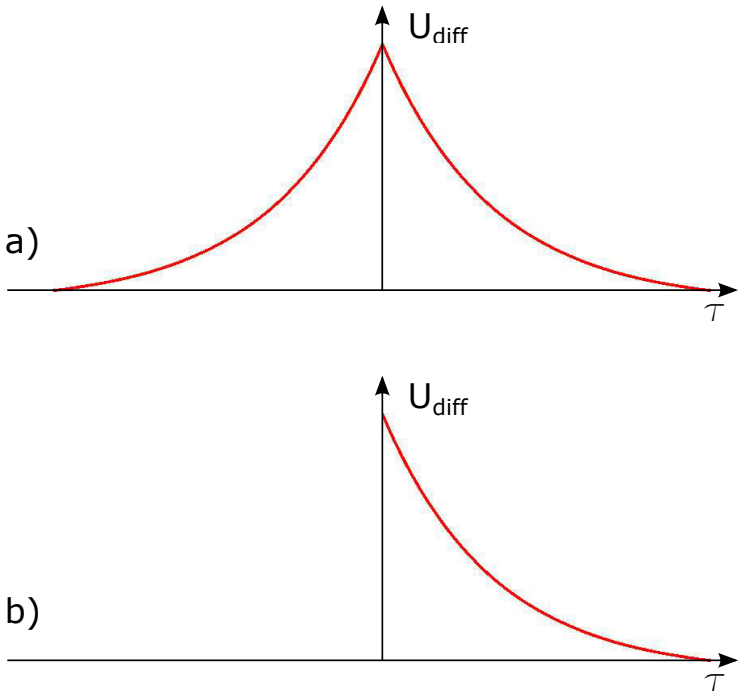

Figure 2.6: a) Diffracted signal in the $-k_1 + k_2 + k_3$ in an *homogeneous* system at different τ. Either for positive and negative delays a signal is detected. b) Diffracted signal in the $-k_1 + k_2 + k_3$ in an *inhomogeneous* system at different τ. Only at positive τ photon echo is revealed.

signal can be measured in the *rephasing* direction. Measuring the energy in this direction at various τ, either positive and negative, the detected field will look different on the basis of the sample. If the sample is *homogeneous* an echo will be revealed also for negative τ since all the dipoles are always in phase. If an *inhomogeneous* target is analyzed, the echo will appear only for positive value of τ. In Fig. 2.6 this difference is depicted.

Photon echo spectroscopy is the basic of all the nonlinear spectroscopy that are presented in this chapter. Trying to reduce the number of pulses, other possible techniques has been explored. The easiest is the *pump probe* spectroscopy presented in the next section.

2.3 Pump Probe Spectroscopy

Pump probe spectroscopy is another ultrafast third-order spectroscopy technique that doesn't involve directly three pulses. It instead exploits the high power of the pump pulse and thus this pulse interacts two times with the sample. The probe pulse, delayed respect the pump one by a variable delay T, is the one

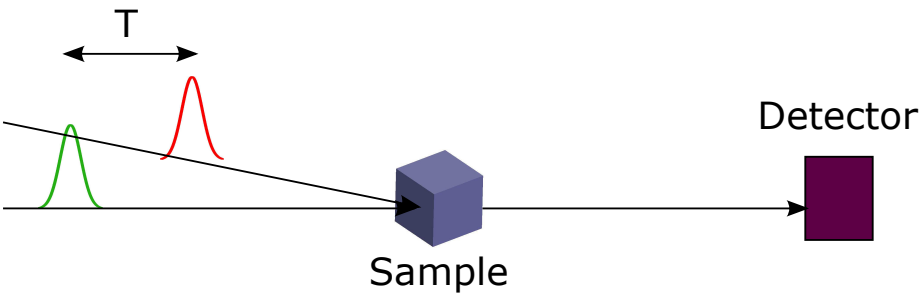

Figure 2.7: Pump probe spectroscopy setup.

that generates the *third order* polarization term. This simplification respect to the previous case of course affects the number of degree of freedom of the measurement. In pump probe spectroscopy the first two pulses have the same $\vec{k}$-vector, and the same is true for the third and a local oscillator pulse. Concerning the delays between the pulse the only accessible one is T, i.e. the population time. The situation is the following:

$$\begin{aligned} \vec{k}_1 = \vec{k}_2 \qquad &\Rightarrow \qquad \tau_1 = 0; \\ \vec{k}_3 = \vec{k}_{LO} \qquad &\Rightarrow \qquad \tau_3 = 0. \end{aligned} \tag{2.20}$$

In Fig. 2.7 is represented the simple scheme that is involved for pump probe experiments. Due to phase matching the *third order* polarization is generated in the same direction of the the probe pulse.

It is possible to see *pump probe* spectroscopy as a special case of three photon echo spectroscopy in which the first and the second pulse are collinear and temporally overlapped, i.e. they are the same pulse. From Eq. 2.19 is clear why the generated pulse has the same $\vec{k}$-vector as the probe pulse. From this equation emerge also that *rephasing* and *non rephasing* fields are emitted in the same direction.

Macroscopically pump probe can be seen as a technique in which the pump pulse excites the system and the probe reveals the behavior of the system at different times. It is like the probe pulse registers the temporal evolution of the state of the molecule under analysis. The condition *sine qua non*, is that the pump must be at resonance with an excited state and that the probe is at resonance with other allowed transitions of the molecule. In ultrafast non linear spectroscopy, ultrashort pulses are involved and thus they allow to have a temporal resolution of the order of their temporal duration, that means in the order of 10^{-15} seconds.

To have a figurative idea of what happens into the sample, in Fig. 2.8 are represented the energy levels of a three level system and the allowed transitions.

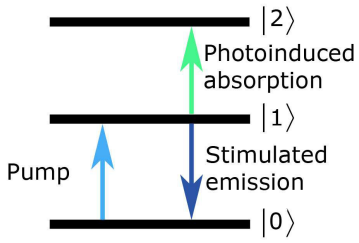

Figure 2.8: Three level system energy levels.

After the pump pulse the system is in a population state $|1\rangle$. The probe pulse is near resonance both with the $|1\rangle \rightarrow |2\rangle$ and the $|2\rangle \rightarrow |1\rangle$ transition, hence it can induce an absorption (green arrow in figure) or an emission (dark blue arrow in figure), called respectively *photoinduced absorption* and *stimulated emission*. Another kind of signal that can be revealed is the so called *photo bleaching* that is just the case in which the system, when the probe pulse arrives, is not anymore able to absorb from the ground to the excited state even if the pulse is at resonance with this transition. This generates an increasing in the transmitted pulse from the sample.

Pump probe technique actually looks at a differential signal, indeed it reveals a difference in transmission between the probe pulse in the case of *pump-on* and *pump-off*, normalized with its transmission without pump. Thus each of the photophysical signals have a certain sign associated. Let $\frac{\Delta T}{T}$ be the differential signal registered by the pump probe signal detector, if stimulated emission (SE) occurred $\frac{\Delta T}{T}$ will be positive. The same is true for the photobleaching signal (PB). In the case of photoinduced absorption (PA) the transmission of the probe pulse is reduced, thus the $\frac{\Delta T}{T}$ is negative.

Going back to a representation with the density matrix formalism, the *double sided Feynman diagrams* are schematically the same than those for the photon echo spectroscopy represented in Fig. 2.4. In this figure the interaction with the pump pulses can be seen as these interact one just before the other.

Making the same approximation done for the third order nonlinear polarization, Eq. 1.67 is valid. Once calculated the third order response function the behavior of the polarization is known. Pump probe experiment reveals the *free induction decay* generated by this nonlinear polarization term with an heterodyne detection made with the probe pulse that is in the same direction. The detector integrates over time the signal and reveal the absorption. If the pump pulse is modulated the detector can read the difference of the probe pulse with the pump on, and without. From this it is possible to reconstruct the

phenomenological behavior of the sample.

2.4 Two-dimensional Spectroscopy

In order to enlarge the number of information that ultrafast nonlinear spectroscopy allows to retrieve, it is possible to use *multidimensional spectroscopy*. This technique exploits all the information that is possible to retrieve about the *third order* nonlinear response.

The idea is quite simple: it starts from the photon echo theory but it tries to enhance the spectral resolution of the gained information. In order to do that let's try to understand what it is needed for this kind of experiment. As in all the nonlinear spectroscopy methods, the first pump pulse generates the linear polarization, the second creates a population state, the third yields the third order polarization. The critical aspect of this method is that it needs a precise interferometric time control of the delay between the first and the second pulse that must be phase-locked. This is due to the fact that in this way the first two interaction between the sample and the electromagnetic radiation are almost identical. The fine control of the delay between the two allows to have an important information in the frequency domain. Indeed let's take the Fourier transform of two peaks, what it is obtained is a sinusoidal curve with an oscillating period, i.e. a frequency, proportional to the temporal distance between the two. Fig. 2.9 depicts what it has been said. This means that by exciting with different delays between the first two identical pulses, different modes in the sample are stimulated. Thus to have a complete information of the behavior of an object in analysis, it is possible to scan this delay in order to excite all the possible oscillating modes of matter.

Bidimensional spectroscopy starts from the photon echo, hence nonlinear polarization emits fields in the *rephasing* an *non rephasing* directions. The double sided Feynman diagrams for a two level system are the same than those in Fig. 2.4. The main difference from photon echo is that instead of having an homodyne detection, 2D-spectroscopy involves a fourth field for an heterodyne detection. This local oscillator must be phase locked with the generated $E^{(3)}(t)$ pulse. All these phase conditions make 2D spectroscopy quite challenging, and the hardest part remain the fine control of the delay between the first and the second pulse.

The involved fourth field actually allows to get more information respect to the photon echo spectroscopy. Indeed by controlling the delay of this with the free induction decay field, it is possible to make $\tau_3 \neq \tau_1$. In this way the overall degree of freedom on which it is possible to act are even more in this kind of experiments.

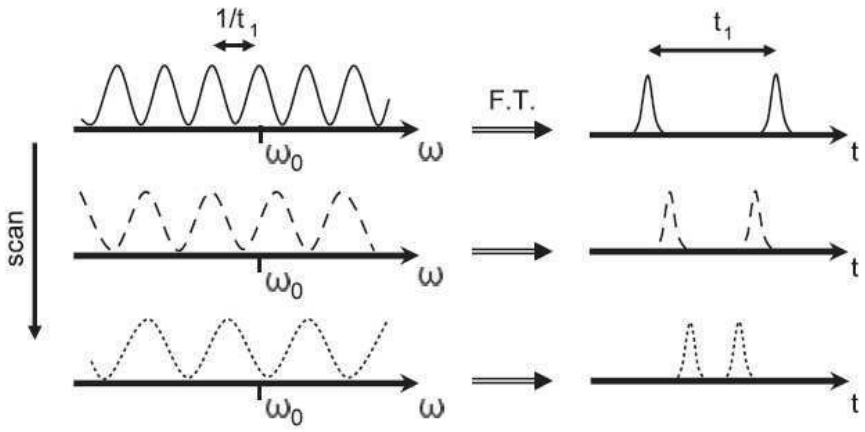

Figure 2.9: Pump pulses spectrum. If many delays are imposed, all the resonant modes are excited [1].

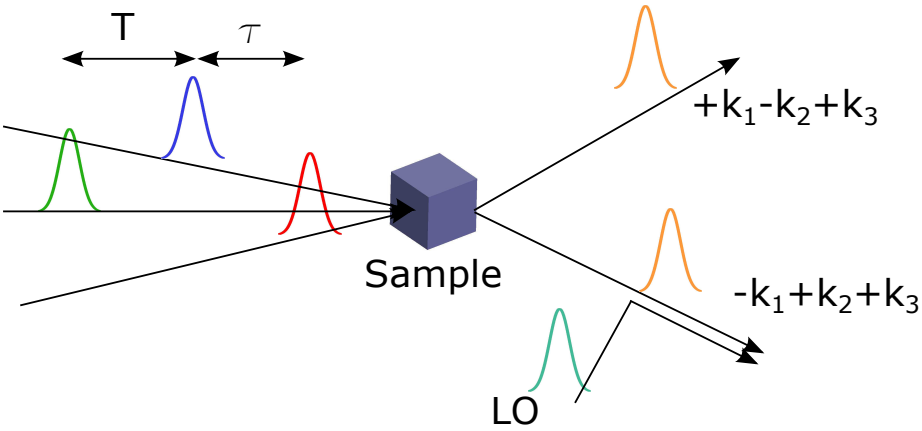

Figure 2.10: Bidimensional spectroscopy setup.

The setup scheme is represented in Fig. 2.10. The delay between the first and the second pulse is $\tau 1 = \tau$ which is the one that must be fine monitored, while delay between the second and the third pulse is T. The detection is non background free but the offset is easily subtracted. The measured field will be

$$|E_{LO}(\omega_t)+E^{(3)}(\omega_t,T,\tau)|^2 \approx |E_{LO}(\omega_t)|^2+2Re\left\{E_{LO}(\omega_t)E^{(3)}(\omega_t,T,\tau)\right\} \quad (2.21)$$

In ultrafast 2D spectroscopy all the approximation made are still valid, that means that the semi-impulsive limit, the rotating wave approximation and the phase matching condition are considered. Third order polarization thus is de-

scribed by Eq. 1.67

$$P^{(3)} = S^{(3)}(t, T, \tau) \tag{2.22}$$

Since the third order nonlinear response is quite difficult to be visualized, an important step of 2D spectroscopy is the Fourier transform of this function in the frequency domain both respect to t and τ obtaining a spectral resolved nonlinear response function $S(\omega_t, T, \omega_\tau)$. This function now can be represented in a 2D plot with two frequency resolved axis and the analysis become quite intuitive. Varying the arrival of the third pulse, i.e. varying T, different maps can be recorded, and this will provide complete information about the nonlinear response function.

Each term of $S(\omega_t, T, \omega_\tau)$ will have both a real and imaginary part that can be considered alone, or by taking the absolute value of them together. Indeed considering the *rephasing* direction the nonlinear response function terms are

$$R_2(t, T, \tau) = R_3(t, T, \tau) \propto e^{i\omega t_1} e^{-\Gamma t_1} e^{-i\omega t_3} e^{-\Gamma t_3} \tag{2.23}$$

while for the *non rephasing* diagrams is

$$R_1(t, T, \tau) = R_4(t, T, \tau) \propto e^{-i\omega t_2} e^{-\Gamma t_2} e^{-i\omega t_3} e^{-\Gamma t_3}. \tag{2.24}$$

By Fourier transforming these equations, the pathways become

$$R_{2,3}(\omega_t, T, \omega\tau) \propto \frac{1}{-i(\omega_\tau - \omega) - \Gamma} \cdot \frac{1}{i(\omega_t - \omega) - \Gamma} \tag{2.25}$$

and respectively

$$R_{1,4}(\omega_t, T, \omega\tau) \propto \frac{1}{i(\omega_\tau - \omega) - \Gamma} \cdot \frac{1}{i(\omega_t - \omega) - \Gamma}. \tag{2.26}$$

Due to the geometry of the setup, the third order field is emitted in two directions and hence both of them must be measured. From literature it is known that the best 2D map in term of contrast and of sign coherence is obtained when all the term of *rephasing* and *non rephasing* are summed up and than only the real part is taken:

$$R_{abs} = Re\left\{R_{2,3}(\omega_t, T, \omega\tau) + R_{1,4}(\omega_t, T, \omega\tau)\right\} \tag{2.27}$$

that generate the so called *purely absorptive spectrum*.

From what is has been said, bidimensional ultrafast spectroscopy plays a very important role in the analysis of a sample. It reveals at least all the information included in the third order nonlinear response, i.e. the composition

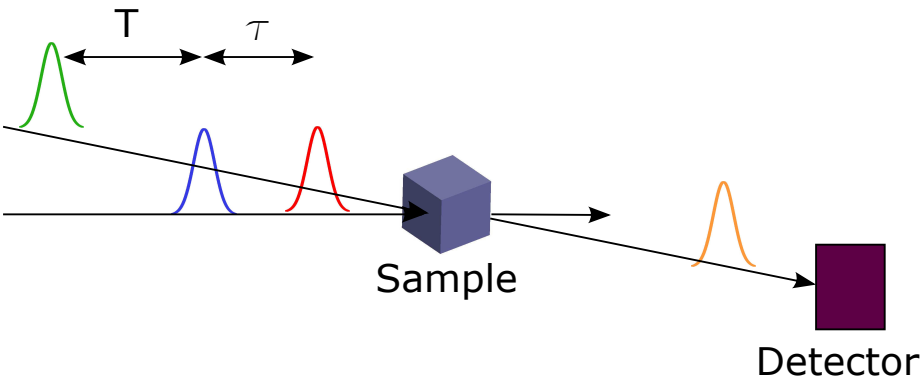

Figure 2.11: *Pump probe* geometry for 2D spectroscopy.

of the sample, the line broadening of the spectrum and the dynamics of the molecules. In order to understand how this is possible let's take a look of how the 2D maps can be analyzed.

2.4.1 Maps analysis

Bidimensional spectroscopy is a nonlinear spectroscopy technique that allows to measure directly the third order polarization. As seen in the previous section this term is equal to the nonlinear response of the sample, that is exactly it's physical evolution. The algorithm that allows to analyze data is the Fourier transform performed on both the time evolution and the temporal delay between the first two pulses. The map obtained will be a false color map resolved in ω_t and ω_τ. In order to understand the informations given by these maps let's consider in a first moment the so called *pump probe* geometry represented in Fig. 2.11.

In this geometry the first two pulses have the same $\vec{k}$-vector, while the third doesn't, and due to phase matching the nonlinear third order fields, *rephasing* and *non rephasing*, are generated in the same direction of the third pulse, like in the pump probe experimental setup. The first two phase-locked replicas are called *pump* pulses, while the third pulse is the *probe* pulse. Due to the collinearity between the probe and the third order field, the first is used as local oscillator for the heterodyne detection. Since $E^{(3)}$ is generated from the probe, these two pulses are already phase locked, and thus many experimental problems are eluded.

Recorded signals of transmission can be either positive and negative. Positive signals in these maps (red in figure) correspond to *stimulated emission* from excited atomic levels or *ground state photobleaching* like those obtained in pump probe experiments. Viceversa, negative signals (blue in figure) are associated

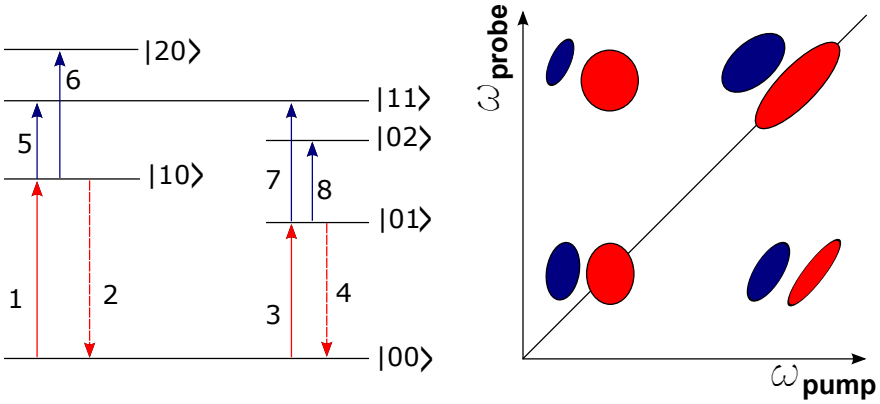

Figure 2.12: Example of 2D spectroscopy map.

to *photoinduced absorption* from the sample.

In pump-probe geometry an example of 2D maps that can be obtained for a *coupled system* is shown Fig. 2.12. The first information 2D maps give is contained is the position of the peaks [9]. Resonant transitions are the *diagonal peaks* that give the information about the possible transitions of the sample. The information that can be retrieved are the same than the one obtained with a simple absorptive spectroscopy measurement. In example in Fig. 2.12 these signals are the *stimulated emission* or *photobleaching* of the ground state (transitions 1+2 and 3+4 in figure)and are associated to single harmonic oscillator taken individually. It means they tell something about the each excitation mode that can be activated.

On the other hand the hallmark of bidimensional spectroscopy are the *cross peaks* that appear off the diagonal of the 2D matrix. These signals are due to any coupling and energy transfer inside the molecule, i.e. inter-level de-excitation, intersystem crossing, etc. In Fig. 2.12 these kind of transitions are both positive or negative (transitions 5, 3, 7, 1) [7] [10] [11]. These terms represent all the possible energy transfers that the ultrafast broadband pulses can stimulate. From this statement it is clear why 2D spectroscopy is giving very important information about the sample. The additional information gained is the *spectral resolution* in terms of pumping frequencies that allows to identify the origin of the emissions or absorptions.

There can be some other peaks positioned just by the diagonal ones (transitions 8 and 6). These are corresponding to some absorption from the excited state, and thus correspond to *excited state absorption*. Their position just on the side of the diagonal is due to anharmonicity of the oscillators. In the case of perfect harmonic oscillator these peaks are positioned exactly on the diagonal

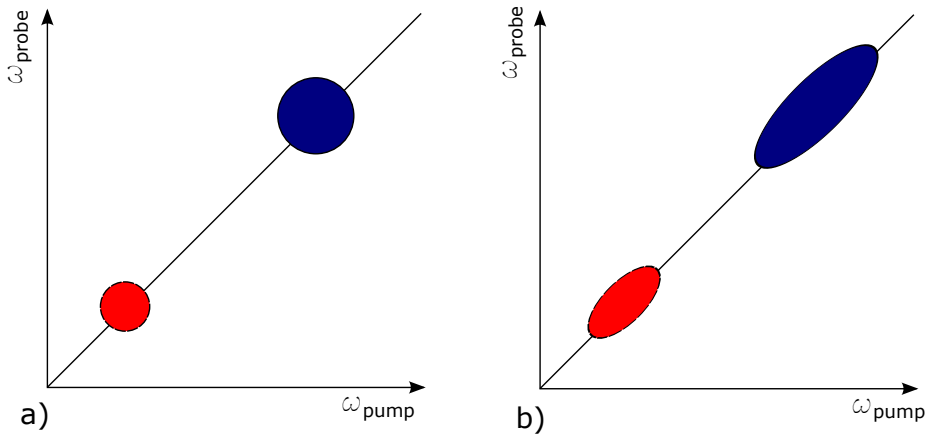

Figure 2.13: a) Map obtained from a 2D spectroscopy experiment on homogeneous isolated system. b) Map obtained from 2D spectroscopy experiment on inhomogeneous isolated system.

and thus they add perfectly with the other signals.

Bidimensional spectroscopy allows to obtain also other information about the composition of the sample. Indeed not only from the position of the peaks but also from their shape it is possible to retrieve important features of the target. One of them is directly connected to the line broadening of the spectrum, i.e. it is possible to distinguish between *homogeneously* and *inhomogeneously* lineshapes. If spots are perfectly circular, this means that only a certain oscillatory mode has been activated. This is the case of *homogenous* broadening in which the pump pulses are resonant with the characteristic oscillation of the dipoles of the sample. For *inhomogeneous* samples the spots assume an elliptical shape with the elongation in along the diagonal direction. The physical meaning of this behavior is that pumping with ultrashort broadband pulses many resonant harmonic oscillators are excited. Graphically the elliptical shape obtained by this systems can be seen as many adjacent rounded spots, each centered at its own resonant frequency. In Fig. 2.13 are compared the two cases of *homogeneous* and *inhomogeneous* broadening, while in Fig. 2.14 is represented the schematically explanation for the elongated shape of mixed states.

2.4.2 Setup geometries

The more complicated but complete possible geometry is called **boxcar** geometry. In this configuration the three excitating pulses are neither collinear nor coplanar like is possible to see in Fig. 2.15.b). The pulses instead are positioned at the vertices of a square so that the $E^{(3)}(t)$ *rephasing* field is generated along the fourth corner, i.e. along the $k_1 - k_2 + k_3$ direction. The local oscilla-

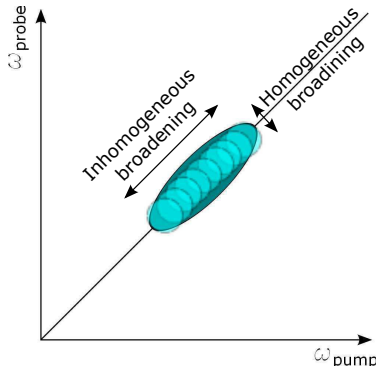

Figure 2.14: Schematically explanation of inhomogeneous broadening elliptical shape.

tor pulse is thus sent along this direction and the heterodyne detection occurs. The interesting feature of this configuration is that the *free induction decay* field is *background free*, hence problems connected to saturation of the detector are avoided. Since in two-dimensional spectroscopy both the *rephasing* and *non rephasing* signals must be collected, an interesting trick can be used. The phase-matched direction of the *non rephasing* is $-k_1 + k_2 + k_3$ where only the first to are signs of $\vec{k}$ vector are inverted. Therefore by reversing the temporal delay between the first and the second pulse the *non rephasing* signal is revealed at the fourth corner of the square. Thus *boxcar* geometry allows to perform the analysis very easily. The amount of information retrieved by this setup are the widest possible since it is possible to play on quite all the degree of freedom of the measurement. On the other hand its main limit is to set up the phase relation between all these pulses and their delay control.

For these reasons another geometry can be introduced: this is the **pump probe** geometry that has the two pump pulses with the same propagating direction. The third pulse, also called probe pulse due to the strict connection with the pump-probe experimental configuration, is tilted respect to that direction. In Fig. 2.15.c) this setup is sketched. The advantage of this technique is that the nonlinear polarization emits the field along the same direction of the probe pulse, making these two pulse collinear. Since the two pump pulses have the same $\vec{k}$ vectors both the *rephasing* and *non rephasing* signals have the same direction. This make the measurement easier not involving the reversing of the order of the two pump pulses. Between the probe and the generated pulses there is a well-defined phase relation since one is almost generated by the other. This is very useful for the heterodyne detection that need that the local oscillator is phase locked with the *free induction decay* field. From what has been said, it follows that the most challenging experimental part in this

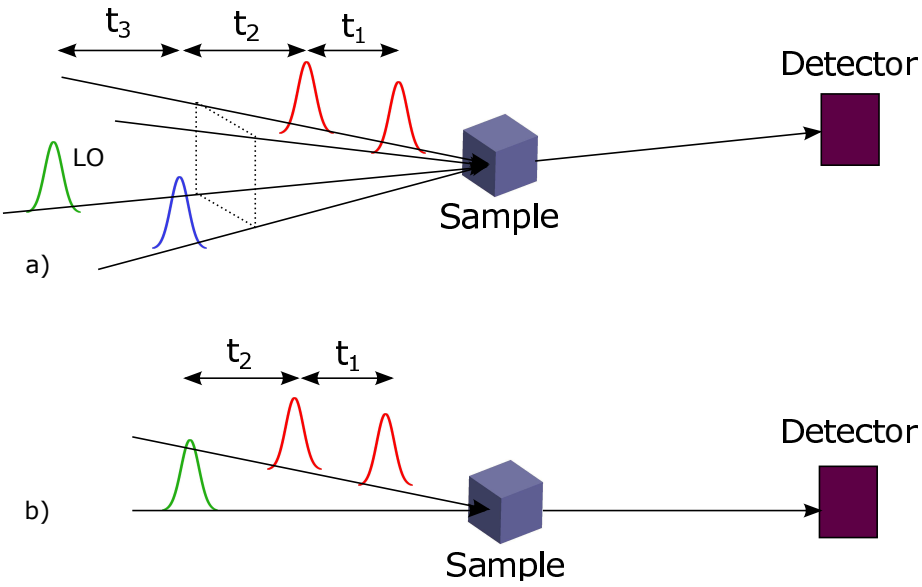

Figure 2.15: a) Setup for Boxcar 2D spectroscopy. Red pulses are those that generate the population state. Blue pulse stimulate the third order polarization that is detected by heterodyne detection with the green pulsed local oscillator (LO) on the detector. b) Pump-probe configuration for 2D spectroscopy experiment. The two red pump pulses are collinear. The probe pulse is collinear with the target signal and thus it acts as local oscillator for the detection.

configuration remain connected to the delay and phase relation between the pump pulses. Many technique have been proposed in order to resolve this task. These will be presented for different spectral regions in the next chapter. To conclude this kind of geometry allows to obtain many information, even if they are limited by the number of factors on witch it is possible to play. Indeed in this case like in Pump probe spectroscopy the $\vec{k}$-vectors of the first two pulses and of the last two are the same but this time it is possible to control the delay between the pump pulses. The situation is thus:

$$\begin{aligned} \vec{k}_1 = \vec{k}_2 \qquad &\Rightarrow \qquad \tau_1 \neq 0; \\ \vec{k}_3 = \vec{k}_{LO} \qquad &\Rightarrow \qquad \tau_3 = 0. \end{aligned} \tag{2.28}$$

Chapter 3

Two-dimensional spectroscopy with birefringent wedges

As presented in the previous chapter, two bidimensional spectroscopy geometries are possible and both present advantages and drawbacks. The photon-echo signal can be detected via an homodyne detection (pump probe configuration) or via heterodyne detection (boxcar geometry). The main advantage of the former is that the signal of interest is generated along the probe direction. Since in our laboratory the pump-probe setup are at the bases of all the measurements, it's quite immediate to think that turning this into a 2DES setup in the pump probe geometry is the easier and more common choice.

In order to collect 2D signal it is crucial to control the relative phase between the pulses. In particular, in the pump probe configuration it is required that the first two pump pulses must be *phase-locked* to avoid interferometric instabilities. To do that, several devices are available and will be discussed in the chapter. In our group has been recently proposed an innovative method based on birefringence of the material in order to control the relative phase of the pulse. In this chapter this new and compact device will be presented and characterized.

3.1 Techniques of phased-locked pair pulse generation

Due to the strictly condition on the phase relation of the first two pulses in the bidimensional spectroscopy, many solutions have been proposed. The easiest one is based on a simple Mach-Zehnder interferometer but other more sophisticated techniques are developed, based on pulse shaper or on birefringent media and here are reported.

3.1.1 Generation of phased locked pulses by Mach-Zehnder interferometer

A very intuitive way to obtain a phased locked pair of pulses involves a Mach-Zehnder interferometer visible in Fig. 3.1 [2]. A first beam splitter (BS in figure) divides an incoming pulse into two weaker identical replicas that are then recombined by a second beam splitter with a certain delay one respect the other. The delay introduced is given by the difference of optical path between the two arms of the interferometer. By controlling with a motorized translation stage the position of the optical delay line (ODL), it is possible to finely control the delay between the two pulses. This solution is very easy to implement, but its main disadvantage is that the two pulses see different optical components that, due to their vibration, introduce different phase contributions. This means that this device fits mainly with wavelength long enough respect the vibration introduced by the optics: the less is the number of optics, the lower are these phase fluctuations. Indeed this set-up is used with IR radiation where the wavelength is on the order of μm. If shorter wavelength are involved, those vibrations give a non negligible contribution. This means that for visible or UV light this system of pair pulse generation is not suitable and other devices must be used.

3.1.2 Generation of phased locked pulses by pulse shaper

A more complicated and expensive solution to the non-trivial problem of the generation of the two pump pulses involves a *pulse shaper*. A pulse shaper is a system that allows to have fully access to the spectral phase and spectral intensity of a pulse. The schematic idea is represented in Fig. 3.2. It is composed of two gratings and two lenses. The first grating disperses the spectral component of the impingent pulse in different direction, while the first lens collimates this divergent beam since it is positioned at a distance equal to its focal length f. From the lens the beam is collimated and travels until the second lens positioned

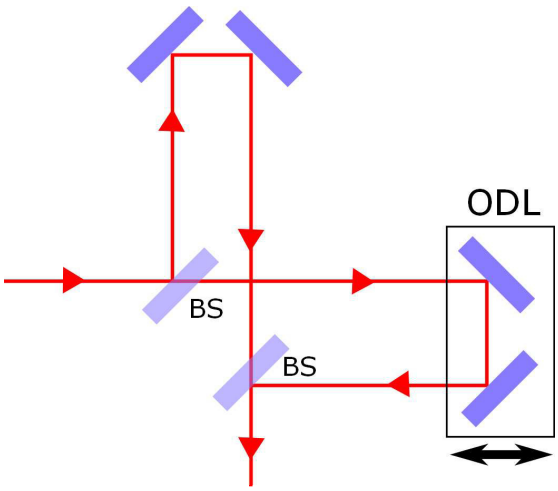

Figure 3.1: Mach-Zehnder interferometer scheme for the generation of a pair of phased locked pulses in the IR spectral region. The two beamsplitter (BS) divide and then recombine the pulse. The optical delay line (ODL) allows to control the delay between the two replica. [2]

at a distance equal to $2f$ from the first. The effect of this optical element is to focus the beam on the second grating that recombine all the spectral component.

Due to the physics of this system, in the between of the two lenses, at a distance f from both, there is the Fourier transform of the pulse, and thus it is possible to directly act on its the spectral phase and intensity. Here is where the *shaping*acts and the associated plane is called Fourier plane. By inserting different kind of modulators it is possible to give a phase modulation or an amplitude modulation in order to be able to obtain any desired pulse at the output of the pulse shaper.

Pulse shaper can be realized both in transmission or in reflection. The geometry is always the same but working in reflection space and costs can be limited. Concerning a pulse shaper in the reflection geometry, on the Fourier plane there must be some reflective optical media, like a mirror. To modulate it can be used for example deformable mirrors [12] [13] [14].

In order to generate two pulses one possibility is to put an acousto-optic modulator (AOM) on that plane and to deform it in a suitable way. As it has been said on the Fourier plain there is the Fourier transform of the pulse, i.e. its spectrum and thus multiplying it by a certain function it can be modulated. Indeed mathematically this can be explained by thinking that

$$E_{out}(\omega) = E_{in}(\omega)M(\omega) \tag{3.1}$$

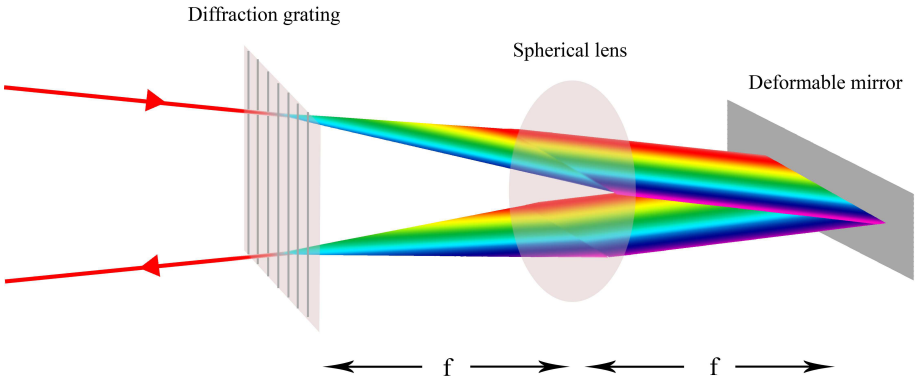

Figure 3.2: 4-f pulse shaper scheme.

where $M(\omega)$ is the mask function. To generate two pulses delayed bu τ the mask function can be written as:

$$M(\omega) = \frac{1}{2}(e^{i\omega\tau} + 1) \tag{3.2}$$

which Fourier transform is a train of two deltas function one centered at $t = 0$ and the other at $t = \tau$. Thus this mask function generates a fixed pulse at $t = 0$ and one at delay τ. By controlling via software the acousto-optic modulator it is possible to finely control the delay τ. [15]

Basically the acousto-optic modulator is an acoustic wave that propagates into a material. Since light is faster than this wave, this wave acts as a transient grating that deflect the desired frequencies with specified intensity and phase. This wave is controlled by a waveform generator in a computer in order to be able to apply different delays τ. The scheme just presented can be seen in Fig. 3.3.

The pair of pulses generated by the pulse shaper is phased locked since the two pulses pass through the same optical elements. The main advantage of this device is the tunability from IR to UV radiation: the shaper can be re-adapted by changing the type of grating and the lenses. The drawbacks of this system is the complexity of the device and the high cost.

3.1.3 Generation of phased locked pulses by birefringent media

An alternative solution proposed in our group exploits the birefringence of the optical material. The difference of the refractive index along different crystallo-

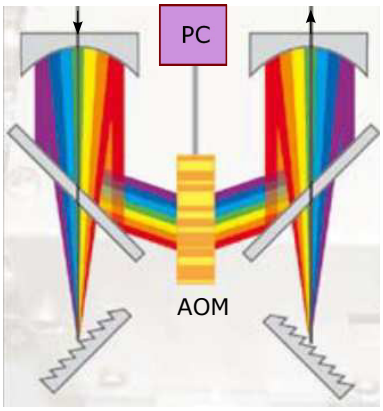

Figure 3.3: Example of acousto-optic pulse shaper.

graphic axis, i.e. birefringence, is used to generate two pulses that travel with different group velocity along different polarization axis. By changing the thickness of the birefringent material it is possible to vary the temporal delay between the pulses. This innovative device is called TWINS: Translating Wedge Based Identical Pulses eNcoding System.

Thus the birefringence creates two orthogonally polarized replicas from the incident beams and, thanks to a translating wedges system, it is possible to control the delay of these two with high accuracy. Let's go more in the detail of how this setup works.

3.2 TWINS

3.2.1 Birefringence

Optical crystals are ordered anisotropic media that behaves in different way depending on the optical properties of an incident beam. In these kind of optical object it is possible to define three orthogonal directions, the so called *main axis*, along which different refractive indices are detected.

Linear polarization is a non isotropic function of space and thus

$$\vec{P} = \epsilon_0 \chi \vec{E} \tag{3.3}$$

where χ is the electric susceptivity that is a tensorial operator. In the crystallographic frame of reference it can be diagonalized and the polarization can be

expressed as

$$\begin{aligned} \vec{P}_x &= \epsilon_0 \chi_x \vec{E}_x \\ \vec{P}_y &= \epsilon_0 \chi_y \vec{E}_y \\ \vec{P}_z &= \epsilon_0 \chi_z \vec{E}_z \end{aligned} \tag{3.4}$$

where the Cartesian coordinates of the polarization and the electric field are related by the *main values* of the electric susceptivity. On the basis of this values it is possible to define three classes of anisotropic crystals:

- *Isotropic Crystals.* These crystals have $\chi_x = \chi_y = \chi_z$. The electric field is thus parallel to the generated polarization.

- *Uniaxial Crystals.* When two of the main values are identical but one is different, i.e. $\chi_x = \chi_y \neq \chi_z$, the media is called uniaxial crystal. This class can be used as isotropic crystals if an electromagnetic field propagate along the z-axis. In this case the ellipsoid can be seen as a rotation along this axis and hence it is called *optical axis.*

- *Biaxial Crystals.* This is the case of $\chi_x \neq \chi_y \neq \chi_z$ that means the the crystal has not a preferential crystallographic direction for the polarization. This class of anisotropic material is used for *trirefringent* experiments.

The class of interest in the TWINS setup is the second one, i.e. the uniaxial crystals. Let's define as *optical axis* the only axis of the crystal identified by the χ_z term. If $\chi_z > \chi_y, \chi_x$ the material is defined as *uniaxial positive*, otherwise if $\chi_z < \chi_y, \chi_x$ it is called *uniaxial negative.*

If now the refractive index n is introduced, due to the connection to the electrical susceptivity ($n = \sqrt{1+\chi}$), in any anisotropic material it has different values along different directions. In particular it is possible to demonstrate that it depends on the direction of the propagation of an incoming electromagnetic radiation and on its polarization, i.e.

$$n = n(\vec{k}, polarization). \tag{3.5}$$

This equation takes the name of *index ellipsoid* and it describes the magnitude of the refractive indices in crystals. Due to the definition of the refractive index it is possible to define refractive indices n_x, n_y and n_z that are respectively the indices seen along the x, y and z direction, they are defined as the *main refractive indices.* The anisotropic crystals can be classified in the same three classes seen before but on the basis on the refractive index.

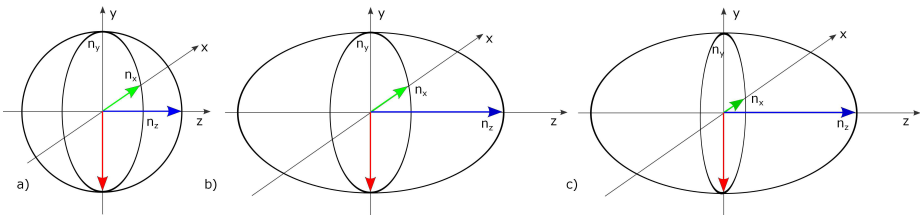

Figure 3.4: Index ellipsoid for anisotropic crystals.
a) Isotropic Crystal $n_x = n_y = n_z$.
b) Uniaxial Crystal $n_x = n_y, n_x < n_z$.
c) Biaxial Crystal $n_x < n_y < n_z$.

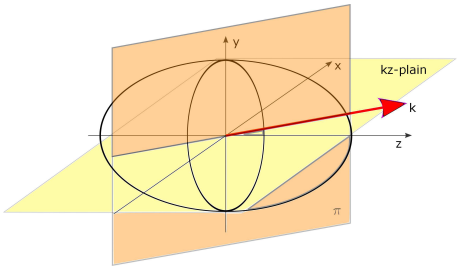

Figure 3.5: Index ellipsoid seen by the electromagnetic field.

The index ellipsoids in these three type of crystals are represented in Fig. 3.4.

From what it has been said, the *optic axis* in an uniaxial crystal is the direction along which an electromagnetic wave can propagate seeing only an ordinary refractive index for any polarization. The behavior of the crystal in this case is the same than the one of an isotropic media.

When the electromagnetic wave impinges the crystal, we can define the π plane as the one orthogonal to the direction of the propagation (and so to the $\vec{k}$-vector) and the *main plane* as the one delimited by the optical axis and the $\vec{k}$-vector. The field components are projected along the π plane, in the orthogonal and parallel direction respect to the main plain. In this way the refractive indices seen by the electromagnetic radiation are defined. The parameter that influence the amplitude of these refractive indecis is the angle θ in the main plain between the $\vec{k}$-vector and the optical axis. Fig. 3.5 represents all these components.

Let's write the *index ellipsoid* as

$$\frac{x^2}{n_x^2} + \frac{y^2}{n_y^2} + \frac{z^2}{n_z^2} = 1 \tag{3.6}$$

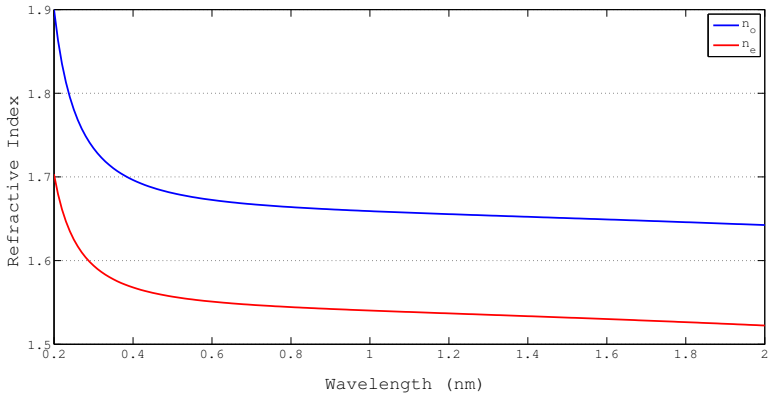

Figure 3.6: Sellmeier equation for α-BBO.

If the field has the *main* plain along xz this equation simplifies as

$$\frac{x^2}{n_x^2} + \frac{z^2}{n_z^2} = 1 \tag{3.7}$$

By expressing the Cartesian axis as the precession of the index it is possible to see that the extraordinary index depends on θ by

$$\frac{1}{n_e^2(\theta)} = \frac{cos^2(\theta)}{n_o^2} + \frac{sin^2(\theta)}{n_e^2(\theta)} \tag{3.8}$$

Let's consider an example of uniaxial crystals, the α-BBO. In Fig. 3.6 are represented the Sellmeier equation associated to this material. An incoming beam can be projected along the two optical refractive index so that two replicas of the pulse can be generated at different times, due to the dispersion of the material. α-BBO is a negative uniaxial crystal since $n_e < n_o$. The phase velocity is defined as the speed of any frequency, being c the speed of light in vacuum,

$$v_{phase} = \frac{c}{n} \tag{3.9}$$

while the group delay is the speed of the wavepacket defined as

$$v_{group} = \frac{c}{n_{group}} \tag{3.10}$$

where n_{group} is calculated as

$$n_{group} = n(\lambda_0) - \lambda_0 \left[\frac{dn}{d\lambda}\right]_{\lambda_0} \tag{3.11}$$

with λ_0 defined as the central wavelength of the pulse.

Due to this velocity mismatch the two orthogonal component of the incident radiation can be delayed one respect the other. How this is done will be presented in the next section.

3.2.2 Setup

In the 2D pump probe configuration (Fig. 2.7), the two pump pulses must be collinear, phase-locked and relatively delayed with high accuracy. The TWINS device is a compact and easy to implement system that generates such pulses.

TWINS set-up can be presented as three different blocks: A,B and C, as represented in Fig. 3.8. [16] The difference between these components is in the direction of the optical axis. Let's consider a set of Cartesian coordinates x, y and z where z is the propagating direction of the incident pulse. First block A has the optical axis, i.e. the extraordinary axis, along the y-direction (y-cut), block B has it oriented along x-direction (x-cut), while the third component C has this axis parallel to the z-direction (z-cut). These three blocks differ not only for the direction of the extraordinary axis, they are different in shape: block A must have a constant thickness d_A, while blocks B and C can vary their thicknesses d_B and d_C respectively, but under a certain condition:

$$d_B + d_C = const. \tag{3.12}$$

In this way the overall thickness of the TWINS will be constant too. In order to have these degree of freedom on d_B and d_C these blocks are not rectangular shaped, as block A is, but they are both wedges pairs. By extracting or inserting one wedge respect to the other for each block, the single thickness of a block can be varied. To satisfy Eq. 3.12 if d_B is reduced, i.e. one of the wedges of block B is extracted, d_C must increase of the same amount, meanings that one of the two wedges of the C block must be inserted, in order to maintain constant the overall thickness the the setup. In order to be able to control the movement of both the two wedges they are mounted on the same translation stage.

Let's consider an incident pulse propagating in the z-direction, polarized at 45° respect x and y. When light hits the block A the π-plain by construction is the xy-plain while the main one is the xz-plain. This means that the electric field component are projected from 45° to the x and the y axis with the same intensity. Since block A is y-cut, on the y-direction light sees the extraordinary refractive index, while on the x-direction there is the ordinary one. This difference of refractive indices affect the velocity of the two electromagnetic components. The one that sees n_e will travel faster than the one that sees n_o since α-BBO is a negative uniaxial crystal. The relative delay at the end of block A

between the two orthogonally polarized component results

$$\tau_1 = d_A \delta_{eo} \tag{3.13}$$

with $\delta_{eo} = \frac{1}{v_{ge}} - \frac{1}{v_{go}}$, and v_{ge} and v_{go} group velocities of the extraordinary and ordinary beam.

Out of block A the two replicas travel again with the same speed but delayed by τ_A. When these two hit the x-cut B block, the first pulse now sees the higher refractive index, while the x component detects the smaller n_e. This is very important since the two replicas in this way can be set again at a zero delay by varying the thickness d_B and moreover it will be possible to scan from negative to positive relative delays. At the exit of this block the relative delay is expressed by

$$\tau_2 = (d_A - d_B)\delta_{eo}. \tag{3.14}$$

The block B has two main roles: the first is connected to the control of the delay by a linear dependence from variation of d_B, Δd_B. The second is connected to the phase lock, that is ensured to the fact the both the pulses pass through the same optical elements.

Let's now analyze the role of the third block C. It is again a pair of wedges and it has been already said it is needed to maintain the overall thickness of TWINS constant. It doesn't introduce any additional delay between the two pulses because of the position of the optical axis that this time is parallel to the propagation direction of the beams. The main role of this block is thus to valid Eq. 3.12. In this way the pulse that sees the same n_o refractive index in the last two blocks, i.e. the y-component, will arrive always at a fixed delay t_0. The x component will be delayed by τ_2 respect to the fixed one. Since one of the two pulses sees always a fixed optical path, it is possible to know the dispersion introduced by the birefringent material. The GDD_o calculated on the x component thus is fixed and can be compensated. This is very important when working with transform limited pulses in ultrafast nonlinear spectroscopy. It is possible to verify that the wedges movement affects the GDD of the y pulse by a factor $(GVD_e - GVD_o)\Delta d_B$, where GVD is the group velocity dispersion. In most of the cases this variation can be neglected since is very small.

After these three blocks thus there are two delayed phased locked pulses. In order to have the same polarization for both of them a polarizer must be introduced after block C.

For this 2DES experiment the already cited α-BBO is used which refractive indices a represented in Fig. 3.6. From their trends it is possible to see that this uniaxial crystal is transparent in a very wide spectral region, and so it has good optical properties even using ultrashort broadband pulses from UV to near IR.

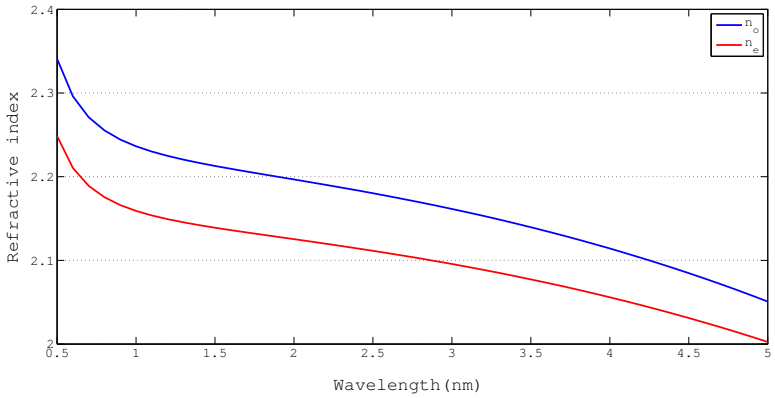

Figure 3.7: Sellmeier equation for Lithium Niobate ($LiNbO_3$).

In the case of mid-IR radiation this kind of wedges will not be the best solution, but they can be easily changed. Instead of α-BBO negative uniaxial crystal, it can be used a Lithium Niobate ($LiNbO_3$) which Sellmeier equations are shown in Fig. 3.7 [17].

Due to the difference between the phase velocity and the group velocity, defined in Eq. 3.9 and 3.11, between the two phase-locked pulses a delay-dependent phase difference is detected. Defining δ_{gp} as $\frac{1}{v_g} - \frac{1}{v_p}$ with v_p referred to the carrier frequency, it is possible to estimate this phase slip as

$$\begin{aligned} \Delta\phi &= (\delta_{gpx} - \delta_{gpy})\Delta d_B \\ &= (\delta_{gpx} - \delta_{gpy})\frac{\Delta\tau}{\delta_{eo}} \end{aligned} \tag{3.15}$$

where δ_{gpx} and δ_{gpy} are the δ_{gp} for the x and y component respectively, while $\Delta\tau$ is the relative delay variation due to Δd_B. This phase contribution will appear in the characterization of TWINS.

Note that blocks A, B and C are independent from each other and thus their disposition can be mixed and reversed. It will be shown later how the final setup looks in order to have a precise control of the position of the two sliding wedges.

3.2.3 Test of the setup

This setup has been tested in order to verify its stability and accuracy. The test involves the spectral interferometry, powerful instrument that can be used to retrieve many information on the pulses, even if it doesn't allow to retrieve the spectral phase and shape of it.

In Fig. 3.9 it is reported the experimental realization of the device. Since each component is independent the idea is to put the two translating wedge

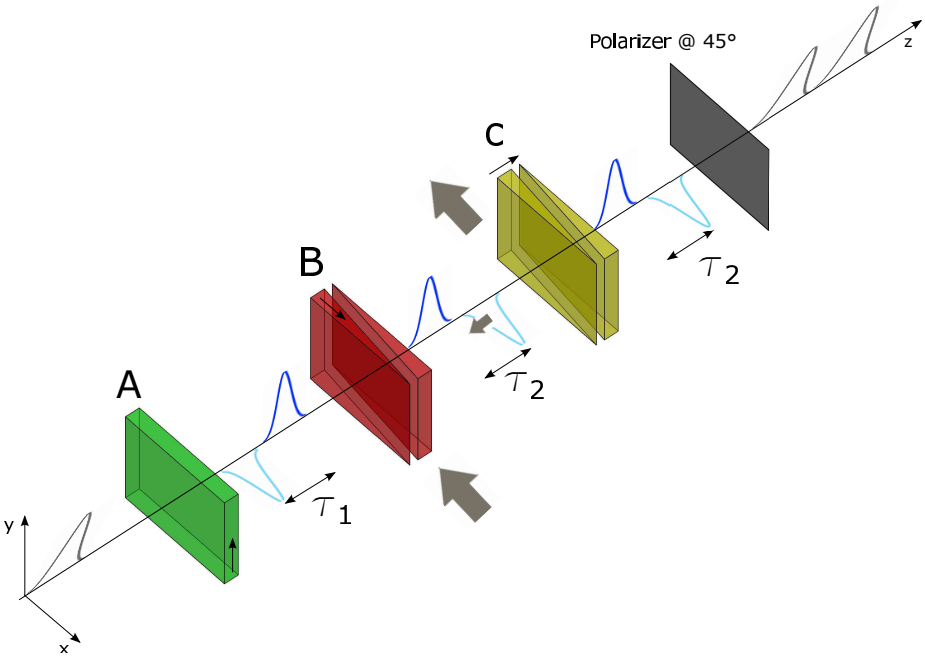

Figure 3.8: TWINS. Block A has a fixed thickness and introduces a fixed delay τ_1 between the two orthogonally polarized component of an incoming beam polarized at 45°. Block B by the movement of one of the two wedges is able to inverse the delay between the two replicas. The final delay is $\tau_2 = (d_A - d_B)\delta_{eo}$. Block C is needed in order to maintain the overall thickness of TWINS constant $d_A + d_B + d_C = const$.

together on a single translation stage in order to be sure that the two were moving of the same amount. Due to different cut of the wedges the second pair of mixed wedges is necessary to guarantee that the two beam travel again perfectly parallel. Since the thickness of the third block is kept fixed during the experiment, the other two wedges are placed at the minimum insertion.

The translation stage has a spatial resolution of 0.0086 μm. The wedges have a wedge angle of 7°, a minor thickness of 0.5 mm and a major thickness of almost 3 mm. Thus the delay resolution that TWINS have in this geometry is around 0.44 as (at $\lambda = 500$ μm).

The first test performed on the wedges is aimed to check if the setup is able to maintain fixed the delay of the *fixed delay* replica. This is done by spectral interferometry (SI). On one arm of an interferometer the TWINS device is placed while on the other arm, the light is freely propagating. Making interference between the fixed replica, i.e. the y component, and the same component of the free propagating beam, by scanning the stage it is possible to see that the interference pattern remained fixed. The setup used is sketched in Fig. 3.10. Once that all the imperfection due to a misalignment or to some irregularities in the crystal were corrected by the opto-mechanical mounts to verify that by moving the stage the arrival time of the fixed replica is always the same t_0.

Trying to analyze all the properties of the setup other tests have been performed. In particular a first simple test done is a spectrally resolved auto-correlation measurement of TWINS. In Fig. 3.11 are represented the pulse pair spectra associated to different wedges position, i.e. to different delay. These spectra are resolved respect the probe frequency in the NIR spectral region (vertical axis in figure). The bidimensional map obtained is the typical fringed pattern that can be obtained from auto-correlation measurements. The position associated to the zero delay between the two replica is detected by the dashed white line in the map. As it is possible to see on the left the fringes have a negative slope, while on the right, i.e. for delays bigger than zero, the slope is positive. This tilt is even bigger going to longer delays.

By making the Fourier transform with respect to τ (horizontal axis) of the 2D map, it is obtained the Fourier-dependent calibration of group delay τ, the residual group delay dispersion (GDD) and the relative phase slip $\Delta\phi$ introduced by a given wedge movement. The Fourier transform is shown in Fig. 3.12. From the tilt angle of the trace it is clear that different spectral components see different phase velocity. The new horizontal axis of the Fourier transform is composed by the so called *pseudo*-frequencies ν_τ, i.e. the physical variable associate to the Fourier transform of the delay (or wedges position). From the figure it easy to see that there is a shift between the probe frequency and the horizontal axis, indeed the transform is slightly shifted respect to the diagonal.

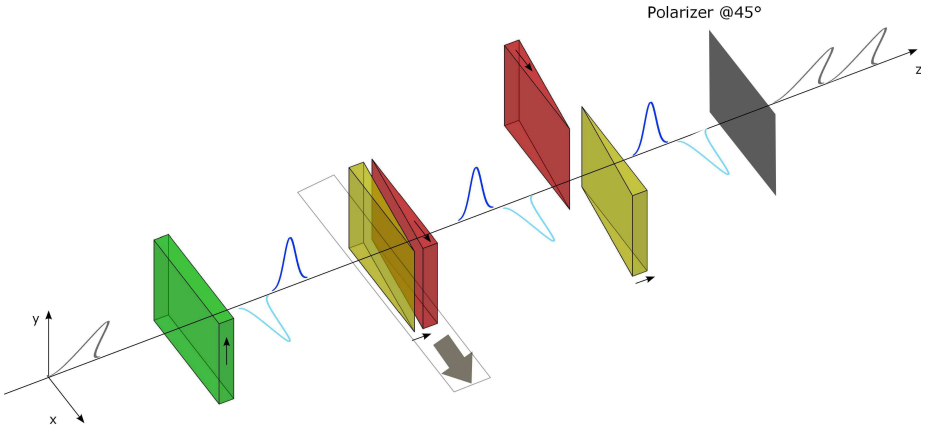

Figure 3.9: Setup of TWINS. The two translating wedges are combined together on the same translation stage. The fixed pair of wedges is needed to make the two beam walk again parallel. This variance of the setup is possible thanks to the independence of each element in the setup.

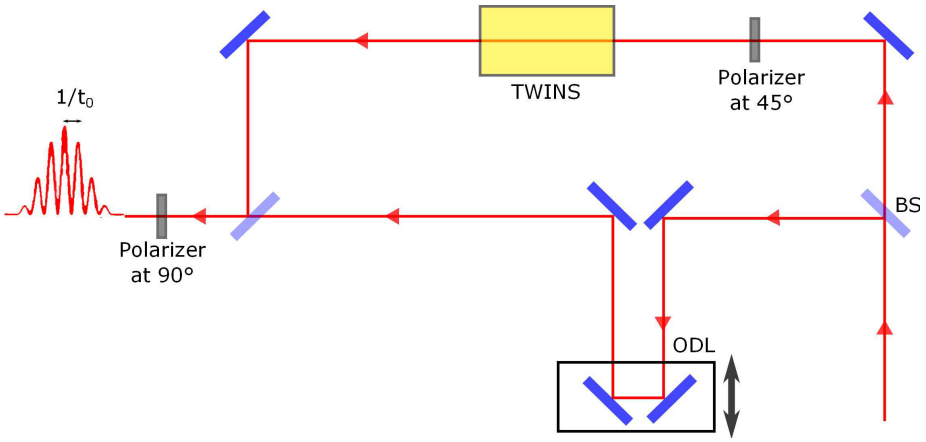

Figure 3.10: Simple interferometer involved in the measurement of the fixed delay t_0 of the y-polarized replica out of the TWINS.

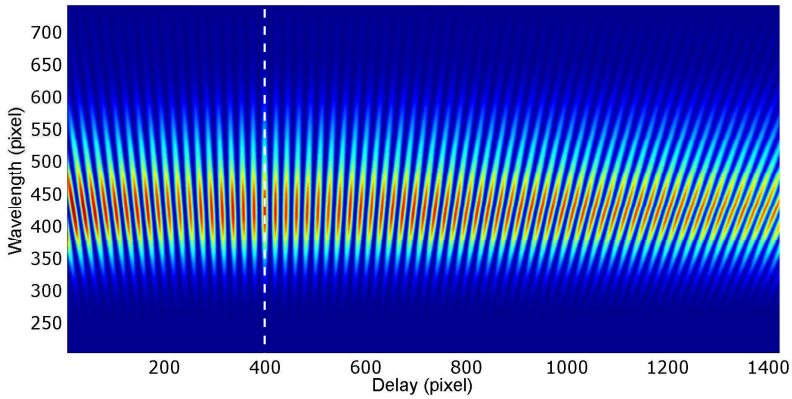

Figure 3.11: Interference fringes between the two pump pulses due to one complete scan of the translation stage. The white dashed line correspond to the zero delay position of the stage.

In order to be able to associate pump frequencies to the *pseudo*-frequencies hence a small contribution, approximately linear, must be taken into account. This shift of frequencies is due to the rotating frame related to the phase slip previously introduced. The *calibration* of the TWINS device hence contains all these information and is necessary for the analysis of the maps obtained from the 2D spectroscopy.

Another information that can be retrieved from the auto-correlation on the TWINS device it the auto-correlation function of the pump pulse. In Fig 3.13 is represented its the temporal behavior. Since the measurement is not performed symmetrically respect to the zero delay, the temporal trace is not centered at time zero. The nice shape of this function is due to the high precision and resolution of the considered setup.

3.2.4 Realization of the opto-mechanical components

To conclude this chapter it is presented the project and the realization of the opto-mechanical setup designed for TWINS. This concept must take into account all the imperfections connected to the imperfection of the shape of the wedges, to the cut of the crystals and the misalignment. Many idea were presented but the final one is sketched in Fig. 3.14. All the wedges are positioned as close as possible in order to reduce all the walk off between the two orthogonally polarized pulses. The home-made final setup is visible in Fig. 3.15.

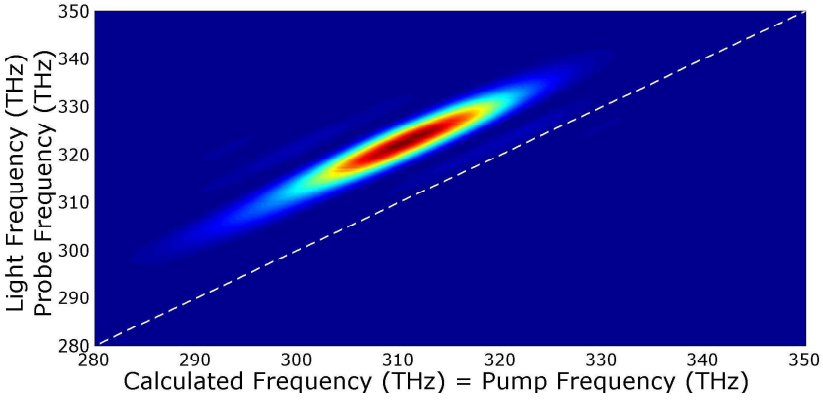

Figure 3.12: Fourier transform of the interference pattern obtained from the TWINS. Each frequency have a different phase velocity and thus the transform is tilted. The position off the diagonal (dashed white line) is due to the rotating frame related to the phase slip. From this data is retrieved the calibration needed in the 2D maps analysis. It allows to associate the right pump frequency to the relative delay of the pump pulses.

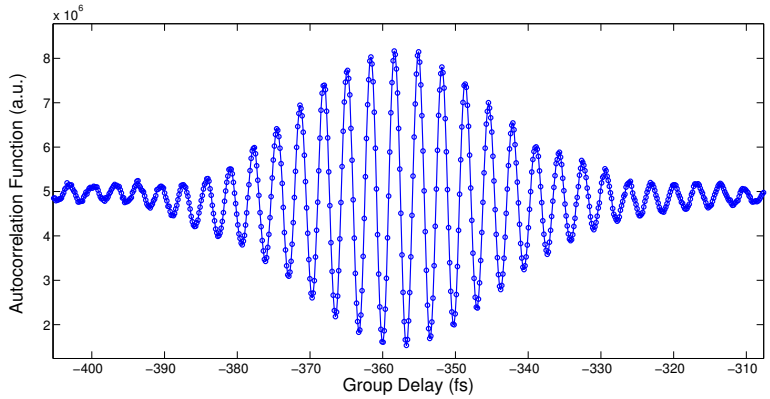

Figure 3.13: Auto-correlation function of the pump pulses retrieved by the auto-correlation measurement of the TWINS device.

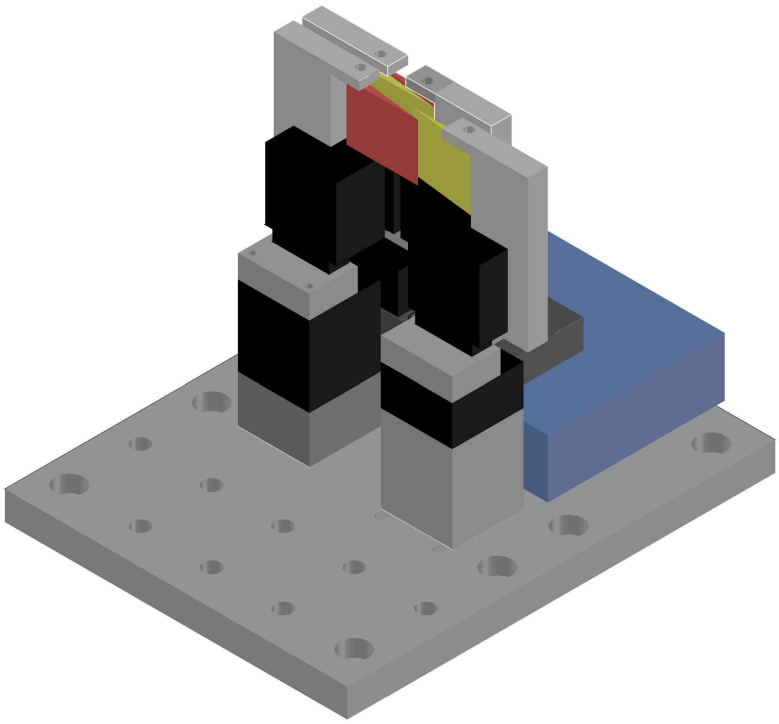

Figure 3.14: CAD project of the TWINS setup.

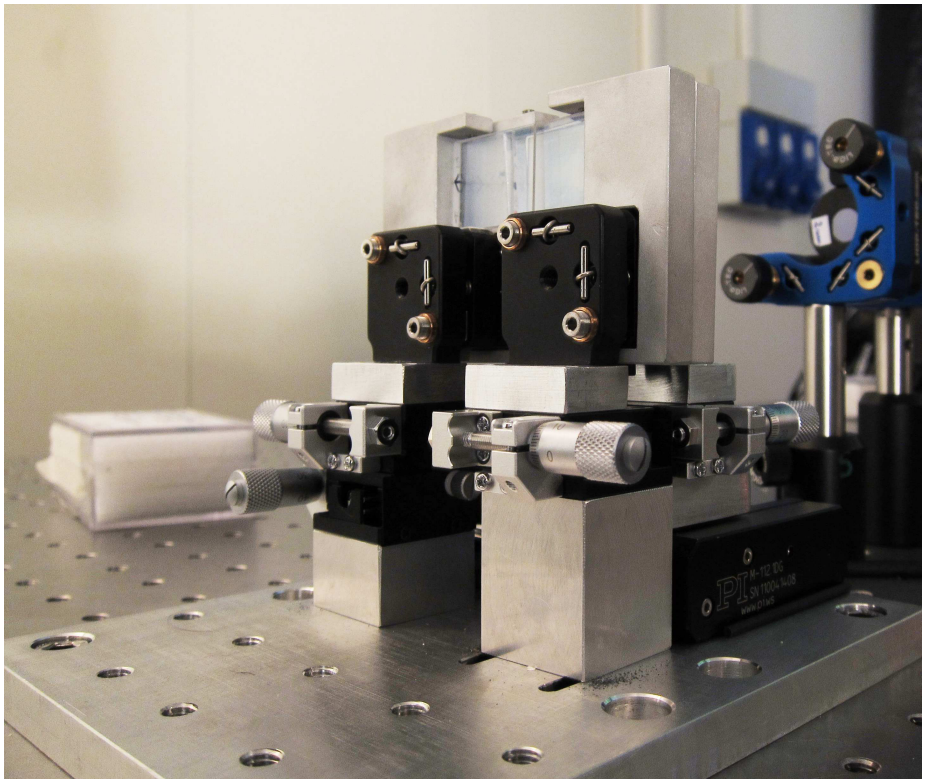

Figure 3.15: Real aspect of the TWINS.

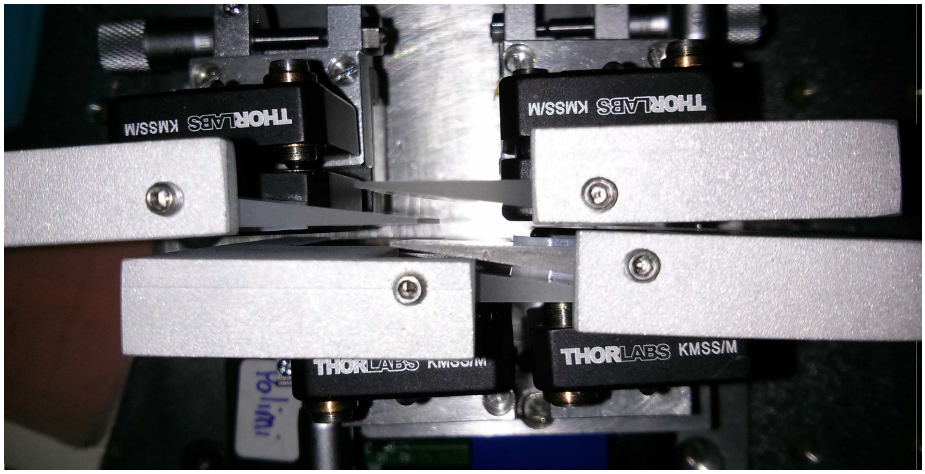

Figure 3.16: Real aspect of the TWINS. Top view.

Chapter 4

Experimental setup

This chapter describes the setup realized in the laboratory in order to perform bidimensional electronic spectroscopy experiments (2DES). It is first presented the light source used in the laboratory, then it is described the optical parameter amplifier (OPA) used for the experiment. The NIR radiation is energetic enough to excite electronic transitions, and thus to *electronic* spectroscopy [18]. This OPA emits ultrashort transform limited pulses in the near infrared (NIR) spectral region. The last paragraph describes setup built for the 2DES measurement.

4.1 Light source

The laser used in the laboratory is a Libra Ti:sapphire pulsed laser from *Coherent*. The basis of this laser is the Kerr-lens mode-locking technique that allow to have high pick energies pulses with short temporal duration. The limiting factor for pulses is the *time-bandwidth product* that limits the temporal duration of a pulse:

$$\Delta t \Delta \omega \cong 1. \tag{4.1}$$

It is possible to define this product to different pulse shape. Table 4.1 shows the time-bandwidth product for the more common pulse shapes.

Pulse shape	Time-Bandwidth product $\Delta t \Delta \nu$
Square	0.886
Gaussian	0.441
Hyperbolic secant square	0.315
Single sided exponential	0.110

Table 4.1: Time-bandwidth product for different pulse shapes.

In the time-bandwidth product formula the equality holds for *transform limited* pulses. If the different frequencies of the wavepacket are dispersed, equation 4.1 becomes

$$\Delta t \Delta \omega > 1. \tag{4.2}$$

The Libra Ti:sapphire laser is characterized by a pulse duration of less than 100 fs, by a 30 nm bandwidth centered at 790 nm (corresponding to 14 THz) and by a mean power at the output of 5 W at 1 kHz of repetition rate. Fig. 4.1 shows the constitutive blocks of the Libra system.

First block is the *Vitesse* that is the seed generator. This pulse is amplified in a regenerative stage based on a Ti:sapphire crystal pumped by the *Evolution*. In order to enhance the peak intensity of the outgoing pulse the amplification system used exploit the *chirped pulse amplification*. Thus a stretching stage and a compressing stage are present too.

In the *Vitesse* box there is a pump Verdi CW laser at 532 nm that is used into a cavity to pump a nonlinear crystal in order to generate a mode-locked seed. The generation is made into a Ti:sapphire crystal in which, after a perturbation, thanks to self focusing and hence Kerr lensing, mode-locking pulse emission take place. Out from the cavity thus there is a mode-locked seed that must amplified.

The amplification is realized into another Ti:sapphire crystal pumped by the second harmonic of a Q-switched laser at 527 nm generated in the *Evolution* cavity with a Nd:YLF crystal. This pump pulse is sent twice into the amplification crystal in order to maximize the pump efficiency. Working with pulses means to deal with extremely high peak energies and thus amplification processes must take into account different steps. The incoming seed is firstly sent into a *stretcher* that reduces the peak energy and disperse all the frequency components. Then the beam passes into the crystal several time in order to obtain a certain amplification. After some bounces the beam goes out from the regenerative stage and goes into the *compressor* that is a negative image of the stretcher, and thus put all the frequencies together enhancing again the peak energy. The outcoming beam thus will be *transform limited* and with a very high peak energy.

In order to control the amplification, two Pockels cells are introduced in the *regenerative* stage. Their role is to control the number of bounces into the amplification crystal. The more these bounces are, the higher the energy of the pulse is. In Fig. 4.2 is represented a scheme of *chirp pulse amplification* process while in Fig. 4.3 is depicted the only regenerative amplifier.

Pockels cells (PC-1 and PC-2 in figure) control the number of bounces of the stretched seed into the crystal. The first allows the entrance of the seed in

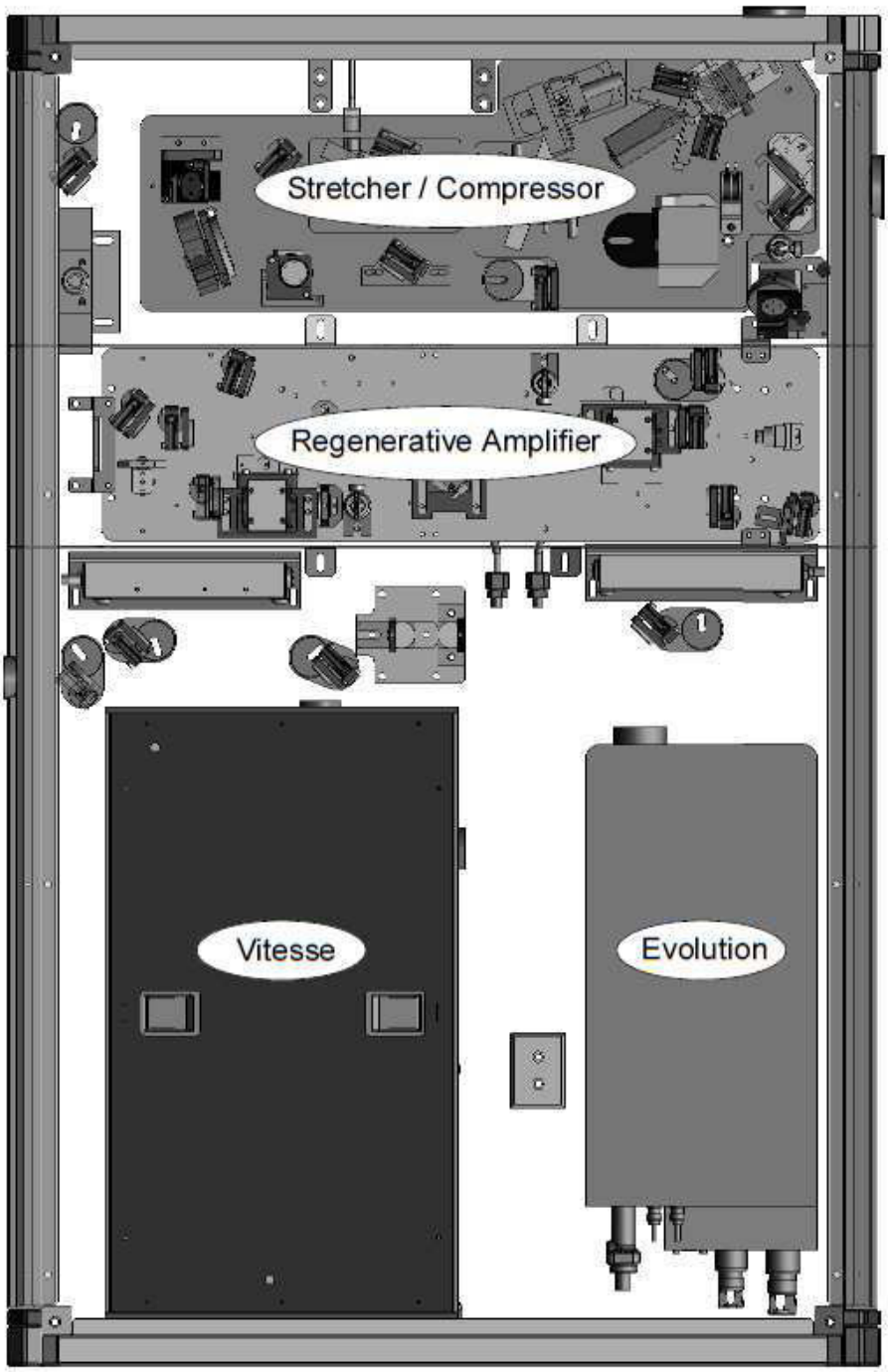

Figure 4.1: Setup of Libra laser from *Coherent*.

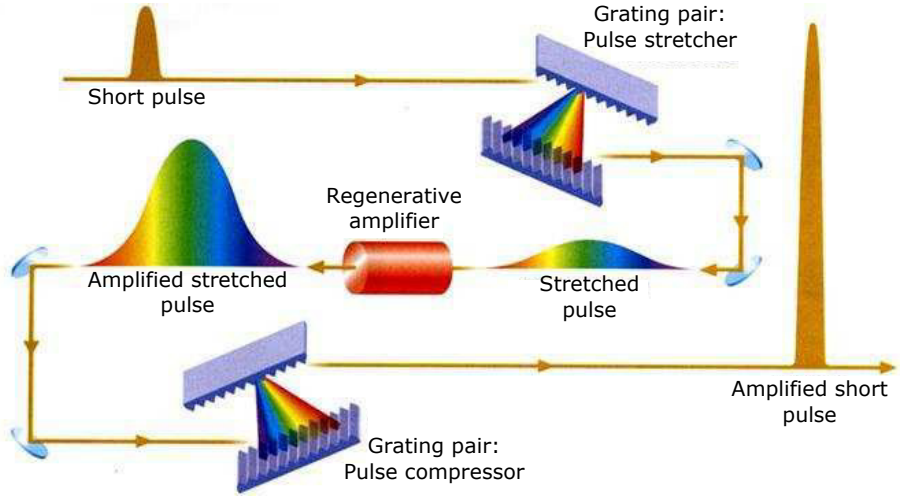

Figure 4.2: Scheme of chirped pulse amplification.

the regenerative stage, while the second controls the ejection of the amplified pulse. In standard configuration seed passes through the crystal five times. By controlling the delay of the Pockels cell it is possible to vary the number of reflection and thus the power of the laser. In the regenerative stage the pulse from the stretcher goes into the cavity and if the Pockels cells are OFF passes through the quarter-wave plate two times and thus its polarization is rotated by 90°. If the incoming pulse is s-polarized, thus it gain a p-polarization. Then the PC-1 is switched ON in order to maintain this polarization as long as the pulse remain in the cavity. Remind that with p-polarization it is possible to reduce the reflection losses by choosing the Brewster angle between light and amplification crystal. When the pulse has made enough bounces PC-2 is switched on and rotates the polarization of the beam again to s. Now the prism act as a mirror and reflects this polarized pulse away towards the compressor.

At the end of all these steps the resulting pulse outcoming from the Libra is transform limit with 5 W of mean power with a repetition rate of 1 kHZ and p-polarized.

In order to measure the beam size, a knife edge measurement it has been performed just out from the laser. The waist is almost round with circularity of 0.9 meanings that the horizontal waist is slightly bigger than the vertical waist. The mean value of the waist is near $4mm$, meanings that the diameter of the whole beam is near $8mm$. In Fig. 4.4 is reported an image of the beam made by an apposite camera from *Coherent*.

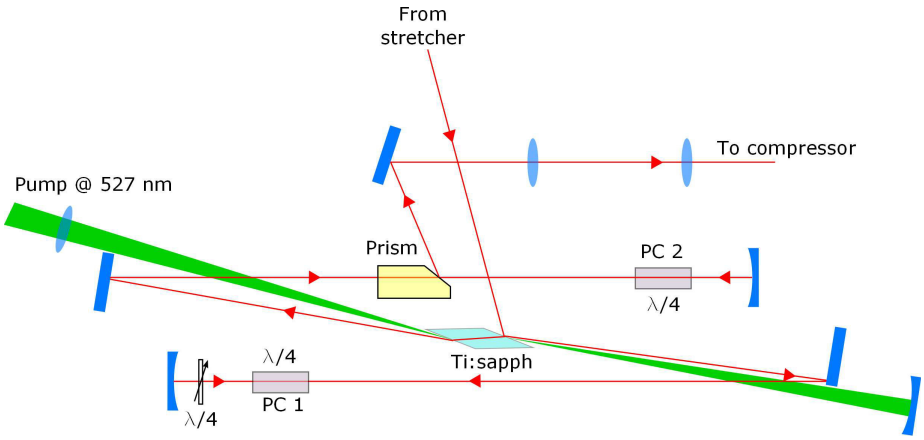

Figure 4.3: Regenerative stage of the Libra laser from *Coherent*. The green pump is folded in order to maximize its effect. The signal is passing through the amplification crystal a number of time set by the Pockels cells (PC1 and PC2).

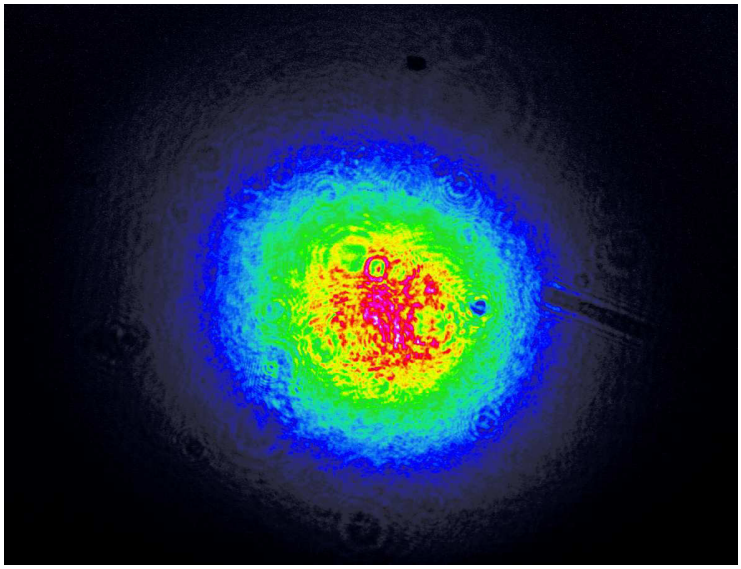

Figure 4.4: Beam spot of Libra laser from *Coherent*.

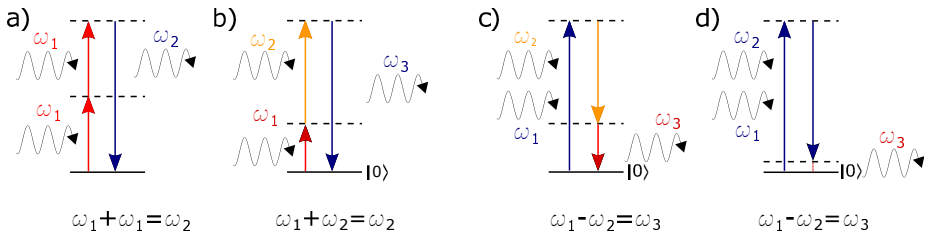

Figure 4.5: Second order nonlinear effects. a) *Sum frequency generation.* The two incoming pulse have the same frequency ω_1 and thus $\omega_2 = 2\omega_1$. b) *Sum frequency generation.* The two incident beam have different energies and sum up. c) *Difference frequency generation.* The third generated pulse is the difference of the first two. d) *Optical rectification.* The incoming two pulses have energies that are very close and thus the generated pulse is in the THz region.

4.2 Optical Parametric Amplifier

The Libra laser beam is used to yield broadband pulses. Such pulses can be generated by *optical parametric amplification*, a process occurring in nonlinear crystals. In particular it is a second order process like second harmonic generation (SH), sum frequency generation (SFG), difference frequency generation (DFG) and optical rectification (OR). All these phenomena represented in Fig. 4.5 involve two incoming beams that interact in order to generate the third, maintaining the overall energy constant. *Optical parametric amplification* (OPA) is a difference frequency generation process in which one of the two incoming pulses is more intense respect to the other.

Second harmonic generation is a nonlinear interaction where two identical pulses generates a pulse with twice the energy of the first two. Its frequency is thus $\omega_2 = 2\omega_1$, where ω_1 is the angular frequency of the incident pulses and ω_2 is the one of the generated beam. Sum frequency generation is the general case of second harmonic generation: if two incident pulses are different, the generated beam has a angular frequency that is the sum of the first two. Difference frequency generation instead is the a second order interaction in which from a high energy pulse, it is generated a low energy one. Since there is the need of three pulses a second incident pulse is needed and the relation between the angular frequencies is $\omega_1 - \omega_2 = \omega_3$, where $\omega_1 > \omega_2, \omega_3$. Optical rectification can be seen as a particular case of the previous case in which the two incoming pulses have almost the same energy. The generated pulse has a very slow angular velocity and thus is in the THz region.

All these effect are present every time that the two interacting pulses are synchronized in time and space when pass through a second order nonlinear crystal. It is possible to select one respect to the other thanks to the phase

matching that allows to make one of these nonlinear effect more efficient respect to the others. Phase matching can be done by angle tuning or by temperature tuning. In both the cases one second order process is enhanced.

Optical parametric amplification (OPA) is a second order nonlinear process in which the three acting pulse are defined as *pump*, *signal* and *probe* pulse. The pump pulse is the more energetic one at ω_P, the signal is the second incident beam, i.e. the seed at ω_S while the idler is the generated third pulse at ωI. Thus the relation between the three angular frequencies is $\omega_P > \omega_S, \omega_I$. Due to energy conservation, while the idler is generated, the signal pulse is amplified, i.e. for each pump pulses signal and idler pulses are generated (*parametric down conversion*).

In this amplification all the transitions that play role in the second order processes, are made upon virtual level and not upon real levels, as it occurs for laser amplification. This affects the band of the generated pulses that can be very broad. For this reason OPAs are very useful: it is possible to generate broadband ultrashort pulses in different spectral regions.

In order to understand how this amplification works let's consider a birefringent negative uniaxial crystal of BBO (β-Barium BOrate or β-BaB2O4) that allows to have second order polarization terms, i.e. it is a non-centrosymmetric crystal. The parametric amplification take place when the pump and the signal are overlapped in space and time. Thus OPAs must have a very accurate system for the delay tuning. In order to maximize the efficiency of the amplification the group velocity mismatch must be taken into account. The best condition for OPA is when the pump travels in the between of the idler and the signal, in this way the amplification is more efficient.

In order to understand what it has been said, it is necessary to consider the group velocity mismatch between two pulses and the pump defined as

$$\begin{aligned} \delta_{S-P} &= \frac{1}{v_{gS}} - \frac{1}{v_{gP}} \\ \delta_{I-P} &= \frac{1}{v_{gI}} - \frac{1}{v_{gP}} \end{aligned} \tag{4.3}$$

where v_{gS} and v_{gI} are the velocity of the signal and idler respectively, and v_{gP} is the group velocity of the pump. If the *pulse splitting length* is the maximum spacial length in which two pulses interact, it is defined as

$$\begin{aligned} L_{S-P} &= \frac{\tau}{|\delta_{S-P}|} \\ L_{I-P} &= \frac{\tau}{|\delta_{I-P}|}. \end{aligned} \tag{4.4}$$

The term τ in the equation is the maximum interaction time that is supposed to

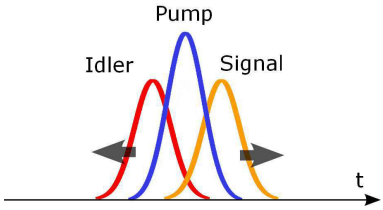

Figure 4.6: Best condition for *optical parametric amplification*. The pump pulse has a velocity that is between the one of the signal and the one of the idler.

be exactly equal to the pulse duration, that to simplify the analysis, is considered the same between the two interacting pulses. Considering the velocity of the signal and idler respect the pump, it is possible to see that

$$\begin{aligned} \delta_{S-P}\delta_{I-P} > 0 \quad &\Rightarrow \quad v_P < v_S, v_I \ \vee \ v_P > v_S, v_I \\ \delta_{S-P}\delta_{I-P} < 0 \quad &\Rightarrow \quad v_I < v_P < v_S \ \vee \ v_S < v_P < v_I. \end{aligned} \tag{4.5}$$

In the fist case the overall interaction length L will smaller than the one of the second case where it is bigger than the two pulse splitting length individually. This is due to the fact that if the pump travels between the signal and the idler, each time that the DFG occurs between the pump and the signal, the idler pulse will move in the direction of the pump. The same is true when the nonlinear effect occurs between the pump and the idler. Fig. 4.6 shows the optimum solution.

In order to maximize the tunability of these instruments the seed is a white light *supercontinuum*, in this way many component can be amplified in the same time. In order to extend the phase-matching band a non collinear geometry is chosen. This configuration is called NOPA: Non collinear Optical Parametric Amplifier. In this geometry the pump and the signal are not collinear and thus thanks to the angle that they form with the optical axis of the BBO, it is possible to play with the extraordinary refractive index seen by one of the two. This degree of freedom helps for the group velocity matching of the three pulses and hence on the bandwidth that linearly depend from this term [19]:

$$\Delta\nu_{FWHM} \propto \frac{1}{|\delta_{S-P}|} \tag{4.6}$$

After the parametric amplification it is possible to write the parametric gain of the signal and the idler as function of the pump pulse intensity I_P as

$$G \propto e^{\sqrt{I_P}}. \tag{4.7}$$

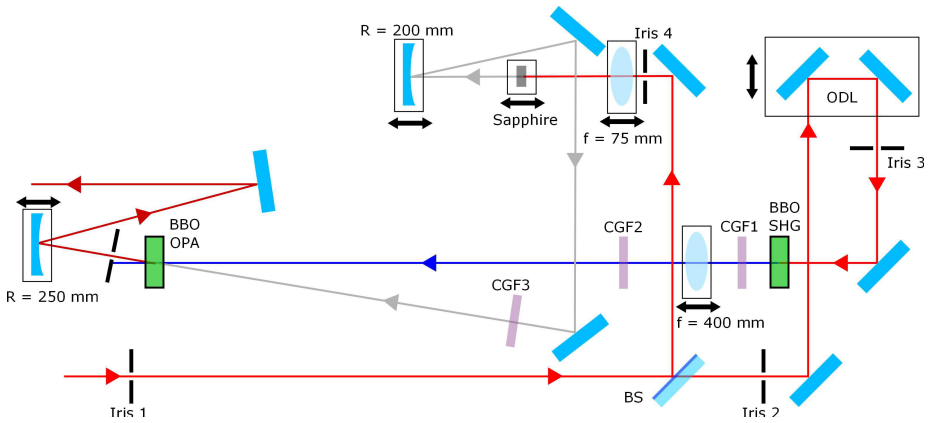

Figure 4.7: NIR-NOPA setup.

4.2.1 NIR-NOPA

The ultrashort broadband source realized for the experiment is a NOPA in the near infrared spectral region (NIR). In Fig. 4.7 is sketched the setup. Light from laser enters in the setup through Iris 1 and is divided into two replica by a beam splitter (BS) with reflectivity of 30% and transmission of 70%. The weaker replica is used for the white light generation by *supercontinuum* into a sapphire plate of 2 mm of thickens. The transmitted part is used as pump. Due to conservation of energy, to obtain a NIR pulse from the OPA, the pump must be the second harmonic of the laser beam (400 nm) and thus a second harmonic crystal is used. In order to remove all the residual non converted light two color glass filter (CGF1 and CGF2 in figure) are put into the path of the pump pulse. Pump and signal are crossed at a certain angle in order to take advantage from the noncollinear geometry. In order to amplify only the near infrared region of the white light, a black filter (CGF3) is introduced after the white generation: this filter removes all the visible components of the generated *supercontinuum*, leaving the infrared one passing through. In the focal spot where the pump and the seed are overlapped in space and time is positioned another BBO crystal that is the one that amplifies the frequencies of interest. In order to control the temporal overlap between pump and seed an optical delay line (ODL) is put along the pump walk.

Due to the geometry chosen the amplified signal is generated in the same direction of the incoming seed, while the idler pulse is generated in the opposite side respect the pump pulse. By tuning the angle of the BBO, i.e. by changing the phase matching, it is possible to tune the generated NIR pulse near the 800 nm or more in the infrared spectral region near 1050 nm. Due to phase matching by varying the central wavelength of the amplified signal, the idler is

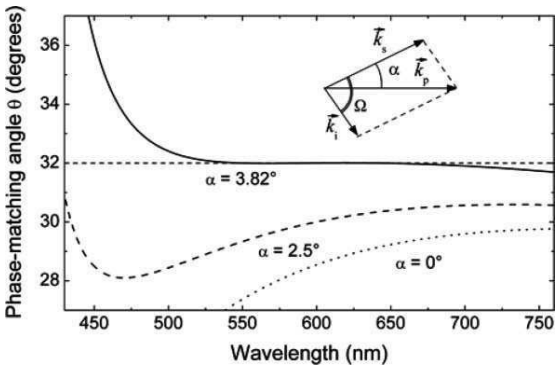

Figure 4.8: Signal wavelength dependence of the phase-matching angle in a BBO crystal with a 390 nm pump wavelength. [3]

also changing. For a signal tuned at 900 nm the idler is centered around 700 nm.

In order to obtain the widest bandwidth possible there are some rules to take into account in the realization of the setup. The main is the control of the angle between the pump and the seed. The best solution is to have an angle of $\sim 4°$ between the two, that means that at 35 cm from the BBO crystal the two beams must be at 2.5 cm one from the other. The BBO OPA crystal must have an angle of $\sim 30°$ respect the pump pulse. The best choice is thus to put a 32° cut crystal with the optical axis parallel to the polarization of the pump (i.e. horizontal) and to tilt it slightly. This can be seen also from Fig. 4.8 where is represented the signal wavelength dependence of the phase-matching angle in a BBO crystal with a 390 nm pump wavelength [3] [19]. In the NIR region, not represented in figure there is the need to tilt slightly the crystal. The phase matching is a Type II, that means that the signal and the idler will be orthogonally polarized. In the NIR-OPA realized the signal is vertically polarized this means that it sees the ordinary refractive index in the crystal.

In the final setup from the Libra laser only $400mW$ with $1kHz$ of repetition rate enters in the NIR-NOPA. The 70% will act as pump that passes through a second harmonic BBO. This second order process has an efficiency of almost the 30% but, due to filters set to remove the residual 800 nm radiation, the blue pump pulse has an energy of $40mW$. The white light generation is performed with only a portion of the radiation and thus it is done with only $2mW$ of power. The output generated signal has an average power of 2 μW at 950 nm and a band of nearly $100nm$. Since the generation is performed in dispersive media there is the need to compress the generate pulse after the optical parametric amplification. In next section is described how this can be done in the NIR spectral region.

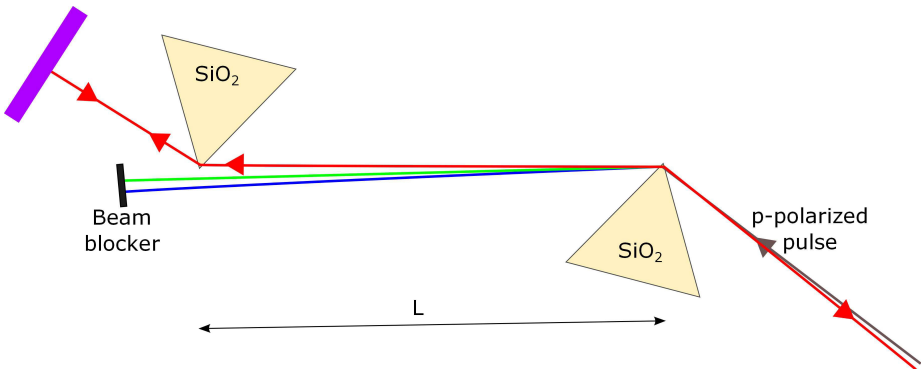

Figure 4.9: Prisms pair compressor.

4.2.2 Pulse compression

Dispersive media, i.e. all the optical materials involved in the setup, act in different manner on the different spectral component of the pulses going to vary the duration and the quality of the pulse. Thus the overall amplified pulse has a certain chirp that must be compensated. The dispersive media that affect the NIR pulses are the air and all the optical transmitting component that are involved in the setup, i.e. lenses, sapphire plate and crystals.

Pulse compression must act on the different spectral component individually in order to be able to remove the different optical path seen by each. Thus there must be introduced other dispersive media but with a overall dispersion that has the opposite sign of the one generated in the setup. Since all the dispersive media involved introduce a positive dispersion, the pulse compression is performed by the insertion of a negative dispersion component.

Many are the solution that allows to compress the pulses, such as chirped mirror, pair of gratings, pair of prisms or pulse shapers. The simpler one that can work in the NIR spectral region is the *prisms compressor*. This setup works as it can be seen in Fig. 4.9. There are two identical isosceles prisms of fused silica (SiO_2) with angles of 60° that are crossed by the pulse twice. First prism divides all the spectral component giving to each a different deviation angle. Due to the Sellmeier equation of the fused silica, the low frequencies arrive before the high ones, and thus it introduces a positive chirp. The red is less deflected respect to the blues and thus while entering in the second prism it passes through less amount of glass. After the second prism there is a reflecting mirror that folds the beam backward so that out of the fist prism the pulse has all the spectral component overlapped again.

This prism compressor introduces an overall negative dispersion due to the geometry and thus it slows the lower frequencies respect to the higher ones. The

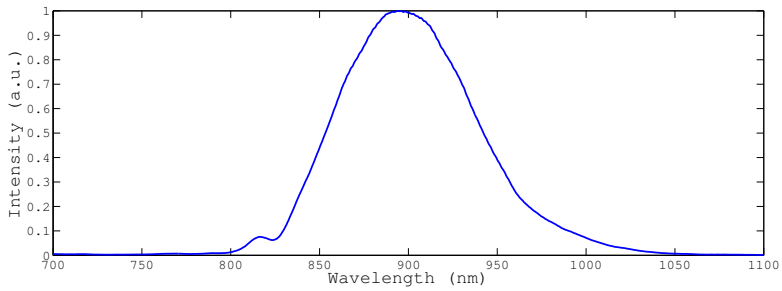

Figure 4.10: NIR non-collinear optical parametric amplifier spectrum tuned ad 900 nm.

same is true for the third order dispersion, thus it can be written

$$\begin{aligned} D_2 &= D_{2,compressor} + D_{2,glass} \\ D_3 &= D_{3,compressor} + D_{3,glass} \end{aligned} \tag{4.8}$$

where $D_{2,compressor}$ and $D_{3,compressor}$ are negative and bigger than $D_{2,glass}$ and $D_{3,glass}$ that are positive and all are proportional to the distance L between the prisms.

In order to reduce the reflection losses on the surface on the prisms, they are positioned at Brewster angle respect the beam that must be p-polarized. In this way these losses are avoided. Moreover prisms are put at the *minimum insertion*, meaning that the overall amount of glass is minimized.

In order to compress the NIR pulse the degree of freedom on which it is possible to play is the distance between the prisms edge L. By measuring the duration of the NIR pulse after compression it has been found that the optimum distance L is around 16.3 cm.

4.2.3 Pulse characterization

The NIR-OPA has been characterized by measuring the pulse duration and pulse spectrum. The NOPA is pumped with 400 mW, the 390 nm pump has a power of 40 mW and the white light is generated with 2 mW. The outer NIR pulse has a maximum power of 2 mW ca. The optimized spectrum associated is centered at 900 nm and is reported in Fig. 4.10. The $\Delta\lambda$ is in the order of magnitude of 100 nm, thus the NIR pulse has a band of 40 THz ca.

The temporal duration of the pulse is investigated by a nonlinear technique, i.e. the second harmonic FROG (SH-FROG). The measured auto-correlation function is analyzed with a quite complex algorithm that allows to retrieve information about spectral phase and spectral intensity of an unknown pulse. In Fig. 4.11 is reported a FROG trace showing that the pulse duration is less

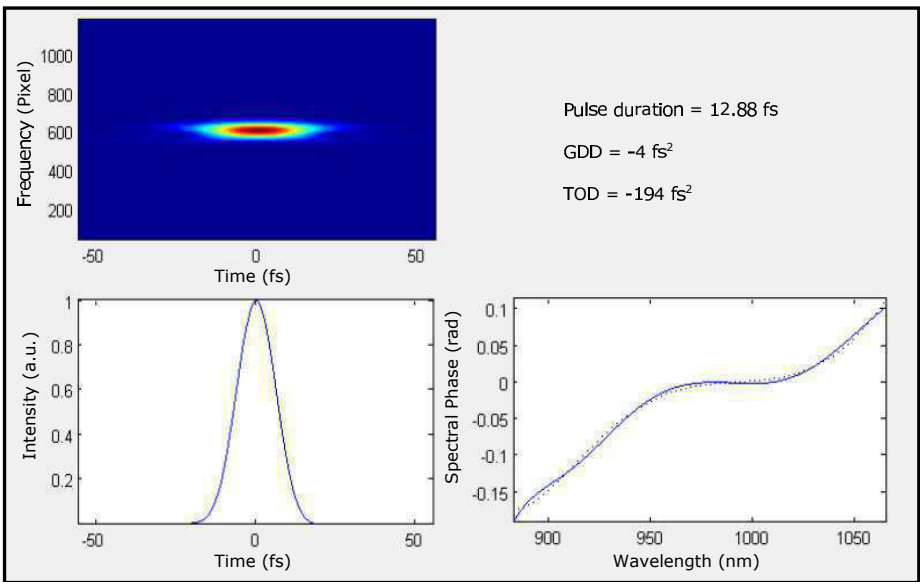

Figure 4.11: FROG trace of the NIR pulse and spectral phase and pulse duration retrieved from the map.

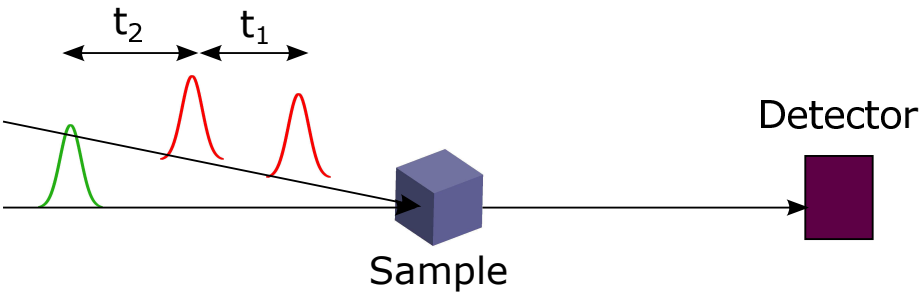

Figure 4.12: Pump probe geometry for 2DES.

than 15 fs, near the transform limited value.

4.3 2D setup

The bidimensional electronic spectroscopy set-up is schematized in Fig. 4.12.It can be easily implemented since it is based on a simple auto-correlator. In one arm the free propagating probe passes through an optical delay line so that it can be delayed respect the pump pulses.

In the other arm of the auto-correlator the two pump pulses are generated by the TWINS setup. Due to the dispersion introduced by the wedges the two pump pulses must be compressed. This can be done thanks to some particular chirped mirror that work in the NIR region [20] [21].

Chirped mirror are dielectric multilayer mirrors that are able to give a certain negative dispersion. Dielectric mirror made by multiple thin layers of dielectric material grown on a substrate. The choice of the material and the thickness of the layers allow to generate high reflective mirror for certain spectral regions. The succession of low and high refractive index layers is the responsible of the final behavior of the mirror. Indicating with d_H the thickness of the high refractive index layer and by d_L the one of the other layers, it is possible to represent the dielectric mirror as in Fig. 4.13.a). Defining n_H and n_L the high and low refractive index respectively the reflectivity of the mirror results:

$$R = \left[\frac{(\frac{n_0}{n_s})(\frac{n_L}{n_H})^{2n} - 1}{(\frac{n_0}{n_s})(\frac{n_L}{n_H})^{2n} + 1} \right]^2 \tag{4.9}$$

where n is the number of couple of layers. To be able to reflect a certain wavelength λ, there must be positive interference from all the reflections. This fix the thicknesses of the layers at certain values:

$$d_H = \frac{\lambda}{2n_H} \qquad\qquad d_L = \frac{\lambda}{4n_L}. \tag{4.10}$$

Chirped mirror are based on these kind of mirrors but are used in optics as media able to give a negative dispersion able to compensate the positive dispersion of the many optical material. Positive chirp given for example from the air to a pulse act on it by slowing the bluer component respect to the redder. Chirped mirror must do the reverse, i.e. they must be able to make propagate more the redder spectral components. This is done by varying the thickness of the layers gradually in order to be able to reflect in the former layers the blue light, while the red is reflected in the latters. In Fig. 4.13.b) is shown the behavior of the dielectric chirped mirror when hit by a broadband pulse. This result is quite difficult to be obtained since the control on the thickness of the layers must be very accurate.

Chirped mirror are often used in pairs, because the control of the group delay dispersion is rarely as good as it is needed. It is often an oscillating function and thus by combining the effect of one double chirped mirror (DCM) with another it become at least linear. The drawback of chirped mirror is that they introduce a certain dispersion for each reflection. By changing the number of bounces between the chirped mirror, different dispersion are given to the pulse. The more the bounces are, the more the introduced negative dispersion is. To be able to finely control the dispersion of a pulse, chirped mirror should be used together with come other continuum dispersive media like is represented in Fig. 4.14.

The chirped mirror used in the 2D setup are actually designed to be used

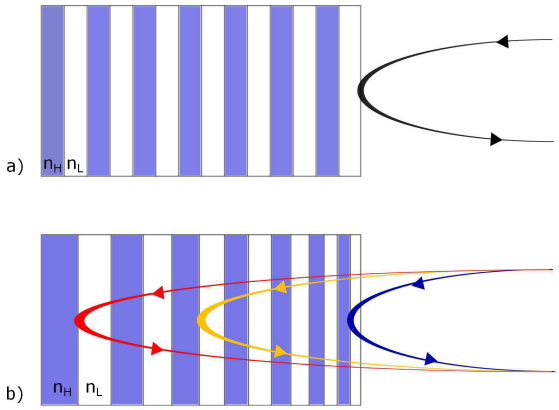

Figure 4.13: a) Dielectric multilayer mirror scheme. Low refractive index layers interchange with high refractive index layers always with the same thicknesses. b) Chirped mirror scheme. The thickness of the layers is changing inside the mirror in order to reflect different wavelength at different depths.

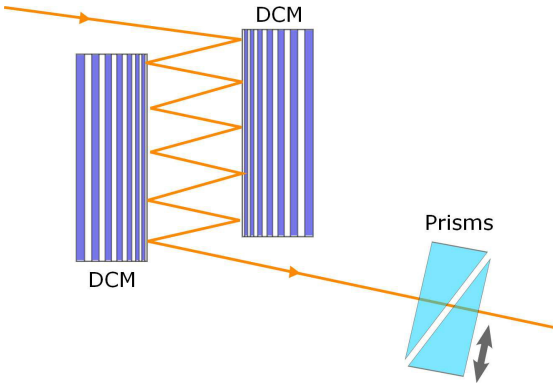

Figure 4.14: Fine compressor. Dispersion introduced by a discrete number of bounces on the double chirped mirror (DCM) is finely controlled by pair of prisms.

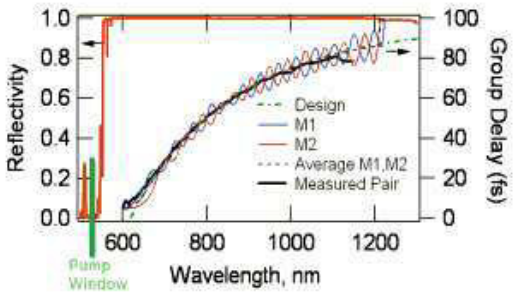

Figure 4.15: Double chirped mirror reflectivity and group delay dispersion.

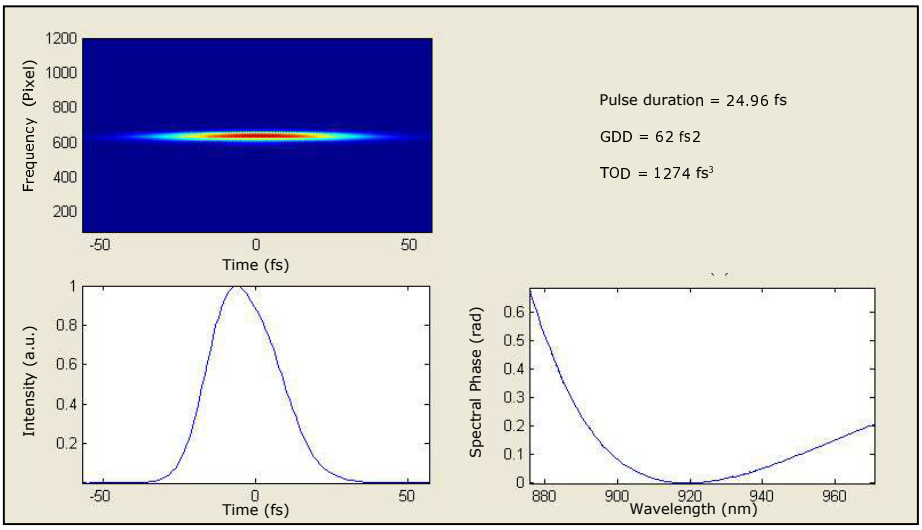

Figure 4.16: FROG trace of the NIR pulse after the TWINS setup and spectral phase and pulse duration retrieved from the map.

in the *fs* Ti:sapph lasers after the regenerative stage. In Fig. 4.15 are reported the reflectivity and the group delay introduced: one can see that they work in a very broadband spectral region from 600 nm to 1200 nm. Moreover the DCMs were designed with an analytical method for computing dispersion of multilayer coatings and generate the exact negative dispersion to compensate the path and the optics into laser cavity. [21, 20]

By using these mirror to compress the pump pulses it has been found that after three bounces per mirror the compression is not the best. The FROG trace of the pump pulse is reported in Fig. 4.16. It is possible to see that the pulse is not compressed completely and this is due to the discrete contributions of the DCM used. Thus pump pulses have nearly 30 fs of temporal duration.

On the pump arm there are the TWINS setup and these chirped mirror. The

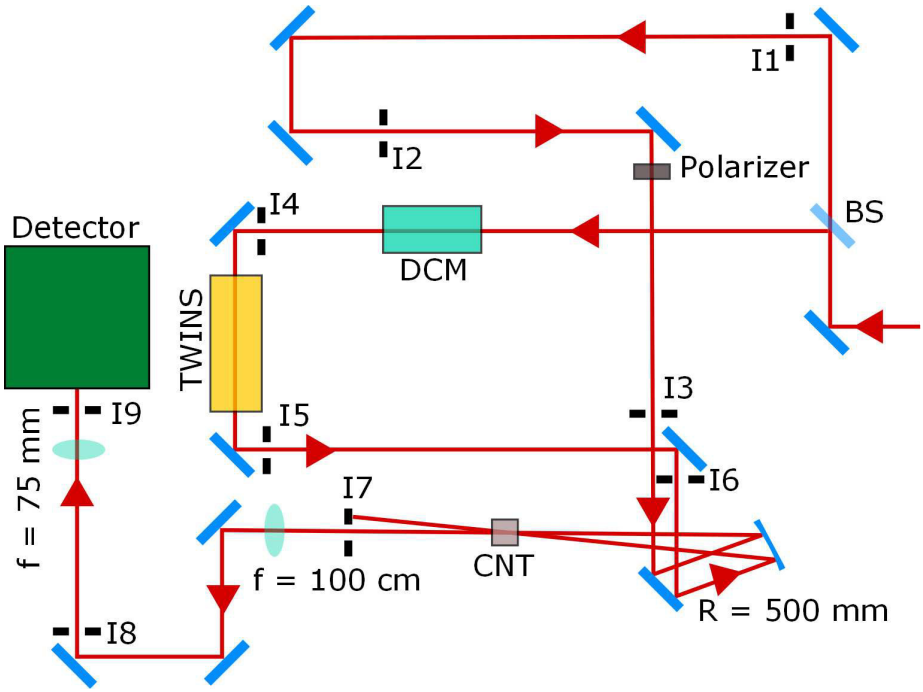

Figure 4.17: 2DES setup.

TWINS setup is composed by one half-wave plate that turn the polarization of the NIR-NOPA by 45°, two pair of wedges orthogonally cut, one α-BBO plate 1.6 mm thick and one polarizer aimed at turning the two polarized pumps again at 45°. All these optical component introduce a positive dispersion that can be compressed by the chirped mirrors since these elements introduce a negative dispersion. The only limit of the DCMs is that they work with discrete steps, i.e. with discrete number of bounces. By measuring the pump pulse duration for the fixed replica that sees always the ordinary refractive index, it is has been found that the optimum corresponds to three bounces on each mirror giving as a result less than 28 fs. The compensation of the chirped mirror thus is not optimal and should be finely adjusted in some other way.

The final setup is shown in Fig. 4.17. The probing area where the electromagnetic radiation interacts with the sample is made with concave mirror with radius of 500 mm and hence with a focal length of 250 mm. The pump pulse is spatially blocked by an iris while the probe with the target beam propagate together. They are finally focused on a the revelation camera.

In order to perform the measurement on the electronic transitions on a sample of Carbon Nanotube (CNT), that will be described in the next chapter, both the pump pulses and the probe were coming from the same NIR-NOPA. Thus experiment is a *degenerate* bidimensional spectroscopy measurement in

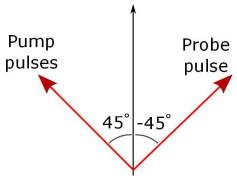

Figure 4.18: Pump and probe are orthogonally polarized during the measurement.

the pump probe geometry. Due to this choice of pump and probe wavelength, the signal is affect to scattering from the pump that interferes with the probe pulse. The solution adopted is to set an angle between the pump and the probe polarizations [22]: while the pump pulses from the wedges are polarized at 45°, the probe pulse's polarization is turned at -45° respect the vertical axis. In this way the two orthogonally polarized pulses should not see one the other. Due to the sample nature it is possible to detect some signal even if it is pumped at a crossed polarization. In the setup hence a polarizer is introduced also in the pathway of the probe pulse. Pump and probe polarization is sketched in Fig. 4.18.

Chapter 5

Experimental Results

In this chapter is presented a measurement of bidimensional electronic spectroscopy (2DES) on a single wall carbon nanotubes (SWNTs). This experiment is performed with the setup described earlier with the NIR pulse generated from the noncollinear optical parametric amplifier. In the first section is briefly presented the sample. The aim of the experiment is to look at the inhomogeneous broadening in such a system (see Appendix ??). Several 2D maps has been recorded at different T time in order to follow the photoexcited dynamics of the SWNTs.

5.1 Carbon nanotube

Carbon nanotube (CNT) are allotropes of Carbon (C) that due to its valence can grows in different forms. Diamonds, graphite, graphene and fullerenes are different kind of allotropes that can be found. Carbon nanotubes belong to the last group together with some spherical and ellipsoidal formation.

Carbon nanotubes are at least what can be considered a one-dimensional (1D) system: it has one atom in thickness, few tens of atoms in circumference and many microns in length [4]. CNT are formed from a rolled one-atom thick carbon layer, that is the graphene.

The structure and the physical properties of this sample are strictly connected to its chiral vector $\vec{C_h}$. In order to understand how this vector is, let's consider the hexagonal honeycomb lattice in the real space of the graphite drawn in Fig. 5.1. Being $\vec{a}_1$ and $\vec{a}_2$ the real space basis vector, the chiral vector $\vec{C_h}$ is defined as

$$\vec{C_h} = n\vec{a_1} + m\vec{a_2} \equiv (n, m) \tag{5.1}$$

where n and m indicate the number of bases vector $\vec{a}_1$ and $\vec{a}_2$ contained in the

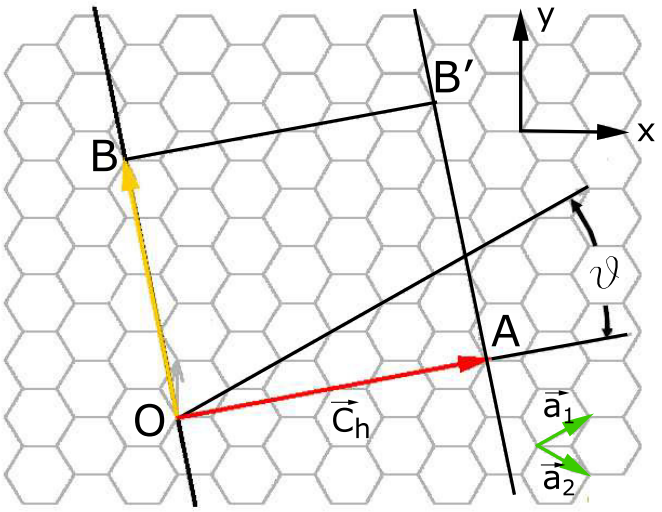

Figure 5.1: Graphite sheet structure. Chiral vector connects two identical point in the real space of the material [4].

chiral one. This vector is crossed with the $\vec{a}_1$ direction at an angle θ that is defined *chiral angle*.

The chiral vector connects two crystallographically equivalent sites O and A on a two-dimensional (2D) graphene sheet where a carbon atom is located at each vertex of the honeycomb structure. The graphite plane is thus rolled and the junction is along the two parallel direction OB and AB'.

The diameter d_{CNT} of the resulting nanotube is hence connected to the chirality i.e. to (n, m) as follows

$$d_{CNT} = \frac{C_h}{\pi} = \frac{3^{\frac{1}{2}} a_{C-C} \left(m^2 + mn + n^2\right)}{\pi} \tag{5.2}$$

where C_h is the amplitude of the chiral vector and a_{C-C} is the nearest-neighbor C-C distance. The chiral angle θ is define as

$$\theta = tan^{-1} \left[3^{\frac{1}{2}} \frac{m}{(m + 2n)} \right]. \tag{5.3}$$

A CNT can be thus identified from the chiral vector $\vec{C}_h$ or also from ts diameter d_{CNT} and chiral angle θ. From these parameter it is possible to retrieve several information also about the physics of the sample. It must be considered that carbon nanotube can be either metallic or semiconductor. From literature it is possible to establish one rule that allows to distinguish the one from the

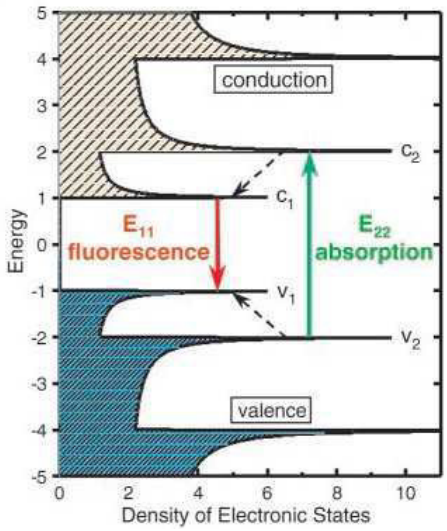

Figure 5.2: Density of state (DOS) of 1-D semiconducting carbon nanotube. Discontinuous spikes are the Van Hove singularities. [5]

other. If n and m indices satisfy the following equation

$$2n + m = integer \tag{5.4}$$

CNT behaves as a metal.

Since CNT are a model of 1-D system it density of state (DOS) is not continuum but it is discrete with discontinuous spikes called Van Hove singularities. By looking at the transitions in Fig. 5.2 the only allowed are between $v_1 \rightarrow c_1$ or $v_2 \rightarrow c_2$, etc. labeled as E_{11} and E_{22}, etc. The energy of the Van Hove singularities depend on the type of nanotube and hence from the chirality.

The optical transitions E_{ii} thus are intrinsically defined from the type of CNT considered. Since the transition is quite sharp, the optical signal allows to detect without ambiguity the nanotube under test [5].

One topic of big interest is the study of the dynamics of the CNT in order to analyze the photoexcitational transfer along the tube. Moreover it is very interesting the study of energy transfer between two different nanotube coupled in a system [23] [24] [25] [26].

Carbon nanotube are nowadays a hot topic since they have interesting electric, thermal and mechanical properties that make them promising for many application from optoelectronic to photovoltaic.

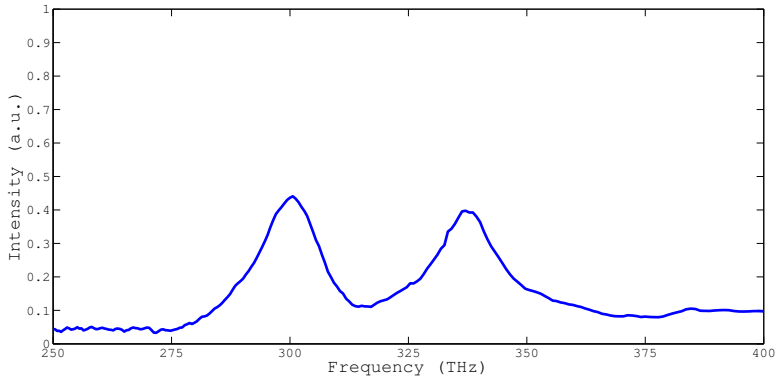

Figure 5.3: Absorbance of the carbon nanotube prepared at the University of Würzburg.

5.1.1 CNT (6,4) and (7,5)

The carbon nanotube analyzed in our laboratory is a coupled system in which the predominant chiralities are (6,4) and (7,5). It has been studied the first excitonic transition of the system whose absorption spectrum is represented in Fig. 5.3. The sample shows two peaks at 900 nm and 1000 nm (335 THz and 300 THz respectively). From literature it is possible to relate these absorption frequency to the two cited nanotubes [5]. From the spectrum it can be seen that there is a shoulder around 320 THz maybe due to the presence of the (6,5) carbon nanotube.

In the bidimensional spectroscopy experiment it has been used the NIR characterized pulse from the NOPA that allows to excite both the two nanotubes together. The aim of the experiment is twofold: first of all to look at the inhomogeneous lineshape of the nanotube, and in second instance to check if some energy transfer take place between the two CNTs.

5.2 2D maps

The very first results recorded in the 2DES experiments are represented in this paragraph. The temporal trace at different delays between the pump pulses is represented in Fig. 5.4. By Fourier transforming this map respect to the horizontal axis and considering the calibration obtained from the wedges it is obtained the bidimensional map as a function of two frequency axis, the pump and the probe frequency (Fig. 5.5). The resolution along the pump spectral components is the additional information given by 2DES. The 2D maps have been recorded at 50 fs, 100 fs, 200 fs, 500 fs and 1 ps of T delay.

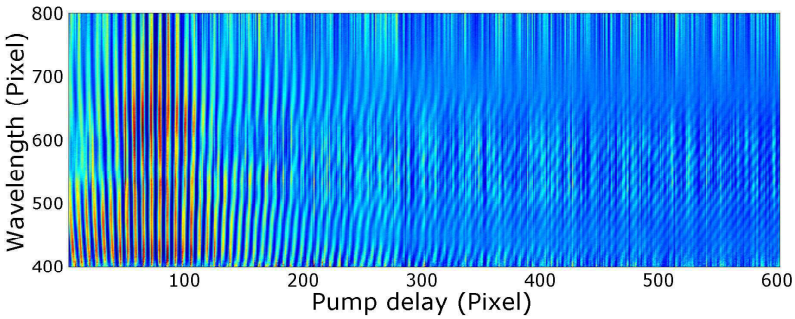

Figure 5.4: Temporal trace recorded in the 2DES experiment.

In the maps the positive signal represent a strong transient bleaching signal assigned to population on the first excitonic state E_{11}. Fig. 5.5.A) is the map at 50 fs of delay. It is possible to see both the excitations of the (6,4) and (7,5) nanotubes. Fig. 5.5.B), C), D) and E) report the situation at 100 fs, 200 fs 500 fs and 1 ps T delays. It is observed an elongated peak at 900 nm (335 THz) that changes in shape at later delays, reflecting the inhomogeneity of the system. From these maps is represented also the dynamic of the first excited state that is slowing relaxating.

In the very first time the CNT is excited and probed at the same frequencies (signal on the diagonal). That means that the CNT excited at a certain pump frequency remembers this pump energy and is probed at the same one. After some time CNT looses the memory of the pump and thus the spot become less defined and more spread in frequency. This can be explained by a zoom of the most intense peak in Fig. 5.5. In Fig. 5.7.A), B) and C) are thus displayed a zoom on the (6,4) CNTs signal at 50 fs, 200 fs and 1 ps of T delay. It is possible to see that the spot is not perfectly circular due to the inhomogeneous broadening of the sample. It is easily detected in 2D maps by a direct comparison with the homogeneous broadening that is the width of the spot in the anti-diagonal direction (white arrows in figure). At bigger T the system looses memory of the excitation (*dephasing*) and the spot increases in size and is more blurred. This change in shape can be interpreted as a spectral diffusion of the system. Kowing the homogeneous broadening is very important because from its evolution, it is possible to evaluate the dephasing time of the system. From Fig. 5.7 the homogeneous broadening at 50 fs, 200 fs and 1 ps respectively, has a linewidth of 5.94 THz, 6.26 THz and 8.658 THz. As expected this value is increasing in time.

The homogeneous absorption spectra as retrieved in Eq. 2.18 is a Lorentzian

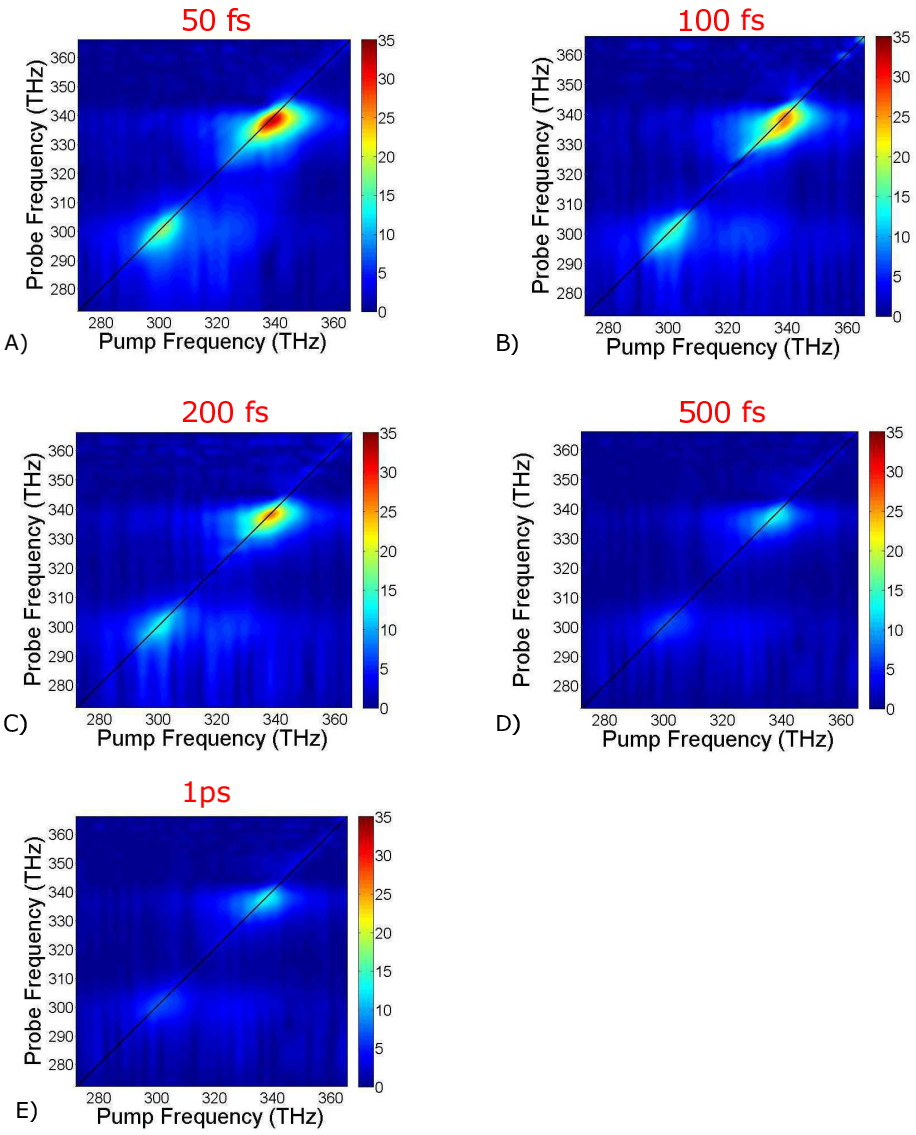

Figure 5.5: 2DES maps at different delays between the second pump pulse and probe.

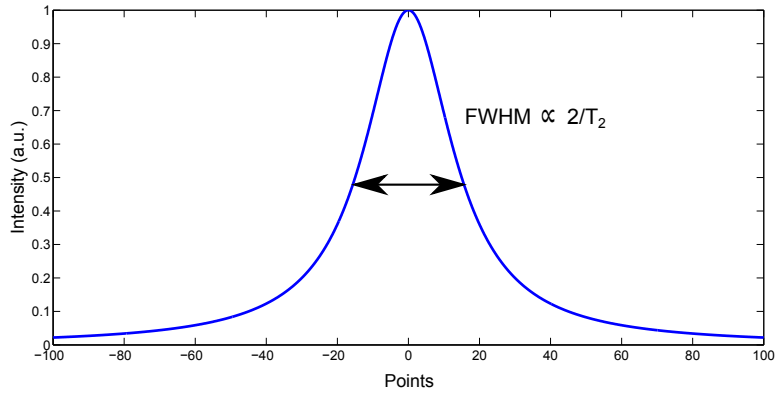

Figure 5.6: Lorentzian lineshape. The FWHM is related to the *dephasing* time.

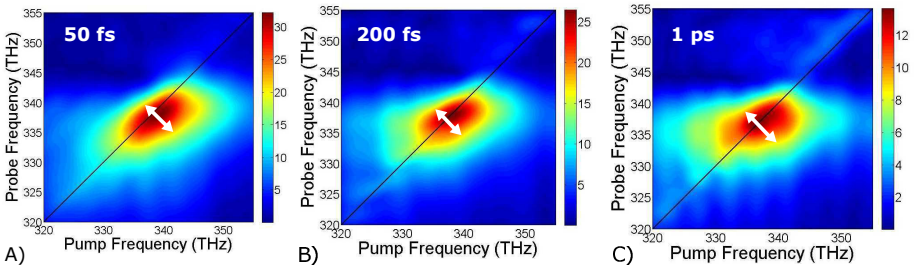

Figure 5.7: Zoom on the (6,5) CNT 2D map at different T delays. The white arrows indicate the homogeneous broadening. It is possible to see that the spot is even more blurred as the delay T increases.

function that is directly related to the *dephasing* time:

$$A(\omega) \propto \frac{\Gamma}{(\omega - \omega_0)^2 + \Gamma^2} \tag{5.5}$$

where Γ is

$$\Gamma \propto \frac{1}{T_2} \tag{5.6}$$

and T_2 is the *dephasing* time of the system. The maximum value of this lineshape is when $\omega = \omega_0$ and thus it is proportional to $\frac{1}{\Gamma}$. Thus the FWHM of the Lorentzian displayed in Fig. 5.6 is

$$FWHM = 2\Gamma \propto \frac{2}{T_2}. \tag{5.7}$$

From the complete maps in Fig. 5.5 it seems that there is no relevant energy exchange between the two nanotubes. More measurement can help to understand if the absence of the cross peaks is due to the sample itself. Since

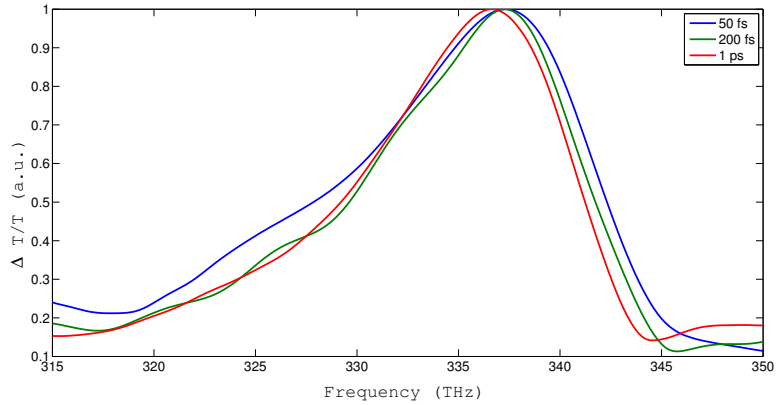

Figure 5.8: Marginals of the 2D maps at 50 fs, 200 fs and 1 ps of T delay.

in literature ([23]) it seems that an energy transfer should relate two coupled nanotube, the possible reason of the absence of the formation of cross peaks in the maps in Fig. 5.5 can be due to the fact that the carbon nanotube are quite far and thus don't interact each other.

In order to prove the importance of bidimensional spectroscopy these results are compared to those obtained from a simple pump probe experiment. 2DES bases its great potential to the spectral resolution along the pump axis and on the possibility to read all the information available with other nonlinear spectroscopy techniques. Thus if the integral over the pump axis is performed the resulting data are equivalent to those retrieved from a pump-probe experiment. This marginals evaluated from the 2D maps are shown in Fig. 5.9 at all the different population delays T. From this data it is possible to measure the decay of the excitation of the first excited state. It seems that both the peaks decay in time with almost the same temporal constant. This validate the hypothesis of non-coupled carbon nanotubes in the sample.

From pump-probe experiment any information about the inhomogeneity of the sample can be retrieved. By plotting the singularity normalized spectra at different T, the only difference that can be seen in the central frequency of the peak. In Fig. 5.8 are plotted the temporal spectra of the most intense peak of the (6,4) CNT. It is visible a very small red shift of the peak, while the shape is almost the same. Anything can be said about the composition of the sample. By looking at the same delays displayed in Fig. 5.7 it is evident the great potential of the bidimensional spectroscopy since it says something about the lineshape of the CNT.

To understand if the absence of energy transfer between the CNTs is an issue of the sample, a complementary fluorescence experiment could be performed.

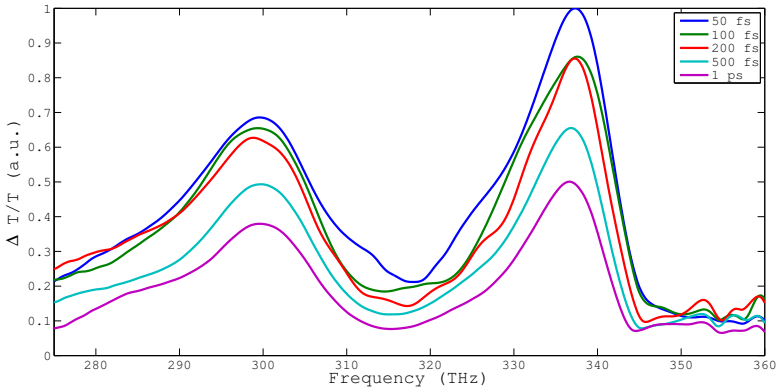

Figure 5.9: Marginal of the 2D map. This data correspond to those obtained from a pump probe experiment. The spectral resolution along the pump axis is lost.

Fluorescence measurements loose the temporal resolution of the dynamics address the question of a possible energy transfer in this system.

It should be said that many can be the reasons why this couplings are not displayed. The fact the pump pulses and the probe one have crossed polarization can be one, but also the analysis performed with broadband pulses that excite both the CNTs can give wrong results.

Many are the improvements that can be done on the setup. First of all the the pulses involved must be optimized since the one used in these experiments were still not the optimal. The compression of the wedges must be finely controlled and for example, using the NIR pulses, this could be easily done by moving the prisms of the compression stage. In this way, since the measurement is an auto-correlator experiment, the probe pulse will be chirped, but the temporal resolution of the experiment would be better respect the opposite case of chirped pump.

From the maps it is possible to see that the signal retrieved is quite noisy and this is due to some scattering between the two pumps in the sample. By playing with their polarization these problem can be avoided but this solution will limit the number of samples that can be measured.

Another test that can be done is to focus on the sample with a shorter focal length. In this way pump and probe will be crossed at a bigger angle and thus scattering from the pump can also be spatially filtered.

In light of all it has been said many other measurement can be performed but it is evident that bidimensional spectroscopy has a very important role in the analysis of systems.

5.3 Conclusion

In this thesis I focused my attention on the development of a new nonlinear spectroscopy system, the 2DES. In order to be able to realize a bidimensional spectroscopy setup in our laboratory, we started from the realization of a near infrared non collinear optical parametric amplifier (NIR-NOPA). The NIR pulse has been compressed by a prisms compressor and then characterized with a FROG technique from which we extracted a pulse duration near to the transform limit value: 13 fs.

In order to develop a bidimensional spectroscopy setup in the pump-probe configuration an auto-correlator has bean realized. On one arm a translation stage allows the control of the population delay T (waiting time) while in the other the TWINS device leads to the generation of a phased-locked delayed pump pulses. TWINS is a system based on birefringence phenomena that generates two replicas locked in phase starting from a single incoming pulse. Thanks to the possibility to finely control the temporal delay τ it is possible to obtain a 2D map characterized by the spectral resolution on the pump axis.

We then recorder preliminary results obtained on a single walled carbon nanotubes (SWNTs) sample. It is evident the great potential of this technique: thanks to pump frequency resolved axis many features of samples can be detected, like the inhomogeneous broadening. Carbon nanotubes absorb in the NIR spectral range and thus in the recorded maps the bleaching signal of the first excited state can be seen. We observed the inhomogeneous broadening by looking at the shape of the spot of the signal. By measuring different maps in function of T it can be also studied the evolution of the sample. In the case under analysis we showed how the spot changes in shape proposing as a tentative explanation a possible spectral diffusion in the nanotubes.

To conclude we showed how bidimensional spectroscopy can be more complete respect to other nonlinear spectroscopy technique (as the pump-probe) leading to a deeper analysis of matter.

Appendix A

Homogeneous and Inhomogeneous broadening

Homogeneoug and Inhomogeneous broadening of a sample are phenomena that affect the spectrum of any material. This is due to all the interaction of the system with all that is around. As a result of the broadening the linsehape of the system is changing.

Let's consider an atom. It has only one resonance frequency ω_0 and thus its absorption spectrum should be only a δ-function. But this is not true since many factors make the lineshape wider. It is possible to distinguish between causes of homogeneous and inhomogeneous broadening.

Homogeneous broadening happens when the lineshape is changing in the same way and in any direction of the spectrum, non-depending on the resonant frequency. This mechanism actually broadens the lineshape in the same way for each atom. This make the δ-function a Lorentzian function. For example this results when a system collides elastically with gases or when spontaneous emission occurs (natural broadening). In Fig. A.1 is represented an example of homogeneous lineshape: a Lorentzian.

When the broadening is not the same for every frequency, but is is different it is the case of *inhomogeneous broadening*. It happens that the resonance frequencies ω_R of an atoms are distributed around some central frequency ω_0 with a certain distribution function. The mechanism thus distributes the resonance frequencies over a spectral range. Many are the cause of this kind of broadening. For example in a solid local electric and magnetic field (Stark effect) generate a discontinuity in the lattice that is the responsible of this resonant frequency distribution. Another possible reason is connected to phonons in a material that modify the local potential of a sample. The resulting lineshape

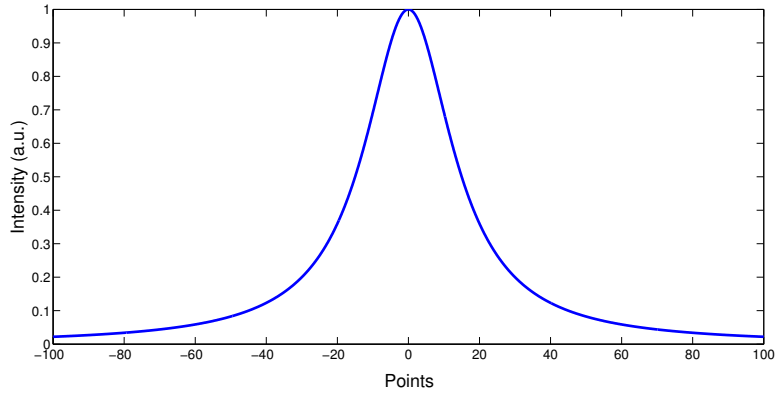

Figure A.1: Homogeneous broadening. Lorentzian lineshape.

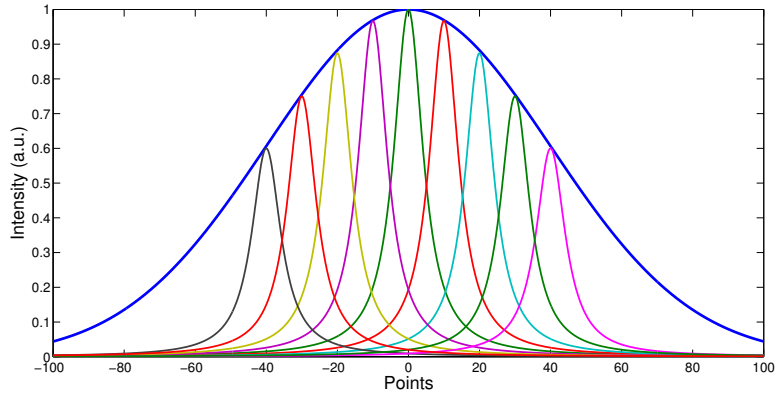

Figure A.2: Inhomogeneous broadening. Gaussian lineshape as a conribution of many Lorentzian ones.

can be seen as many homogenous line composed toghether and resulting in a Gaussian lineshape. In Fig. A.2 is displayed this concept.

Considering one single atom if different broadening mechanisms occur the resulting lineshape is the convolution of the lineshape broadening contributes. That mean that if only Lorentzian broadening take place, the final lineshape is a Lorenztian. The same is true when only inhomogeneous Gaussian broadening occurs, giving a final Gaussian lineshape. When both homogeneous and inhomogeneous broadenings affect the spectrum of an atom, the final lineshape is the integral of the two curves, Lorentzian and Gaussian. This curve is defined as Voigt profile [27].

In spectroscopy the analysis is performed on a ensable of atoms and molecules, and thus revealing of homogeneous broadening is a quite hard purpose. The principal contribute of the lineshape therefore is strictly connected to the in-

homogeneous broadening that is responbile of the lineshape of the absorption and emission spectrum of a sample, that hence will have a dominant Gaussian lineshape.

In spectroscopy knowing the lineshape of a sample is very important since from it it could be retrieved the *dephasing* time of the excited coherences.

Bibliography

[1] P. Hamm and M. Zanni, *Concepts and Methods of 2D Infrared Spectroscopy*, Cambridge University Press, 2011.

[2] J. Helbing and P. Hamm, *Journal of the Optical Society of America B* **28**, 171 (2010).

[3] G. Cerullo, C. Manzoni, L. Lüer, and D. Polli, *Photochemical & photobiological sciences : Official journal of the European Photochemistry Association and the European Society for Photobiology* **6**, 135 (2007).

[4] M. S. Dresselhaus and P. C. Eklund, *Advances in Physics* **49**, 705 (2000).

[5] S. M. Bachilo, M. S. Strano, C. Kittrell, R. H. Hauge, R. E. Smalley, and R. B. Weisman, *Science (New York, N.Y.)* **298**, 2361 (2002).

[6] S. Mukamel, *Principles of Nonlinear Optical Spectroscopy*, Oxford Series in Optical and Imaging Sciences, Oxford University Press on Demand, 1999.

[7] P. Hamm, *Principles of Nonlinear Optical Spectroscopy : A Practical Approach or : Mukamel for Dummies*, 2005.

[8] X.-T. Liang, *Chinese Physics Letters* **29**, 084211 (2012).

[9] N. S. Ginsberg, Y.-C. Cheng, and G. R. Fleming, *Accounts of chemical research* **42**, 1352 (2009).

[10] M. Cho, T. Brixner, and I. Stiopkin, *JOURNAL-CHINESE ...* **53**, 15 (2006).

[11] R. M. Hochstrasser, *PNAS* **104**, 14190 (2007).

[12] S. Bonora, D. Brida, P. Villoresi, and G. Cerullo, *Optics express* **18**, 23147 (2010).

[13] S. Bonora, *Optics Communications* **284**, 3467 (2011).

[14] G. Chériaux, O. Albert, V. Wänman, J. P. Chambaret, C. Félix, and G. Mourou, *Optics letters* **26**, 169 (2001).

[15] S.-H. Shim and M. T. Zanni, *Physical chemistry chemical physics : PCCP* **11**, 748 (2009).

[16] D. Brida, C. Manzoni, and G. Cerullo, *Optics letters* **37**, 3027 (2012).

[17] D. E. Zelmon, D. L. Small, and D. Jundt, *Journal of the Optical Society of America B* **14**, 3319 (1997).

[18] D. B. Turner, K. E. Wilk, P. M. G. Curmi, and G. D. Scholes, *The Journal of Physical Chemistry Letters* **2**, 1904 (2011).

[19] G. Lanzani, G. Cerullo, and S. De Silvestri, *Coherent Vibrational Dynamics*, Practical Spectroscopy, Taylor & Francis, 2007.

[20] J. R. Birge, H. M. Crespo, M. Sander, and F. X. Kärtner, Non-Intrusive Sub-Two-Cycle Carrier-Envelope Stabilized Pulses Using Engineered Chirped Mirrors, in *Conference on Lasers and Electro-Optics/Quantum Electronics and Laser Science Conference and Photonic Applications Systems Technologies*, p. CTuC3, Optical Society of America, 2008.

[21] H. M. Crespo, J. R. Birge, E. L. Falcão Filho, M. Y. Sander, a. Benedick, and F. X. Kärtner, *Optics letters* **33**, 833 (2008).

[22] W. Xiong and M. T. Zanni, *Optics letters* **33**, 1371 (2008).

[23] R. D. Mehlenbacher, M.-Y. Wu, M. Grechko, J. E. Laaser, M. S. Arnold, and M. T. Zanni, *Nano letters* **13**, 1495 (2013).

[24] J. J. Crochet, S. Hoseinkhani, L. Lüer, T. Hertel, S. K. Doorn, and G. Lanzani, *Physical Review Letters* **107**, 257402 (2011).

[25] C. Manzoni, a. Gambetta, E. Menna, M. Meneghetti, G. Lanzani, and G. Cerullo, *Physical Review Letters* **94**, 207401 (2005).

[26] M. W. Graham, T. R. Calhoun, A. a. Green, M. C. Hersam, and G. R. Fleming, *Nano letters* **12**, 813 (2012).

[27] O. Svelto and D. Hanna, *Principles of Lasers*, Springer, 1998.